# Photonics and Transport in Bulk Heterojunction Organic Solar Cells

by
John R. Tumbleston

A dissertation submitted to the faculty of the University of North Carolina at Chapel Hill in partial fulfillment of the requirements for the degree of Doctor of Philosophy in the Department of Physics and Astronomy.

Chapel Hill
2011

Approved by:

Rene Lopez, Advisor

Edward Samulski, Reader

Sorin Mitran, Reader

Yue Wu, Reader

Charles Evans, Reader

**ABSTRACT**

**JOHN R. TUMBLESTON: Photonics and Transport in Bulk Heterojunction Organic Solar Cells. (Under the direction of Rene Lopez.)**

In this thesis, the groundwork is established for a new type of bulk heterojunction (BHJ) organic solar cell geometry that has photonic crystal (PC) photoactive layers. This design is motivated by the need to improve light absorption without increasing active layer thickness, which for many BHJ systems, degrades electrical performance. It is demonstrated that with the right choice of materials and cell dimensions, quasiguided or resonant modes are excited near the band edge of a variety of BHJ blends to enhance absorption. Resonant modes are predicted by first developing a scattering matrix optical model and then observed in wavelength-, polarization-, and angular-dependent reflection and photocurrent measurements. PC cells are fabricated using a facile nanopatterning technique, where highly ordered arrays of submicron features are constructed over large areas in a single step. Optical and electrical function of this new cell architecture is fully explored in this thesis.

Through optical measurements and modeling, PC devices show clear enhancements in light absorption. On the other hand, the impact of the nonplanar geometry on electrical performance is not as easily deduced due to the multitude of electrical processes that lead to photocurrent generation. First, the electrical properties of the electron transporting layer that interfaces with the BHJ nanopattern and provides optical contrast in the PC greatly affect parasitic resistances in the solar cell. By including resistance losses in a drift/diffusion numerical model that describes electrical performance, it is shown that these losses greatly influence fundamental steps leading to photocurrent generation. This is confirmed with experiment by comparing two BHJ material systems that have different affinities for exciton separation. Second, significant levels of free carrier recombination are predicted by the electro-optical model due to the relatively long transport paths in the nanopattern features. To test this prediction, an experimental technique is developed to measure the transport lengths of photogenerated electrons and holes in BHJ solar cells. It is found that transport lengths of positive and negative carriers are mismatched and helps explain both PC electrical performance and recent conflicting results of planar BHJ solar cells in the literature.

# Acknowledgments

First and foremost, I would like to thank Profs. Rene Lopez and Edward Samulski for their guidance during my time as a graduate student. They have offered countless suggestions and comments regarding my experiments, presentations, and manuscripts since I began research on organic solar cells in the summer of 2007. I also thank Profs. Sorin Mitran, Yue Wu, Gerald Cecil, and Charles Evans for being on my thesis committee.

Second, I am grateful to have worked alongside Doo-Hyun Ko, a former chemistry graduate student. All work of this thesis has been published as a joint effort between us. I learned many things from him during our work together and am indebted for the time and effort he spent to conduct our research.

Finally, I would like to thank the many people who offered contributions, help, or suggestions regarding this work. I thank Neal Johnson, Philip Thompson, Cliff Tysor, and Steve Medlin for their expertise in the machine shop, Christoph Kirsch for conversations regarding numerical calculations, Abay Gadisa for his careful readings of my manuscripts and our many discussions, Mukti Aryal for our fruitful conversations, Brittany McPherson for her assistance with purchasing, Christina Redmon and Duane Deardorff for their help with instrumentation, Carrie Donley, Bob Geil, and Amar Kumbhar for their assistance with and upkeep of CHANL equipment, Doug Mar, Mike Houchins, Stuart Williams, Meredith Hampton, and Kai Chen for their assistance with P.R.I.N.T., Walter Schenck for supplying polymer films, Kristen Alexander, Yingchi Liu, Rudresh Ghosh, and Emily Ray for all their help in the lab, Ethan Klem, Will Rice, and Prof. Frank Tsui for suggestions regarding conductivity measurements, Prof. Wei You and his group for sharing their glovebox system, Brad Barlow and Emily Morgan for their extensive help with LabView programming, and Adam Shields for use of his wonderful LaTeXthesis template.

Personally, I am grateful to mom and dad, Katherine and Jake, Alison, Brad, and Doo-Hyun for their unwavering support and encouragement.

# Contents

# List of Tables

# List of Figures

# List of Symbols and Abbreviations

| | |
|---|---|
| $\alpha$ | scaling exponent relating photocurrent to light intensity |
| $a$ | electron/hole pair separation distance |
| $A$ | device absorption |
| $A_{BHJ}$ | absorption in bulk heterojunction |
| $B_{photo}$ | bimolecular recombination rate of photogenerated carriers |
| $BHJ$ | bulk heterojunction |
| $E$ | internal electric field |
| $E_{gap}$ | difference between $HOMO$ and $LUMO$ of organic semiconductor |
| $E_{gap}$ | difference between $HOMO_{donor}$ and $LUMO_{acceptor}$ |
| $\epsilon$ | dielectric constant |
| $G$ | exciton generation rate |
| $HOMO$ | highest occupied molecular orbital |
| $IPCE$ | incident photon to current efficiency |
| $IQE$ | internal quantum efficiency |
| $ITO$ | indium tin oxide |
| $J_0$ | reverse saturation current density |
| $J_{dark}$ | dark current density |
| $J_{light}$ | light current density |
| $J_{n,p}$ | electron/hole current density |
| $J_{photo}$ | photocurrent density |
| $J_{sat}$ | saturated photocurrent density |
| $J_{sc}$ | short-circuit current |
| $k$ | imaginary part of index of refraction or extinction coefficient |
| $k_B$ | Boltzmann's constant |
| $k_f$ | bound electron/hole pair decay rate |
| $LUMO$ | lowest unoccupied molecular orbital |
| $\mu_{n,p}$ | electron/hole mobility |

| | |
|---|---|
| $MDMO-PPV$ | poly(2-methoxy-5-(3',7'-dimethyloctyloxy)-p-phenylene vinylene) |
| $MEH-PPV$ | poly(2-methoxy-5-(2'-ethyl-hexyloxy)-1,4-phenylene vinylene) |
| $n$ | real part of complex index of refraction |
| $N_0$ | density of states |
| $n_d$ | diode ideality factor |
| $\tilde{n}$ | complex index of refraction |
| $nc-ZnO$ | nanocrystalline zinc oxide |
| $OPV$ | organic photovoltaic |
| $P_{CT}$ | probability of exciton dissociation |
| $P_{light}$ | incident light intensity |
| $\phi_0$ | incident number of photons per area |
| $PC$ | photonic crystal |
| $PFPE$ | perfluoropolyether |
| $P3HT$ | poly-3-hexylthiophene |
| $PCBM$ | phenyl-C61-butyric acid methyl ester |
| $PEDOT:PSS$ | poly(3,4-ethylenedioxythiophene):poly(styrenesulfonate) |
| $q$ | elementary charge |
| $R_{fraction}$ | fraction of free carriers that undergo bimolecular recombination |
| $R_{sh}$ | shunt resistance |
| $R_{sr}$ | series resistance |
| $t$ | active layer thickness |
| $T$ | absolute temperature |
| $TDPTD$ | poly(3-(2-methyl-2-hexylcarboxylate) thiophene-co-thiophene) |
| $U$ | net generation rate of free carriers |
| $V_{app}$ | applied voltage |
| $V_{gap}$ | Voltage conversion of $E_{gap}$ |
| $V_{oc}$ | open-circuit voltage |
| $z$ | depth into PC or planar active layer |

# Chapter 1

# Introduction

## 1.1 Meeting the World's Energy Needs

The search for alternative energy sources in the $21^{st}$ century is a growing academic and industrial pursuit. Rising costs of carbon-based fuels coupled with increased emissions and environmental concerns has placed a greater demand on the clean energy sector. In 2005, the world average energy consumption rate per capita was 2.3 kW[1]. From 1990 to 2005 the average use rate nearly doubled in developing countries like China. Given the increasing demand due to rising populations and improved standards of living, it is imperative that new, clean methods of energy conversion be developed to meet the growing needs of humanity.

Compared to other renewable energy sources, the sun is by far the most abundant. This has long motivated research in photovoltaics, also known as solar cells, that convert sunlight into electrical energy. Since the 1950s, the power conversion efficiency (PCE) of these devices has steadily improved. Currently, crystalline silicon and gallium arsenide solar cells have proven efficiencies at or above the 25% level[2]. Furthermore, in a multi-junction configuration, where two or more semiconductors are paired to absorb different regions of the solar spectrum, PCE $> 40\%$ have been achieved[2]. However, a primary limitation of photovoltaics is their relative cost compared to fossil fuels. This led to the development of thin film technologies that use less material, such as amorphous silicon, cadmium telluride, and dye sensitized solar cells, which have PCE $> 10\%$. These and other thin film technologies are also desirable to make solar cells on lightweight substrates that could be used in diverse applications.

Another avenue to thin film photovoltaics was envisioned with the development of conducting polymers in the 1970s[3]. These types of polymers can be doped to demonstrate electrical properties that range from insulating to metallic, all while retaining the desirable mechanical properties of plastic materials, such as flexibility. C.W. Tang is credited with developing the first modern organic photovoltaic (OPV) device in 1986 that consisted of a bilayer

of hole conducting copper phthalocyanine and an electron transporting perylene tetracarboxylic derivative[4]. The PCE of the reported devices were around 1%. Approximately ten years later, the concept of the bulk heterojunction (BHJ) was introduced, where donor and acceptor were mixed in solution prior to deposition. This allowed for distributed donor/acceptor interfaces throughout the BHJ photoactive layer for free carrier creation and therefore circumvented the short exciton diffusion lengths of organic semiconductors[5,6]. Even though the PCE for this new breed of OPV still remained around 1%, the active layer of these devices could be prepared by spincoating from solution instead of through thermal evaporation under vacuum. These results jumpstarted expansive research and inspired the possibility of making solar cells using simple processing techniques from plastic, lightweight, and flexible materials.

With the development of new polymer materials and processing techniques, the PCE had risen to 4.4% by 2005 using an electron donor polymer, poly-3-hexylthiophene (P3HT), and electron acceptor molecule, phenyl-C61-butyric acid methyl ester (PCBM)[7]. Today, this material system remains the most studied and well-understood BHJ solar cell system. Device performance did not stop there as PCE increased to 5.5% in 2007[8], 6.1% and 6.8% in 2009[9,10], and finally to 7.4% in 2010[11]. Not only has progress been hade in academia, but companies such as Solarmer and Konarka claimed 8.1%[12] and 8.3%, respectively, for new polymer systems at the end of 2010. Currently, the race in on to reach the benchmark PCE of 10%. Surpassing this barrier should be possible as indicated by extending different models of BHJ device performance to their limit[13–15].

The explosion of research in this area is exemplified in the numerous review articles on the subject[16–18]. With the passing of time, the field has been categorized into specific areas where comprehensive reviews exist on device physics[19], processing techniques and morphology[20], light trapping cell designs[21,22], charge photogeneration[23], and electrode/interface materials[24].

## 1.2 Bulk Heterojunction Organic Solar Cells: A Primer

### 1.2.1 Device Configuration and Basic Measurement

The most basic device architecture is shown in Fig. 1.1(a) where a BHJ photoactive layer is sandwiched between two electrodes, the top electrode (typically a low work function metal cathode) and bottom electrode (typically a high work function semi-transparent anode). When illuminated with light and placed under short-circuit (i.e. applied voltage ($V_{app}$) = 0 V), photocurrent is produced in the external circuit. This point is labeled as the short-circuit current ($J_{sc}$) on the standard current density vs. voltage (J-V) measurement (Fig. 1.1(b)).

An internal electric field points from cathode to anode under short-circuit conditions due to the energy level difference of the electrodes, which drives photocurrent extraction. Typically, the current density can be further increased by applying negative bias across the device that raises the internal electric field strength. If the current under illumination ($J_{light}$) is subtracted from the current in the dark ($J_{dark}$), then this amount, the photocurrent ($J_{photo}$), will saturate to a level proportional to the amount of light absorbed in the BHJ layer.

As the applied voltage ($V_{app}$) is increased to positive bias, then the extraction of carriers decreases in part due to a decrease in the internal field, but also due to increased injection of holes from the anode and electrons from the cathode (i.e. $J_{dark}$). Under open-circuit conditions, the internal field is very weak and $J_{light} = 0$. With even more application of bias, the current increases rapidly until it becomes linear with a slope controlled by the series resistance ($R_{sr}$) of the device.

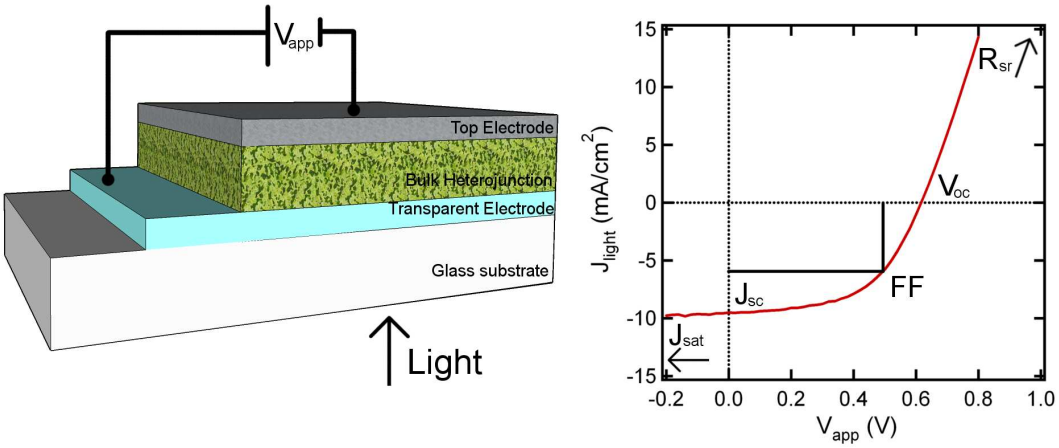


Figure 1.1: (a) Device schematic of BHJ solar cell with top metal electrode (typically cathode) and bottom transparent electrode (typically anode). (b) Standard current-voltage (J-V) curve under illumination. The power conversion efficiency (PCE) is proportional to the product of short-circuit current ($J_{sc}$), fill factor (FF), and open-circuit voltage ($V_{oc}$). With high reverse bias application, the current will saturate to a level proportional to the amount of light absorbed in the active layer ($J_{sat}$). Under positive bias, the current will become linear and act as a resistor with serial resistance, $R_{sr}$.

### 1.2.2 Light Absorption

Under illumination, many processes occur in order to generate $J_{photo}$. The first is light absorption. Semiconducting polymers, including those used in OPV, are characterized by a bandgap, $E_g$, which is the difference between the highest occupied molecular orbital (HOMO) and lowest unoccupied molecular orbital (LUMO). The HOMO and LUMO are analogous to the valence and conduction bands, respectively, used to describe inorganic semiconductors. Conjugated bonds along the backbone of the polymer give rise to one unpaired electron per carbon atom. This delocalizes the electron and gives rise to electrical conduction. In the visible spectrum, photons

with energy above $E_g$ can be absorbed, thereby promoting electrons from the HOMO to the LUMO. Excited states will eventually relax back to the HOMO either non-radiatively or by emitting a photon with energy equal to $E_g$. However, if there is a mechanism, such as an electric field or gradient in carrier concentration, then current can be extracted to the external circuit.

The semiconducting polymers used in OPV are characterized by a wavelength-dependent complex index of refraction ($\tilde{n}(\lambda) = n + ik$) that describes how light interacts with the material. The imaginary part is related to the absorption coefficient via the relation, $\alpha_{abs} = \frac{4\pi k}{\lambda}$. For light with energy above $E_g$ that impinges normal to a thick film with non-zero $\alpha_{abs}$, the generation rate of excited states as a function of depth in the film ($z$) is given by:

$$G(z) = (1 - R)\alpha_{abs}\phi_0 e^{-\alpha_{abs}z} \tag{1.1}$$

where $R$ is the reflection from the film and $\phi_0$ is the incident number of photons per area. While this expression works well for single layers where the thickness is larger than the optical depth, it is not appropriate for thinner films, especially if they are part of a thin film stack adjacent to other layers.

In the case of OPV devices, most have photoactive BHJ layers thinner than the optical depth of the material. Furthermore, the active layers are sandwiched between multi-layer electrodes on both sides, so thin film interference plays a significant role in light absorption. Reflection and transmission occur at each material interface where a device may include four to six layers with a total stack thickness less than 1 $\mu m$. This results in a compound effect of constructive and destructive interference that is wavelength-dependent. When combined with the wavelength-dependence of $\tilde{n}$ for each material in the stack, deviations from the exponential dependence of Eqn. 1.1 result.

Figure 1.2(a) shows normalized $G$ for a BHJ solar cell with P3HT:PCBM as the photoactive layer for different incident wavelengths. Light is incident normal to a glass substrate where the anode, indium tin oxide (ITO) and poly(3,4-ethylenedioxythiophene):poly(styrenesulfonate) (PEDOT:PSS) are the first two thin films on the substrate and serve as typical anode materials for OPV. They have thicknesses of 150 and 40 nm, respectively. Next is the P3HT:PCBM layer with active layer thickness ($t$) of 225 nm. Finally, aluminum is used as the cathode and has thickness of 100 nm. This thickness is enough to stop any light from being transmitted through the device. It is observed in Fig. 1.2(a) that the distribution of absorbed photons depends on the wavelength and is far from exponential due to optical interference.

Light from the sun is a spectrum of wavelenghts and is approximated by a blackbody radiator with temperature

of 5630 K. For each wavelength, a certain fraction of the incident photons will be absorbed in the photoactive BHJ. When integrated across the spectrum and assuming each absorbed photon leads to an electron in the external circuit, the maximum possible $J_{sc}$ can be computed. This is shown in Fig. 1.2(b) for the device structure mentioned above for varying P3HT:PCBM layer thickness, $t$. Due to variations in optical interference, there are oscillations with a maximum around $t = 90$ nm followed by subsequent valleys and peaks.

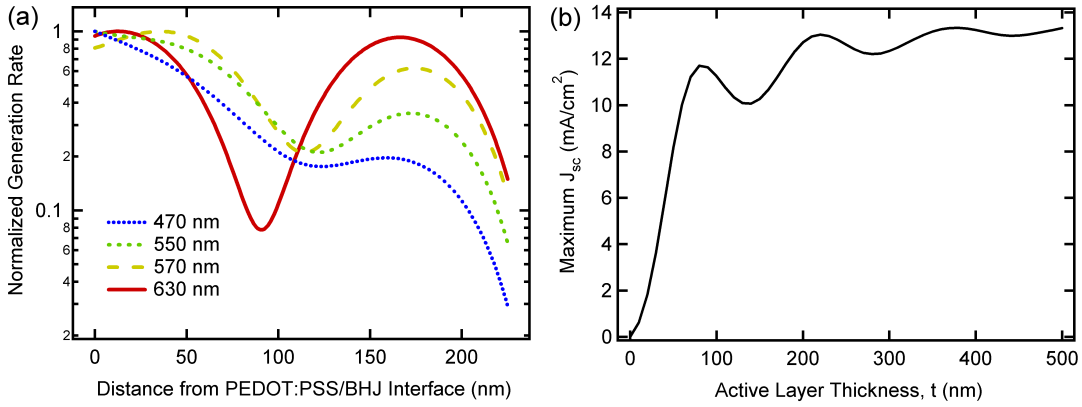


Figure 1.2: (a) Normalized generation rate of excited states, $G$, for different incident wavelengths for a BHJ device with the following structure: glass substrate/ITO (150 nm)/PEDOT:PSS (40 nm)/P3HT:PCBM (225 nm)/Al (100 nm). (b) Maximum $J_{sc}$ as function of active layer thickness, $t$. Here, it is assumed that each absorbed photon in P3HT:PCBM leads to an electron in the external circuit.

The results of Fig. 1.2 are determined via the scattering or transfer matrix method that will be used throughout this thesis. This method takes into account $\tilde{n}$ for all device materials along with optical interference. This model was first applied to organic solar cells in the early 2000s[25,26] and has gained widespread use in the OPV community[27–31]. Input parameters are the layer thicknesses and $\tilde{n}$ of each material layer, which are measured via spectroscopic ellipsometry. The optical properties of both electrode[31–33] and polymer blends[34,35] have been presented in the literature and will be discussed in this thesis.

### 1.2.3 Diffusion of Excitons to Donor/Acceptor Interfaces

Following light absorption, an excited state is created in either the donor or acceptor material. For most material systems, the polymer donor absorbs a majority of the photons, because the common electron acceptor molecule, PCBM, has a higher bandgap and is weakly absorbing. The excited state, or exciton, must diffuse to a donor/acceptor interface where it can then dissociate into free carriers. Because the exciton is charge neutral, it is not influenced by the internal electric field set-up by the device electrodes. Using different variations of photoluminescence quenching, the diffusion length of excitons has been measured in many OPV donor polymers, including P3HT, to be around ∼10 nm and occur on a time scale between 1 ps and 1 ns[19,36,37].

Given this very short diffusion length, it is understood why the first type of OPV devices, those with bilayer architectures, did not yield high photocurrents[16,38]. For these solar cells, the short-lived excitons were not able to reach the interface between the donor and acceptor films. Upon the development of the BHJ concept where donor and acceptor materials were mixed in solution prior to deposition[5,6], the level of photocurrent extraction increased dramatically. This was due to a higher percentage of excitons diffusing to donor/acceptor interfaces that were distributed throughout the film instead of only at the boundaries between pure donor and acceptor layers.

Not only did the development of interpenetrating networks for BHJ devices raise efficiencies, but it also ushered in an explosion of work involving characterization of the nanoscale morphology of BHJ solar cells. It was immediately apparent that device processing during fabrication has a significant impact on morphology and overall performance. For example, if the domain sizes of donor and acceptor are much larger than the diffusion length, then few excitons will be able to reach the donor/acceptor interface to dissociate into free carriers. Processing procedures including choice of solvent, solution concentration, film deposition technique (e.g. spin-coating, drop casting, etc.), and weight ratio of donor and acceptor can each influence morphology[39,40]. A multitude of imaging techniques have been applied to characterize the interpenetrating network of donor and acceptor materials including photoconductive atomic force microscopy[41,42], transmission electron microscopy[43], and near-edge X-ray microscopy[44].

### 1.2.4 Generation of Free Charge Carriers

For excitons that reach the donor/acceptor interface, the end goal is to dissociate into free charges that can be extracted in the external circuit. The process of free carrier generation in BHJ solar cells has been hotly debated and has led to a rich physical picture of photogeneration (see Fig. 1.3)[23]. In the simplest of terms, photogeneration consists of two steps: (1) charge transfer of the electron from the donor to acceptor and (2) dissociation of the charge transfer (CT) state into free carriers.

Via spectroscopic measurements, charge transfer has been shown to be an extremely fast ($\sim$50 fs)[45] and near lossless. This occurs, so long as there is sufficient energy available ($\sim$0.3 eV offset between LUMO of donor and acceptor)[15] for charge transfer. In the case of P3HT:PCBM, the difference in LUMO levels is around 1 eV, providing more than enough energy for charge separation. Unfortunately, this energetic loss also reduces $V_{oc}$.

After charge transfer, the electron and hole are still bound by coulombic attraction. The strength of this attraction varies depending on the donor polymer. Because the electron and hole are physically separated, the

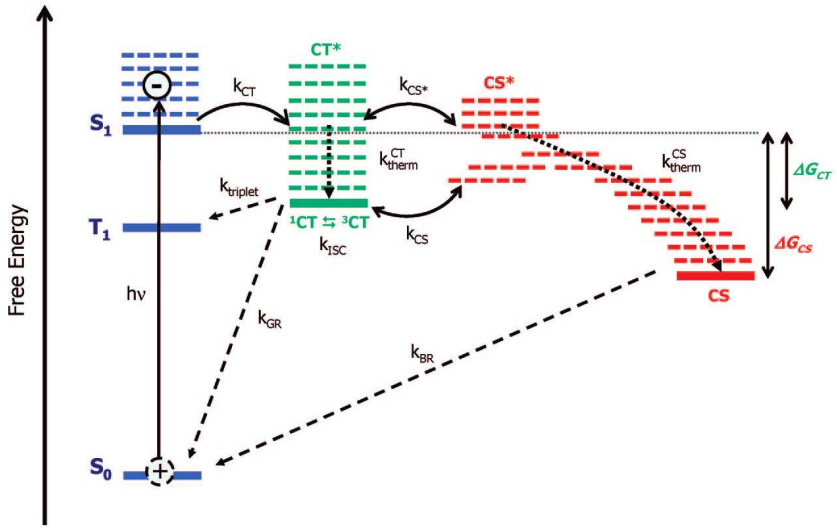


Figure 1.3: The charge transfer (CT) state (green) is bounded by a signlet exciton created by light absorption (blue) and a free charge separated state (red). Thermal relaxation can occur for all three states (dashed lines) where recombination channels exist across all states. Spin mixing is also possible between singlet and triplet CT states. Adaped from review by Clarke and Durrant [23].

dissociation process can be facilitated by an electric field. A field is already built-in due to the work function difference between the two electrodes and can be modulated by applying a voltage across the device. The field-dependence of CT state dissociation, $P_{CT}$, has been described using a model for ion-pair dissociation first proposed by Onsager and later modified by Braun [46], which has been shown to work reasonably well when describing BHJ CT state dissociation of BHJ devices [47].

Not only is the CT state critical to photocurrent generation in BHJ devices, it is also useful to describe the photovoltage. For devices with ohmic contacts, it is understood that the $V_{oc}$ is related to the energy levels of the donor and acceptor through the relation: $V_{oc} = 1/q(E^{HOMO}_{donor} - E^{LUMO}_{acceptor}) - 0.3$ V. This picture has since been improved, where it has been shown that $V_{oc}$ is facilitated through the energetics CT states [48]. Furthermore, the empirical offset of 0.3 V has been linked to temperature-dependent recombination processes within the BHJ layer [49].

### 1.2.5 Transport and Extraction of Free Carriers

As a final step, free charge carriers must be extracted from the device to provide photocurrent that can be used in the external circuit. After dissociation into free carriers, electrons are transported on the acceptor and holes on the donor. Compared to inorganic semiconductors, the carrier mobilities of electrons and holes in BHJ solar cells are low on the order of $10^{-4}$ cm$^2$/Vs. Furthermore, the concept of a bicontinuous network of donor and acceptor materials implies that bottlenecks will exist and restrict carrier transport. Therefore, as with exciton diffusion to

the donor/acceptor interface, morphology is believed to be critical in establishing continuous pathways for carrier transport to the electrodes. This has prompted work in so-called ordered bulk heterojunction devices where donor and acceptor materials exist as pure phases but still in close enough proximity to satisfy the requirements for exciton diffusion[16,50].

Because the carriers are free, it is widely believed that any recombination in transit to the electrodes will be bimolecular in nature (i.e. resulting from different excitons). Compared to most of the recombination pathways in Fig. 1.3 that are for individual excitons and would be monomolecular, bimolecular recombination is a second order process and thus depends on the square of the free carrier concentration. Therefore, this loss process can be probed with light intensity measurements, as will be described throughout this thesis. Significant levels of bimolecular recombination for devices with substantial differences in electron and hole mobilities have been previously observed in BHJ solar cells[51].

As carriers leave the photoactive layer, they still have one final obstacle in the form of carrier transporting layers and electrodes. In ideal situations, these contacts are ohmic and will yield no energetic barriers to carrier extraction that would reduce $V_{oc}$[24,52]. Furthermore, parasitic resistance losses in the form of serial resistance can also play a critical role[53] along with poor interfaces that can lead to fill factors below 25%[54].

## 1.3 Active Layer Thickness: A Trade-off

### 1.3.1 Light Absorption Improves for Thick Active Layers

The primary goal in OPV research is to improve device performance. Therefore, reductions in the losses of any of the physical processes outlined above would boost PCE. From Fig. 1.2, it is observed that increasing the active layer thickness will improve the absorption of light in the photoactive layer. Specifically, increasing $t$ from 50 to 500 nm increases light absorption by 63%. Figure 1.4(a) further supports this where $t$ ($L$ in figure) is increased from 50 to 400 nm[31] for BHJ devices with poly(2-methoxy-5-(3',7'-dimethyloctyloxy)-p-phenylene vinylene) (MDMO-PPV) as the donor polymer. Except for oscillations due to interference, absorption consistently increases as indicated by measurement of $J_{sat}$. This has been seen by others for the same material system[55] and for P3HT:PCBM solar cells as shown in Fig. 1.4(b)[56]. A maximum in $J_{sc}$ occurs for thickness values above 200 nm. Oscillations in absorption are also apparent due to thin film interference, which is a common observation for BHJ devices[30,57–59].

The donor polymers in Fig. 1.4, MDMO-PPV and P3HT, are so-called high bandgap polymers with $E_g$ =

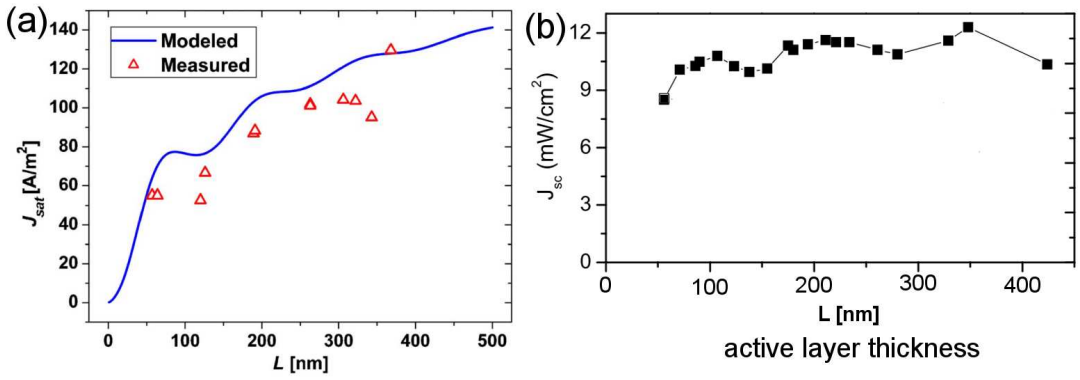


Figure 1.4: (a) Saturated photocurrent ($J_{sat}$) for MDMO-PPV:PCBM devices[31] and (b) short-circuit current ($J_{sc}$) for P3HT:PCBM devices[56] as a function of active layer thickness. The current improves as the thickness is increased. The oscillations are due to interference.

~2 eV. Therefore, photons with wavelengths longer that 650 nm are not absorbed by these materials. Because the sun's maximum photon flux is located around $\lambda = 700$ nm, energy-level engineering via custom synthesis has produced many polymers with broader absorption tails that extend to longer wavelengths[8]. While this has helped polymers absorb extra photons, these materials can also absorb more light if they are made into thicker active layers.

### 1.3.2 Electrical Performance is Better for Thin Active Layers

In spite of this seemingly simple approach to improve device performance, it has been shown that the efficiency of electrical processes will degrade as $t$ is increased. Both electrical mechanisms known to be dependent on the internal field, exciton dissociation and carrier transport, are more efficient for thinner active layers. Figure 1.5(a) shows a prediction of the internal quantum efficiency of MDMO-PPV:PCBM solar cells as a function of $t$. The IQE is a measure of efficiency of all electrical processes in the device and is typically quoted for $V_{app} = 0$ V. The dependence of IQE on active layer thickness is due to the field dependence of exciton dissociation that becomes less efficient as the active layer increases. The internal electric field, $E$, can be approximated as,

$$E = \frac{V_{oc} - V_{app}}{t}, \tag{1.2}$$

so an increase in thicknesses reduces the field, which therefore diminishes the efficiency of exciton dissociation and photocurrent generation. Figure 1.5(b) shows the FF for devices with poly(2-methoxy-5-(2'-ethyl-hexyloxy)-1,4-phenylene vinylene) MEH-PPV as the donor polymer as a function of active layer thickness. As with MDMO-PPV:PCBM, the electrical performance degrades as $t$ increases. For this material system, it is also believed that

exciton dissociation plays a significant role in the electrical performance and is more efficient for thinner active layers where the electric field is stronger.

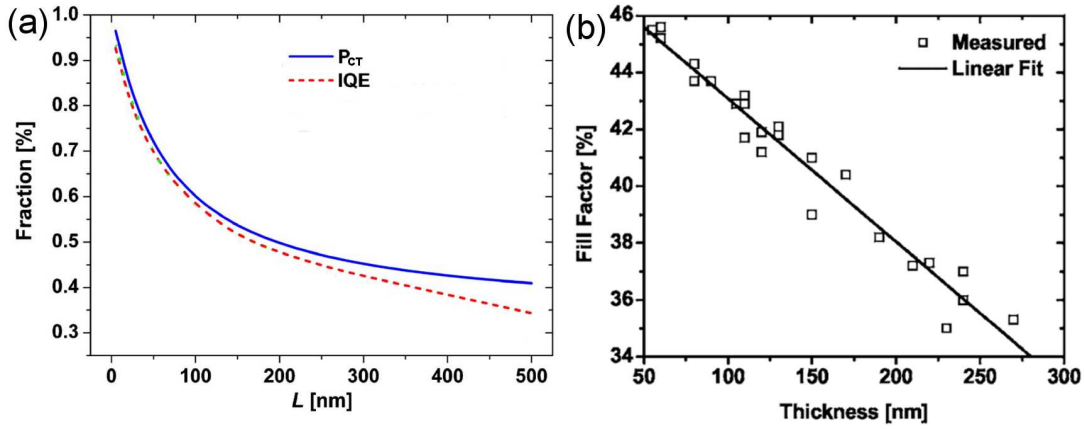


Figure 1.5: (a) Exciton dissociation probability ($P_{CT}$) and internal quantum efficiency (IQE) for MDMO-PPV:PCBM solar cells[31] and (b) FF for MEH-PPV:PCBM solar cells[55] as functions of active layer thickness. For both cases, electrical performance decreases as $t$ is increased.

In terms of free carrier charge transport, increasing the active layer thickness is also believed be detrimental to device performance. The transport length ($L_{n,p}$) of electrons and holes is given by the following,

$$L_{n,p} = \mu_{n,p}\tau_{n,p}E, \tag{1.3}$$

where $\mu_{n,p}$ are the electron/hole mobilities and $\tau_{n,p}$ are the electron/hole lifetimes. When $t$ is increased, not only is the electric field weakened, but it also forces carriers to travel further in order to be extracted. When this is coupled with the mixed phases of the BHJ internal structure, it would seem that free carrier recombination would be a significant loss process in BHJ solar cells.

## 1.4 Photonic Crystals and Transport in OPV

The proposed trade-off in device performance with active layer thickness is a central argument for the development of novel device architectures that could increase light absorption without compromising electrical performance. A majority of this thesis is dedicated to developing OPV devices with photonic crystal (PC) geometries. PC structures (materials with optical properties that are periodic in one, two, or three dimensions on the order of the wavelength of light) have had widespread success in many areas of optics in controlling how light interacts with materials[60]. In this thesis, this concept will be integrated into BHJ solar cells for the first time.

The PC approach is fundamentally different from other light trapping schemes in OPV due to the possibility

of exciting resonant modes in the photoactive layer. These modes are confined to a limited spectral range and should be targeted where the BHJ blend absorbs weakly near the material band edge. Even though optical models of other light trapping approaches have predicted absorption enhancements in specific spectral ranges[61,62], there has been no observation that the photocurrent is actually boosted where absorption is predicted to be enhanced.

Development of this type of solar cell will require new fabrication methods and characterization techniques. Highly ordered arrays of nanopatterns are desired to make PC solar cells. Nanoimprint lithography typically uses Si master molds to construct nanopatterns for OPV[63,64]. However, this process requires great care as Si molds can easily break and are expensive to replace. In order to make light trapping techniques consistent with roll-to-roll fabrication methods, nanopatterning must be done over large areas using simple approaches. Along with fabrication, electro-optical models currently exist for OPV devices with planar active layers[25,26,31,65]. These models must be extended to incorporate the non-planar photoactive layers of PC cells. In extending these models, it may be necessary to include additional materials of the cell that could influence electrical performance. Specifically, interfacial layers in OPV devices can affect parasitic resistance losses and may have an impact on PC performance. These fabrication and characterization objectives will be accomplished in this thesis and set the foundation for future work in light trapping approaches.

Light management techniques, such as the PC method, are justified based on the trade-off in optical and electrical performance. However, the extent to which different donor/acceptor blends suffer from this trade-off remains unclear. As stated above, Fig. 1.5 is for two BHJ blends, MDMO-PPV:PCBM and MEH-PPV:PCBM, where a reduction in electrical performance occurs as $t$ increases. Even though absorption is maximized for $t > 250$ nm, the optimal active layer thickness for these devices is around 100 nm due to electrical restrictions. However, there have been recent accounts of high-performing devices with active layers thicker than $\sim$100 nm. The trademark of good electrical performance is the FF, where values between 55% and 70% indicate efficient electrical function in terms of free carrier generation and transport. For P3HT:PCBM, devices with $t = 425$, 300, and 370 nm have achieved FF values of 62%[56], 55%[66], and 57%[56], respectively. Furthermore, the seminal work on P3HT:PCBM solar cells with PCE = 4.4% had FF values as high as 67%[7]. Surprisingly, these devices also had $t = 220$ nm. Nevertheless, it is commonly argued that the active layer of P3HT:PCBM should be kept around 100 nm in order to reduce electrical losses[29,67]. Furthermore, one of the highest performing BHJ blends to date, PCDTBT:$PC_{70}BM$ (PCE > 6%), has optimal performance for $t < 100$ nm[9].

Given these results, debate continues regarding the optimal active layer thickness for BHJ devices. It appears that the influence of $t$ on PCE is dependent on the material system. All blends, except P3HT:PCBM, have

better electrical performance for thinner active layers where $t = 100$ nm is optimal. One step towards reconciling this debate is realizing that BHJ blends have different affinities for dissociating excitons at the donor/acceptor interface[68]. Figure 1.6 shows $P_{CT}$ for both P3HT:PCBM and MDMO-PPV:PCBM as a function of internal electric field. Squares indicate $P_{CT}$ and the corresponding field at short-circuit for devices with $t = 100$ nm. It is evident that $P_{CT}$ has a much stronger field-dependence for MDMO-PPV:PCBM compared to P3HT:PCBM. At short-circuit, only 2/3 of excitons dissociate at the donor/acceptor interface compared to nearly 90% for P3HT:PCBM[68]. As the electric field is increased under reverse bias, excitons can be more effectively separated, and the photocurrent continues to increase until a saturated level is reached ($J_{sat}$). For P3HT:PCBM, reducing $t$ does enhance the electric field strength, but little gain is achieved in $P_{CT}$ due to its weak field dependence. This offers one explanation why high $J_{sc}$ and FF values have been observed for P3HT:PCBM devices with thicker active layers. Besides P3HT:PCBM, other high performing polymer/fullerene blends, such as PCDTBT:$PC_{70}BM$, have also been shown to have very little loss due to exciton dissociation[9,11] leading to the conclusion that this is a minimal loss process in these solar cells[69].

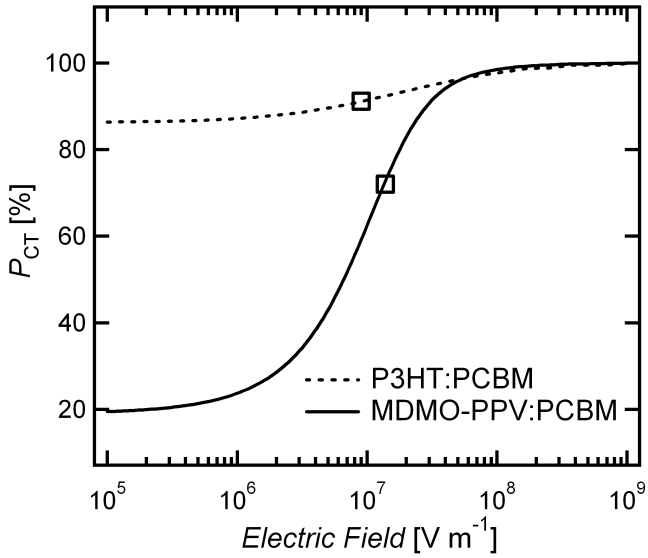


Figure 1.6: Electric field dependence of the probability of exciton dissociation ($P_{CT}$) at the donor/acceptor interface. MDMO-PPV:PCBM has a strong field dependence, while P3HT:PCBM has a weak field dependence. Squares indicate short-circuit conditions.

While this partially reconciles the active layer thickness debate based on differences in exciton dissociation, it does not address this issue with regard to free carrier transport. It has long been argued that increasing $t$ also increases transport losses in the active layer, which reduce electrical performance. Characterizing the ability of free carriers to traverse the active layer is typically done by measuring mobilities using field effect transistor[70] or space charge limited current diodes[71]. While these methods work well to measure mobilities, they rely on

injecting charge from the contacts instead of extracting carriers that were generated by light absorption. In this thesis, a new method that links the local exciton generation profile ($G$) to bimolecular recombination losses (the dominate loss process of free carriers) will be presented. While local absorption profiles have been shown to influence photocurrent extraction[31], they have not been used to measure transport lengths of free electrons and holes. By merging this new understanding of transport lengths of electrons and holes, the debate over the optimal active layer thickness will be clarified. Furthermore, this work will help clarify the impact of charge transport in PC solar cells and guide future light trapping designs.

# Chapter 2

# Optical Properties of Photonic Crystal OPV

## 2.1 Introduction

In general, the disordered nanoscale morphology of organic BHJ solar cells has presented challenges for these devices to reach their full potential. First, BHJ blends have low electron and hole mobilities that have been believed to result in low fill factors[67]. Second, they suffer from a limited probability of exciton dissociation into free charge carriers at the BHJ donor/acceptor interface. For some blends, this is 60% at short-circuit[47]. Both the fill factor[55] and exciton dissociation probability[31] can be increased by reducing the thickness of the photoactive layer, which is beneficial to the electrical performance. However, thinner photoactive layers are antithetical to the absorption of photons, so the result is a fundamental trade-off in photovoltaic design. This is a familiar concept to the design of all solar cells, inorganic included, that has sparked research in light management techniques since it was shown that absorption in a randomly textured sheet could be improved by a factor of $4n^2$[72].

In terms of OPV, many light trapping methods have been recently presented accompanied by optical modeling. Methods utilizing ray optics have been explored in the form of folded substrates[73]. In terms of wave optics, various techniques including anti-reflective multilayer stacks[74], complex scattering structures[75], metallic gratings[62], and optical spacers[27,76] have been theoretically studied. Many of these techniques have predicted an improvement in light absorption, but greater control has been shown theoretically[77,78] and experimentally[79,80] with photonic crystal (PC) architectures in Si solar cells. PC structures have optical properties that are periodic on the order of the wavelength of light. Due to the periodicity, electromagnetic waves are affected in an analogous manner as electron wavefunctions in the periodic potentials of atomic crystals. Many exciting optical phenomena have been predicted for these structures[60], one of which is enhanced coupling of the electromagnetic field to

the structure. Due to the sensitivity of coupling to the PC materials and geometry, the physical parameters of the crystal can be adjusted to produce optical enhancements in a desired wavelength range. For solar cells, wavelengths near the band edge of the photoactive material absorb weakly and are targeted. Until now, PC designs for organic solar cells have had limited visibility, most notably in the form of a bilayer OPV system with a mild index of refraction contrast[81]. There have been no presentations of BHJ systems with PC architectures.

In this chapter, investigations are conducted of the physical dimensions and optical properties of PC solar cells that incorporate the prototypical BHJ blend, P3HT:PCBM, that lead to maximized absorption enhancements. Specifically, both the nanostructure thickness and index of refraction of the low index of refraction conducting material (LICM) that surrounds 1-D and 2-D nanostructured P3HT:PCBM are varied. It is determined that an optimal nanostructure thickness between 200 nm and 300 nm, while the LICM must have an index of refraction ∼0.3 lower than the BHJ blend. Second, the optical properties of resonant or quasiguided modes are presented where it is observed that both broad (short lifetime) and sharp (long lifetime) modes exist in nanostructured devices by comparing spectral absorption to photonic band diagrams. This in-depth analysis is critical, because it is the first prediction of quasiguided modes in organic solar cells, which are not excited in conventional planar cells. These modes have been observed experimentally[82,83] and described theoretically[84] for simple optical systems, but have not been predicted in OPV. Furthermore, profiles of exciton creation for a nanostructured device are presented, which indicate that exciton formation is concentrated in the P3HT:PCBM blend flash layer above the nanostructured layer for quasiguided modes. Finally, simulations of a specific LICM, nanocrystalline ZnO, are presented that represent a near-optimal photonic structure that could be fabricated.

Most of the results and figures of this chapter have been modified from the following publications:

[34]**J.R. Tumbleston**, D.-H. Ko, E.T. Samulski, and R. Lopez, *Electrophotonic enhancement of bulk heterojunction organic solar cells through photonic crystal photoactive layer*, Appl. Phys. Lett. 94, 043305 (2009).

[85]**J.R. Tumbleston**, D.-H. Ko, E.T. Samulski, and R. Lopez, *Absorption and quasiguided mode analysis of organic solar cells with photonic crystal photoactive layers*, Opt. Express 17, 7670 (2009).

## 2.2 Theoretical Approach

### 2.2.1 PC Design

P3HT:PCBM has shown efficiencies approaching 4.5%[7] and is one of the highest performing materials to date in the BHJ class of OPV. Even though ∼100 nm of this blend has very good electrical performance[68], it is still believed to suffer from poorer electrical performance as the thickness is increased[67]. Therefore, any further

improvement in absorption for devices with 100 nm active layers could boost the efficiency beyond 5%. Also, the optical properties of other BHJ blends are very similar to P3HT:PCBM, so many of the results presented here could be applied to these material systems.

The complex dielectric function of P3HT:PCBM and all other device materials are required as input in the optical models presented here. They are measured via spectroscopic ellipsometry as described in Chapter 3. Due to the small phase separation of P3HT and PCBM as a BHJ, it is measured as a homogeneous layer because the phase separation is near two orders of magnitude smaller than the incident light. Figure 2.1 shows the device designs where P3HT:PCBM comprises one of the materials in the nanostructured layer for 1-dimensional (1-D) and 2-dimensional (2-D) periodic PC solar cells. The other nanostructured material is a LICM, which is a transparent electron transport layer with low refractive index compared to P3HT:PCBM ($n_{LICM} \approx 1.4$ for all studies unless otherwise stated). Titanium oxide ($TiO_2$) [29] and nanocrystalline zinc oxide (nc-ZnO) [86] are possible candidates for this material. The glass substrate, ITO, PEDOT:PSS, and LICM have negligible absorption for the spectral range of interest ($400 \leq \lambda \leq 685$ nm) and are taken to be fully transparent. On the other hand, the Al cathode is modeled with its true complex dielectric function, so optical losses do occur in this material. All absorption plots presented describe the fraction of incident light that is absorbed in the P3HT:PCBM only, where an absorption value less than 1 signifies loss from absorption in the Al or reflection/scattering. P- and s-polarized light are incident normal to the relatively thick (1 mm) glass substrate where reflection from the air-glass interface is disregarded. This loss is 4% and approximately constant for all wavelengths.

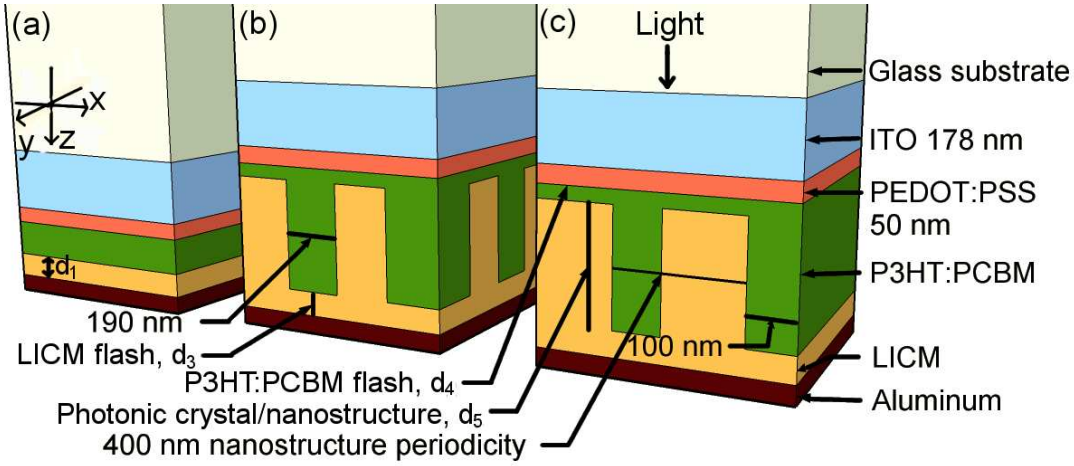


Figure 2.1: Illustration of three photovoltaic devices studied: (a) Conventional planar control stack, (b) 2-D periodic posts with 395 nm square periodicity, and (c) 1-D periodic channels with 400 nm periodicity. S- and p-polarized light have electric fields oriented in y- and x-directions, respectively. The LICM planar film thickness, $d_1$, LICM flash thickness, $d_3$, P3HT:PCBM flash thickness, $d_4$, and nanostructure thickness, $d_5$, will be changed for optimization while all labeled values remain constant. The sum of $d_3$ and $d_5$ is represented as $d_2$, which is not used in this chapter but is cited extensively in Chapter 3. In that chapter, $d_2$ may be less than the sum of $d_3$ and $d_5$ resulting in a wavy top electrode. This effect is ignored in this chapter.

### 2.2.2 Calculation Method

The photonic properties of the PC BHJ devices discussed in this paper are studied using transfer and scattering matrix methods with plane wave expansions[84,87]. Codes in *Mathematica* have been developed as part of this thesis, where the accuracy is demonstrated in the Appendix. The scattering matrix method is a fast algorithm that calculates the optical properties and quasiguided eigenmodes in periodic PC slabs of finite thickness. Maxwell's equations are solved as an eigenvalue problem via plane-wave decomposition in two-dimensional Cartesian coordinates, and the solution is propagated across the different layers by means of scattering matrices, which define the continuity conditions for electromagnetic field components at each interface. The periodic symmetry of the proposed photonic structures makes them especially suitable for this approach. The in-plane periodicity of the structure is represented by the Fourier transform of the piecewise dielectric permittivity. From this formulation, the reflection, transmission, absorption, and scattering coefficients are calculated for the entire stack for both s- and p-polarized light.

Along with these coefficients, the electromagnetic field profile inside the device is required to determine the location and density of exciton creation that follows the energy dissipation profile, $Q(x,y,z)$. In conventional planar devices, the field and energy dissipation profiles are only functions of depth in the device, $z$, and time[25,26]. For nanostructured designs, $\langle Q \rangle$ is a function of all spatial dimensions and is derived from Poynting's time-averaged continuity equation,

$$\langle Q \rangle + \nabla \cdot \left\langle \vec{S} \right\rangle = 0 \tag{2.1}$$

where $\left\langle \vec{S} \right\rangle$ denotes the time-averaged Poynting vector. This equation leads to the time-averaged monochromatic pointwise energy dissipation per unit time per unit area,

$$\langle Q \rangle = \frac{\pi c \epsilon_0 \epsilon_2 \left| \vec{E} \right|^2}{\lambda} \tag{2.2}$$

where $\epsilon_2$ is the imaginary part of the dielectric function, $\epsilon_0$ is the permittivity of vacuum, $c$ is the speed of light in vacuum, $\lambda$ is the free space wavelength, and $\left|\vec{E}\right|$ is the magnitude of the complex optical electric field. To calculate $\langle Q \rangle$, the fields are needed over a high resolution mesh in the unit cell. Using the transfer method[84], this can be done by first solving for the plane-wave amplitudes for the entire structure,

$$\begin{pmatrix} F_{sub}^{+} \\ F_{sub}^{-} \end{pmatrix} = T_{tot} \begin{pmatrix} F_{inc}^{+} \\ F_{inc}^{-} \end{pmatrix} \tag{2.3}$$

where the column vectors are the amplitudes in the substrate and incident semi-infinite spaces connected via the system transfer matrix, $T_{tot}$, and plus (minus) refers to propagation toward (away from) the stack. The amplitudes can be calculated to a given depth in the z-direction in Fig. 2.1 in the structure, $z_0$, by using $F_{inc}^{\pm}$ from Eqn. 2.3 and the transfer matrix calculated to the point of interest, $T_{z_0}$,

$$\begin{pmatrix} F_{z_0}^{+} \\ F_{z_0}^{-} \end{pmatrix} = T_{z_0} \begin{pmatrix} F_{inc}^{+} \\ F_{inc}^{-} \end{pmatrix} \tag{2.4}$$

Energy dissipation is proportional to the exciton generation rate, $G$, so $\langle Q \rangle$ may be thought of as the exciton creation profile in the photoactive region in this chapter. In the case of P3HT:PCBM, a large fraction of excitons will create free electrons and holes[68]. Therefore, the exciton creation profile gives the proximity and density of exciton formation within P3HT:PCBM along with an approximate profile of free carrier generation. An exciton generation profile is generated at each depth in the P3HT:PCBM flash layer and nanostructured layer, so this profile may be integrated to compare absorption at various depths for different wavelengths and polarizations.

In later chapters of this thesis, $G$ will be input in an electrical transport model of BHJ solar cells[65]. For planar devices, this model is one-dimensional, but it will be extended to higher dimensions to appropriately describe the PC geometry. This will provide a means to simulate performance factors such as $J_{sc}$, FF, $V_{oc}$, and PCE with regard to an altered static internal electric field for the PC structure.

As a final note, numerical issues can arise for certain systems when using the transfer method. Mathematically, it has been shown that the transfer and scattering methods are equivalent[84], but exponentially growing transfer matrix entries can occur that lead to numerical instability. This must be checked for a given system before using the transfer method to determine the electromagnetic fields and thus exciton creation profiles in the nanostructured photoactive region.

## 2.3 Absorption Analysis

The physical dimensions and optical properties of the nanostructured layer for the devices in Fig. 2.1 greatly affect absorption in the BHJ blend. The parameters presented here will be directly applicable to nanostructured

devices with P3HT:PCBM as the photoactive material even though some general trends can be applied to other photoactive materials. First, there are considerations regarding the volume of P3HT:PCBM in the nanostructured and planar control devices. In order to compare a nanostructured device to control cell, the volume of P3HT:PCBM available for the nanostructured cell must equal the planar control blend volume. This volume restricts the possible periodicities and thicknesses of the nanostructured region along with the thickness of the P3HT:PCBM flash layer. Typically, a P3HT:PCBM thickness for a flat conventional device with an optical spacer layer is ∼100 nm [29,58] due to balanced optical and electrical performance for this thickness. The goal is to enhance the absorption of a planar device with this approximate thickness using a PC photoactive layer.

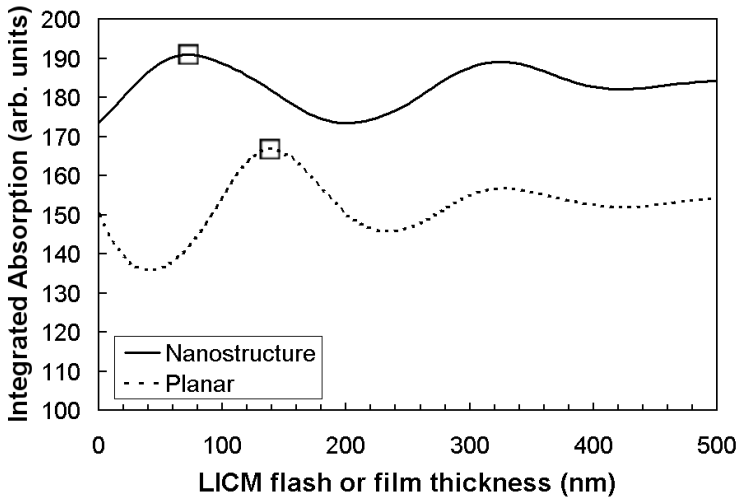


Figure 2.2: Integrated absorption for varying thicknesses of LICM flash layer, $d_3$, for the 2-D periodic device and LICM optical spacer film, $d_1$ for planar control. Comparisons between PC and planar control devices are made for LICM thicknesses that result in maximum integrated absorption (squares).

Interference also plays a major role in absorption for thin film stacks where the total stack thickness is comparable to the wavelength of light. Varying thicknesses of any non-absorbing layer (ITO, PEDOT:PSS, or LICM) will cause the P3HT:PCBM absorption to fluctuate, so it is necessary to vary one of these thicknesses to maximize integrated absorption for both the nanostructured and planar control cells. Here, ITO (178 nm) and PEDOT:PSS (50 nm) thicknesses are kept constant for all studies in order to compare devices more closely with literature. Instead, the LICM flash thickness, $d_3$, for the nanostructured device and the LICM film thickness for the control cell, $d_1$ are varied from zero to 500 nm. For each thickness of LICM, the spectral absorption is integrated between $400 \leq \lambda \leq 685$ nm resulting in Fig. 2.2 for the 2-D periodic device with P3HT:PCBM flash thickness, $d_4 = 40$ nm, and nanostructured layer thickness, $d_5 = 300$ nm. The oscillation in integrated absorption occurs primarily due to interference where the electromagnetic field has varying strengths in the photoactive region. A correct optical comparison is made between nanostructured and planar control devices when both

curves are maximized (as indicated by squares in Fig. 2.2). Integrated absorption is always greater for the nanostructured device, but using the lowest integrated absorption value for the planar device would result in incorrect and exaggerated absorption enhancements.

The first parameter to optimize is the ratio of P3HT:PCBM flash thickness, $d_4$, to nanostructure thickness, $d_5$. Keeping in mind that the goal is to enhance absorption for planar control devices with ∼100 nm thick P3HT:PCBM layers, both $d_4$ and $d_5$ are simultaneously varied for the 1-D periodic device while keeping all other parameters equal to those in Fig. 2.1(c). Here, the volume of P3HT:PCBM remains constant for each step in the optimization and equal to a control device with a P3HT:PCBM thickness of 115 nm. As previously discussed, the integrated absorption fluctuations due to interference are maximized for both nanostructured and planar control cells before calculating absorption enhancements. Fig. 2.3(a) shows absorption enhancements for s-, p-, and average polarization as a function of $d_4$ and $d_5$. Due to the 1-D periodicity, s-polarization is more enhanced by the nanostructure than p-polarization. It can also be seen that a thin P3HT:PCBM flash layer with a thick nanostructure gives larger enhancements in absorption where the maximum for average polarization occurs for $d_4 = 15$ nm ($d_5 = 400$ nm). This would be the optimal value, but the fill factor has been shown to drop for very thin planar P3HT:PCBM cells with a photoactive thickness below ∼40 nm possibly due to decreased shunt resistance[57]. Even though the absorption enhancement drops around $d_4 = 60$ nm and increases to another maximum for $d_4 = 80$ nm, the flash layer value of $d_4 = 40$ nm is taken as optimized as it has the highest integrated absorption excluding the thin regime.

The thickness of the nanostructured region is another important parameter to optimize. Figure 2.3(b) shows absorption enhancements for nanostructure thicknesses, $d_5$, from 100 to 500 nm for the 1-D periodic device with the optimized P3HT:PCBM flash thickness, $d_4 = 40$ nm. Varying the nanostructure thickness changes the volume of P3HT:PCBM, so each device is compared to a planar control cell with equivalent volume. This shows that there exists a wide range of nanostructured layer thicknesses where absorption enhancements are observed. The p-polarized enhancement is maximized for $d_5 = 220$ nm while s-polarization is maximized for $d_5 = 290$ nm. Averaging the two polarizations produces an enhancement of 13% for $d_5 = 210$ nm. There is also reduced integrated absorption for thin ($d_5 < 130$ nm) and thick ($d_5 > 420$ nm) devices. Thicker nanostructures have reduced enhancement factors, because they are compared to planar control devices with thicker P3HT:PCBM film layers. For example, the nanostructured device with $d_5 = 500$ nm is compared to a planar control cell with 165 nm P3HT:PCBM film thickness, which is able to absorb a higher number of solar photons in the spectral range. In the case of thinner nanostructures, they do not produce the optical effects that lead to photonic enhancement.

It is not shown here, but the 2-D periodic device is optimized for $d_5 = 300$ nm.

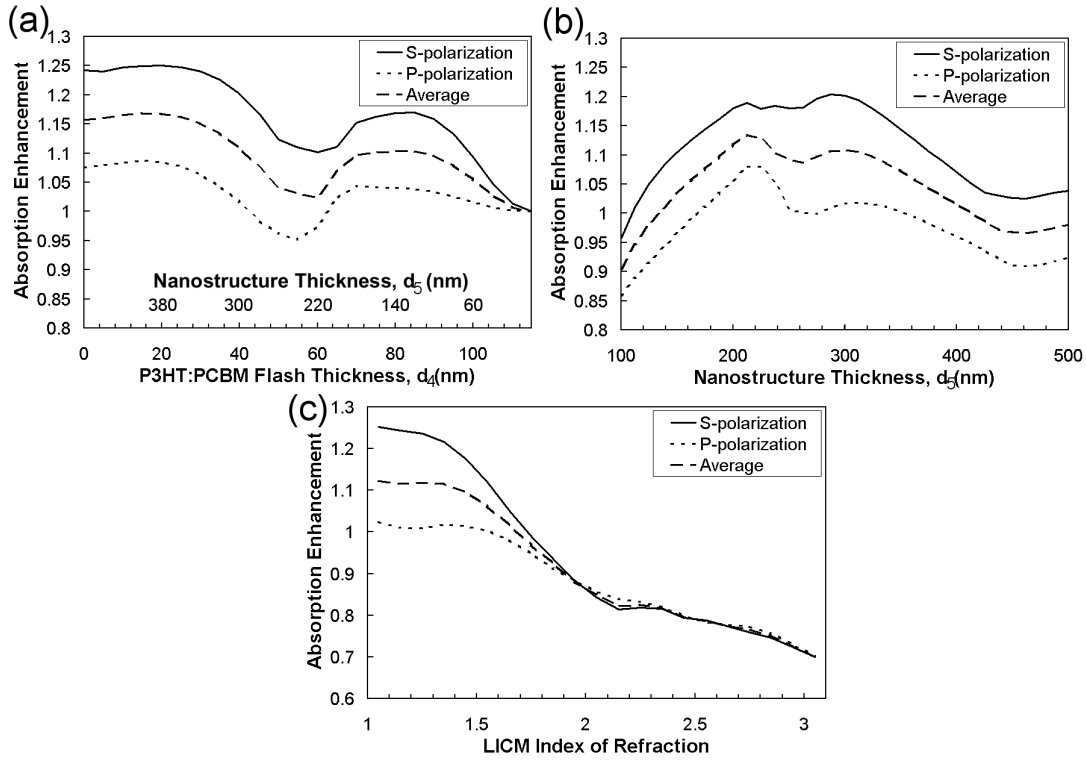


Figure 2.3: Integrated absorption enhancements for variable (a) P3HT:PCBM flash thickness, $d_4$, and nanostructure thickness, $d_5$, (b) nanostructure thickness, $d_5$, and (c) LICM index of refraction of the nanostructured layer. The 1-D periodic device design is used in each optimization.

The final physical parameters to discuss are unit cell periodicity and P3HT:PCBM nanostructure width. Choices are motivated by the desire to produce strong absorption enhancements near the band edge of P3HT:PCBM due to its weak extinction coefficient in this spectral range. A primary way to produce these enhancements is through quasiguided or resonant mode excitation. These modes provide ∼20-fold enhancements for certain energy photons and will be discussed later in detail. Furthermore, as with nanostructure thickness, unit cell periodicity and nanostructure width also affect the thickness of P3HT:PCBM in the planar control cell. Values that give thick planar P3HT:PCBM layers are not desired, because these result in minimal absorption enhancements. The periodicity and index of refraction contrast (discussed below) provide the most control of the enhancement factors and spectral placement of quasiguided modes.

In terms of optical properties, the contrast in the dielectric functions of the two PC materials in the nanostructured layer (P3HT:PCBM and LICM) has the greatest effect on overall absorption. A high contrast in the real part of the refractive index between these materials is desired to make a true PC and to excite quasiguided modes. This is also a desirable trait for producing photonic band gaps in other systems[60]. To illustrate this concept, the LICM index is varied from $n = 1.05$ to 3.05 for the 1-D periodic device with $d_4 = 40$ nm and $d_5 = 300$ nm.

Figure 2.3(c) shows that the greatest enhancements occur when the LICM index of refraction is closest to unity and steadily decreases for increasing index. The average index of refraction of P3HT:PCBM for $400 \leq \lambda \leq 685$ nm is 1.94, so a minimum difference of $\sim$0.3 is needed between the two materials to produce enhanced integrated absorption. As with the above optimizations, there are larger absorption enhancements for s-polarization than for p-polarization. Furthermore, the LICM index must be lower than that of P3HT:PCBM. Even though the difference in index also exceeds 0.3 for LICM index values above 2.25, there is reduced absorption when compared to the planar control devices. Increasing the index to values greater than that of P3HT:PCBM causes greater reflection from the device due to sharper changes in the index from layer to layer. Quasiguided modes can still be coupled for large indices of refraction, but these enhancements are overshadowed by losses from greater reflection.

## 2.4 Quasiguided Modes and Band Structure Analysis

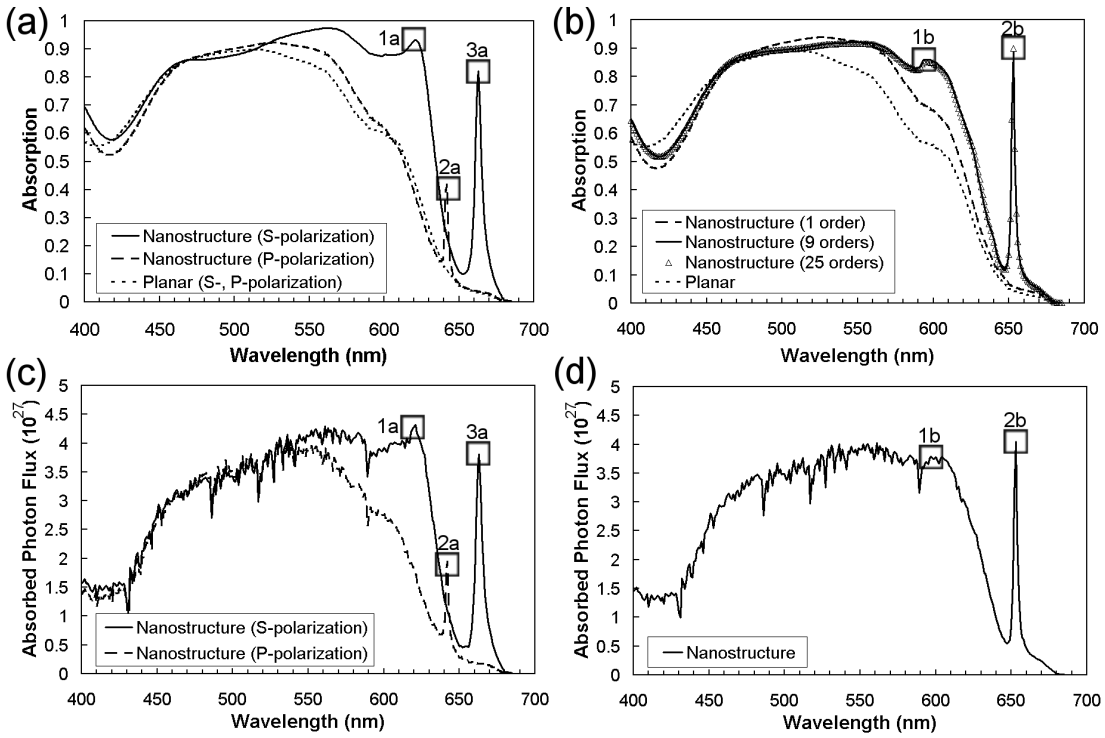


Figure 2.4: Normal incidence absorption spectrum for (a) 1-D and (b) 2-D periodic nanostructured devices and comparable planar cells for both polarizations. P- and s-polarization for the 2-D periodic device are equivalent due to square symmetry. Quasiguided modes are labeled 1a, 2a, and 3a for the 1-D periodic cell, while modes for the 2-D periodic device are referenced 1b and 2b. Convergence of the solution method is also shown in (b) for one, nine, and twenty-five diffraction orders. The solution using one order corresponds to the main zeroth order. The AM 1.5 absorbed flux of solar photons ($\frac{1}{m^3 s}$) is presented for the (c) 1-D and (d) 2-D periodic cells to demonstrate the interplay between device absorption and the solar spectrum.

With the above noted set of physical parameters and optical constants, quasiguided modes are excited in the nanostructured solar cells. These modes are externally excited by incident light[84] and lead to sharp en-

hancements in absorption. Three quasiguided modes are shown in Fig. 2.4(a) in the normal incidence absorption spectrum for the 1-D periodic device that is near-optimal for s-polarized absorption ($d_3$ = 70 nm, $d_4$ = 40 nm, $d_5$ = 300 nm). The modes are labeled 1a, 2a, and 3a for reference. Furthermore, the optimal 2-D periodic device ($d_3$ = 75 nm, $d_4$ = 40 nm, $d_5$ = 300 nm) exhibits two modes at normal incidence as shown in Fig. 2.4(b). The quasiguided mode located at $\lambda = 652$ nm (mode 2b) is very sharp and offers an 18-fold absorption enhancement. Another mode exists further from the band edge at $\lambda = 595$ nm (mode 1b) that has a broader absorption spike. Mode excitation can also be observed when absorption is multiplied by the AM 1.5 solar photon flux[88] as shown for the (c) 1-D and (d) 2-D periodic devices. The solar photon flux reaches a maximum around $\lambda = 700$ nm, so the quasiguided mode excitations provide strong absorption near the highest flux region of the solar spectrum even though the extinction coefficient of P3HT:PCBM is small close to the band edge.

Figure 2.5 shows the photonic band structure for the (a) 1-D and (b) 2-D periodic nanostructured devices. The observed modes in the absorption spectra of Fig. 2.4 for the Γ-point where $kx = ky = 0$ (normal incidence) are noted. The band diagrams are calculated by locating where the determinate of the scattering matrix for the system diverges[84]. This occurs for certain complex wavelengths. The imaginary part is related to the mode lifetime where modes with broader spectral width have shorter lifetimes. An absorption spike with no width would indicate an infinitely trapped waveguided mode. In the case of the 2-D periodic device, mode 1b is confirmed to have a larger imaginary part (shorter lifetime) than mode 2b by an order of magnitude, which is indicated by its broader spike in absorption.

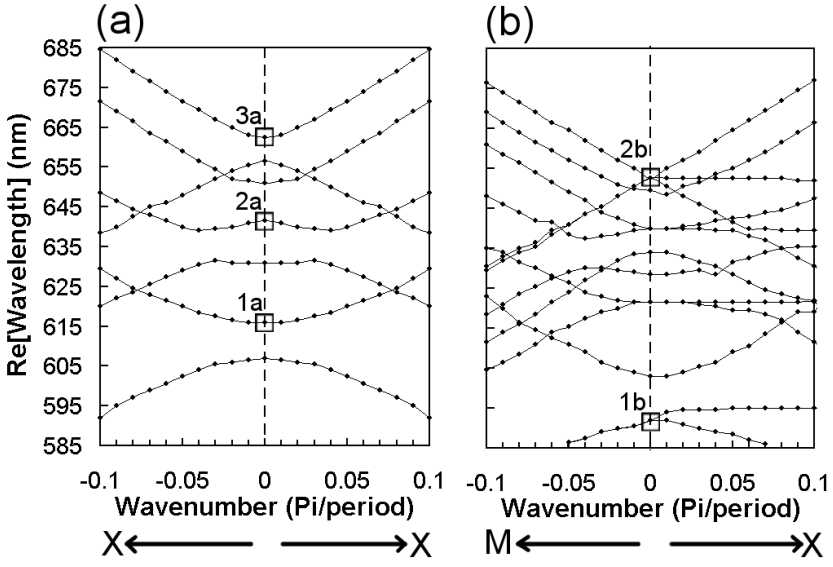


Figure 2.5: Photonic band diagram for the (a) 1-D and (b) 2-D periodic nanostructured devices. Bands corresponding to optically active modes that result in quasiguided mode spectral absorption spikes for the Γ-point are referenced.

Figure 2.5(b) also indicates that there is two-fold and three-fold degeneracy at the Γ-point for the 2-D periodic device for the 1b and 2b modes, respectively. This degeneracy can be broken with non-normal incidence ($kx \neq 0$) giving rise to two s-polarized modes and one p-polarized mode for the case of mode 2b. Further comparison of the spectral absorption (Fig. 2.4) with the band diagrams (Fig. 2.5) also reveals that there are more bands than quasiguided modes that lead to absorption spikes. The bands resulting in absorption peaks are known as optically active modes, while those that do not are inactive[84].

Figure 2.4(b) also shows the convergence of the method, which helps characterize both quasiguided mode excitation and absorption enhancements. As previously mentioned, the simulation method used for solving Maxwell's equations is an approximation scheme that must be truncated after a certain number of terms in the Fourier series solution. These also correspond to a certain number of diffraction orders in Fourier space. After some number of orders, the solution converges. Taking only the zeroth order means that the nanostructured layer is treated as a homogeneous layer where the optical properties of the two materials (P3HT:PCBM and LICM in this case) are averaged by a weight proportional to their volume. It is clear that some of the overall absorption enhancement occurs for this order near the band edge. The physical process of scattering is not included for the zeroth order, so the enhancement only involves interference over a longer depth than for the planar case. It is also observed that the quasiguided modes are not excited, because they require the incident beam to exchange k-vectors with contributions in the lateral directions of the reciprocal lattice.

## 2.5 Exciton Creation Profiles

Along with studying the absorption and photonic band properties of these devices, the optical model can be further extended to determine the electromagnetic fields inside the photoactive region. This results in the profile of exciton creation, $\langle Q \rangle$, for the nanostructured and planar devices. The profiles are calculated at a given depth, $z$, where each slice varies over the two lateral dimensions, $x$ and $y$. Fig. 2.6(a) shows the profile for one unit cell of the 2-D periodic device ($d_3$ = 75 nm, $d_4$ = 40 nm, $d_5$ = 300 nm) at a depth of $z$ = 150 nm into the nanostructured layer for $\lambda$ = 550 nm. There is no energy dissipation around the post, because the LICM is transparent.

Major differences in absorption profiles occur for wavelengths in and out of quasiguided mode resonances. Integrating the exciton creation profiles (Fig. 2.6(a)) over the lateral dimensions for each depth in the P3HT:PCBM flash and nanostructure layers yields Fig. 2.6(b) for both $\lambda$ = 652 nm (quasiguided) and $\lambda$ = 550 nm (non-

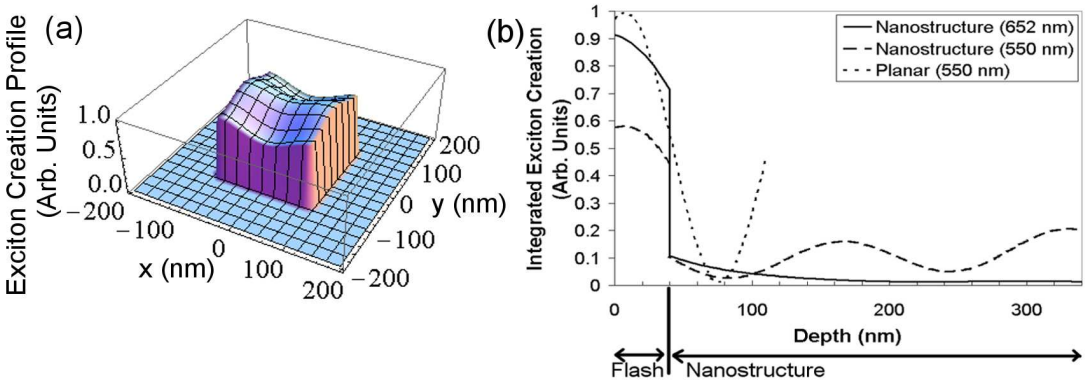


Figure 2.6: (a) Exciton creation profile of one unit cell for the 2-D periodic device at a depth, $z = 150$ nm, into the nanostructured layer for $\lambda = 550$ nm. (b) Integrated exciton creation profile as a function of depth, (z-direction), for the 2-D periodic device for $\lambda = 550$ nm (general absorption) and $\lambda = 652$ nm (quasiguided mode 2b). The integrated exciton creation profile for the comparable planar device is also shown for $\lambda = 550$ nm.

quasiguided). Discontinuity occurs at the flash/nanostructure interface, because the complex dielectric function changes at the boundary due to the inclusion of both P3HT:PCBM and LICM in the nanostructure layer. From Fig. 2.4(b), both wavelengths yield comparable absorption (∼90%) even though the former is due to quasiguided mode excitation and the latter results from the high extinction coefficient of P3HT:PCBM. Fig. 2.6(b) shows that absorption as a function of depth is oscillatory in the nanostructured layer for $\lambda = 550$ nm, while it decays with depth for the quasiguided mode. The most striking feature is that greater absorption takes place for the quasiguided mode in the flash layer than for $\lambda = 550$ nm. Quantitatively, 79% of excitons are created in the P3HT:PCBM flash layer for $\lambda = 652$ nm, while only 39% are created there for $\lambda = 550$ nm. This may cause improved electrical performance for quasiguided modes due to high absorption in the thin $d_4 = 40$ nm flash layer where free carrier transport paths are relatively short.

Figure 2.6(b) also shows the integrated exciton creation profile for $\lambda = 550$ nm for the planar control device. For this wavelength, there is a greater concentration of excitons created toward the PEDOT:PSS side than the LICM layer. The depth where this concentration occurs will vary for different wavelengths, but the general shape of the curve is similar as has been shown in previous studies[26,58].

## 2.6 Case Study: Nanocrystalline ZnO as LICM Material

### 2.6.1 Motivation for Using Nanocrystalline ZnO

Thus far, the low index conductive material (LICM) has remained general and has not been cited as a specific material. In this section, nanocrystalline zinc oxide (nc-ZnO) is used as the LICM due to its low refractive

index compared to P3HT:PCBM ($n \sim 1.5$ as will be shown in Chapter 3) and proven electrical properties. In other studies, nc-ZnO has been used in photovoltaic cells as an optical spacer [58], an electron transport layer [89], a high electron mobility film [90], and an improved electrical contact for metal cathodes [91]. In terms of device preparation, nc-ZnO would be formed by spin-coating a dispersion of freshly synthesized [86] nanoparticles (∼5 nm diameter particles) in methanol on both the PC and planar photoactive strata. Although an IR-VIS-transparent material, the nc-ZnO layer can affect the absorption characteristics of the cell via interference effects as shown above, so it is critical to simulate planar cells with varying spacer thickness and PC cells with a range of nc-ZnO flash thicknesses, $d_1$ and $d_3$ from Fig. 2.1, respectively. In this section, comparisons are only made between absorption spectra that show maximum integrated absorption for both PC and planar cells.

### 2.6.2 Absorption Enhancements

Figure 2.7 shows the geometry and dimensions of PC and planar designs that are similar to those in Fig. 2.1. The given dimensions are optimal as determined in the section above. In terms of absorption, Fig. 2.8 shows the sharp enhancements in P3HT:PCBM absorption near the band edge of this material that are characteristic of resonant modes discussed previously. Excitation of these modes is solely a consequence of the PC topography of the PV layer with high index of refraction contrast. Furthermore, there are enhancements across the whole spectrum ($\lambda = 400$ to 685 nm) for both the 1-D and 2-D periodic device designs that result in integrated 20% (s-polarization) and 14% (both polarizations) enhancements, respectively. Multiplying the absorption by the AM 1.5 solar spectrum as in Fig. 2.4 in this spectral range and integrating causes essentially no change in the enhancement factors.

Exploiting the light management offered by a PC, the height and periodicity are chosen to provide enhancements near the band edge of P3HT:PCBM as described in the optimization sections above. The polarization also has a strong dependence as shown in Fig. 2.8(a) for the 1-D periodic device where there is only a 2% integrated spectral increase for incident light that is p-polarized (electric field perpendicular to the periodicity in x-direction) compared to 20% enhancement for s-polarization. Furthermore, the incident angle plays a role in quasiguided mode excitation as shown in Fig. 2.8(b) where s-polarized absorption is calculated at 2 degree incidence. It is clear that mode excitation is dependent on the incident parameters and device optical and physical properties. In terms of simulation details, it should be noted that the glass substrate, ITO, PEDOT:PSS, and nc-ZnO are taken to be transparent over the entire spectral range. Also, the 1-D and 2-D periodic designs are tailored to improve performance over control devices with blend thicknesses of ∼100 nm, as was the goal stated previously.

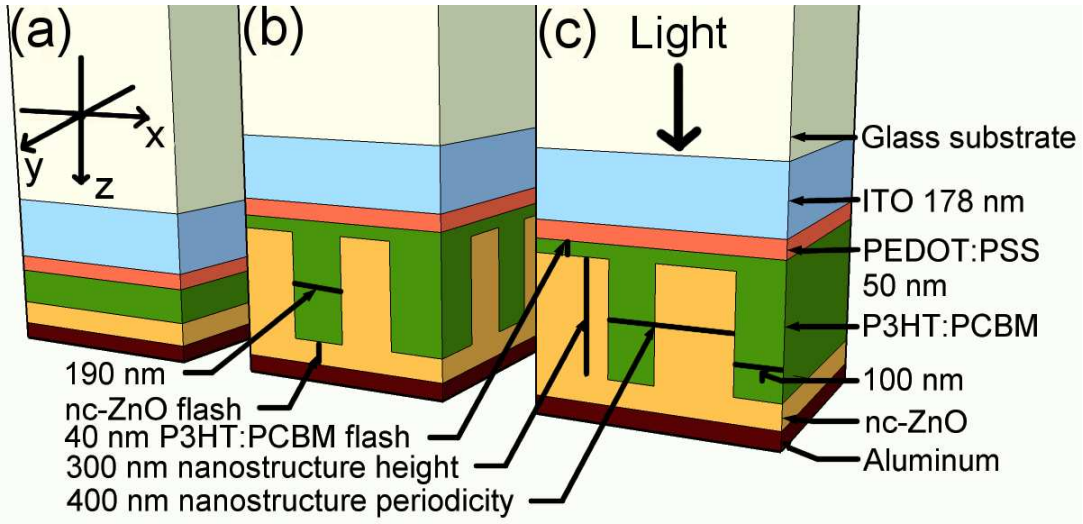


Figure 2.7: Illustration of three organic photovoltaic device designs with nc-ZnO as the LICM: (a) Conventional planar PV stack (control device), (b) square posts with 395 nm 2-D square periodicity, and (c) channels with 400 nm 1-D periodicity.

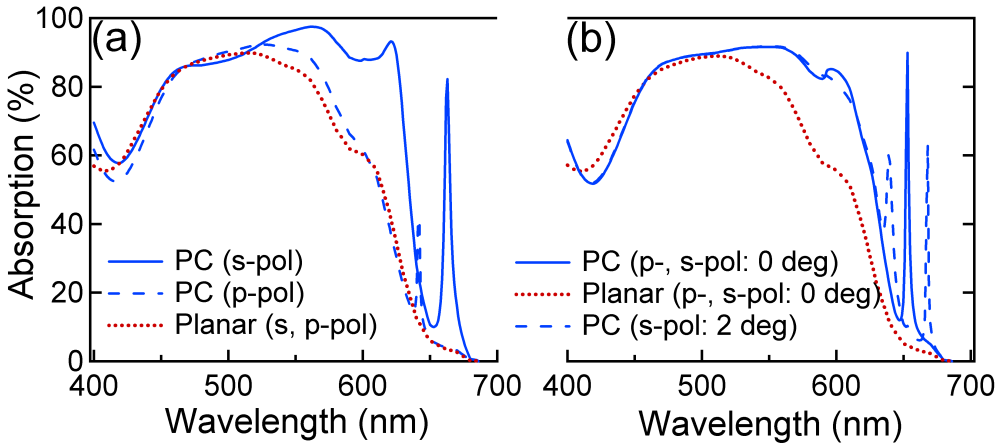


Figure 2.8: (a) Theoretical spectral absorption at normal incidence for 400 nm 1-D periodic PC device compared to planar control cell for both s- and p-polarized light. (b) Spectral absorption for 395 nm 2-D periodic posts at both normal incidence (both polarizations) and 2 degree incidence (s-polarization only).

### 2.6.3 Exciton Creation Profile

Along with the absorption enhancements shown above, it is found that excitons in PC cells are created closer to nanostructured P3HT:PCBM exit interfaces (with either the PEDOT:PSS or nc-ZnO) than in planar cells. Calculating the proximity of exciton creation to exit interfaces provides a rough estimate of potential electronic transport enhancements in the PC device even though no electronic processes are considered. Here, only one creation distance is considered, while in Chapter 5 separate creation distances for electrons and holes are shown to be a more valuable figure of merit. In general, the exciton creation profile is given by the time-averaged monochromatic pointwise energy dissipation per unit time per unit area, $\langle Q \rangle$, from Eqn. 2.2.

The exciton creation profile for one unit cell for the 1-D periodic PC device for $\lambda = 550$ nm at a depth of $z = 150$ nm into the 300 nm nanostructured layer is given in Fig. 2.9(a) to show how local absorption varies over the lateral directions, $x$ and $y$. There is no absorption around each channel, because they are surrounded by transparent nc-ZnO. By weighting the profile against the shortest distance, $l$, to a P3HT:PCBM blend exit interface with either the PEDOT:PSS or nc-ZnO, the exciton creation distance (ECD) for a given incident wavelength, angle, and polarization can be determined:

$$ECD = \frac{\int_V \langle Q \rangle \cdot l \cdot d\tau}{\int_V \langle Q \rangle \cdot d\tau} \tag{2.5}$$

where the integrals are taken over one unit cell of the entire photoactive P3HT:PCBM volume (flash and nanostructure).

ECD values are shown over the entire spectrum for the 1-D periodic structure at normal incidence in Fig. 2.9(b). It is noticed that the greatest reductions occur toward the blue spectral end where absorption is essentially equal between PC and control devices (Fig. 2.8). The comparable ECDs become closer near the band edge where absorption is stronger for the PC device. Ultimately, this could indicate an overall improved PV performance for the entire spectrum either due to shortened ECDs (blue end) or stronger absorption (red end). The presence of the quasiguided modes is again realized with this calculation where sharp reductions are visible. These modes have the effect of concentrating absorption in the thin P3HT:PCBM flash layer which results in reduced ECD values (Fig. 2.6).

By averaging over the full spectral range, the channel structure yields average ECD reductions of 30% (p-polarization) and 22% (s-polarization) when compared to the planar device. Likewise, the 2-D periodic spectral ECD reduction is 11%. These improvements are promising, and full 2-D and 3-D solutions of the transport equa-

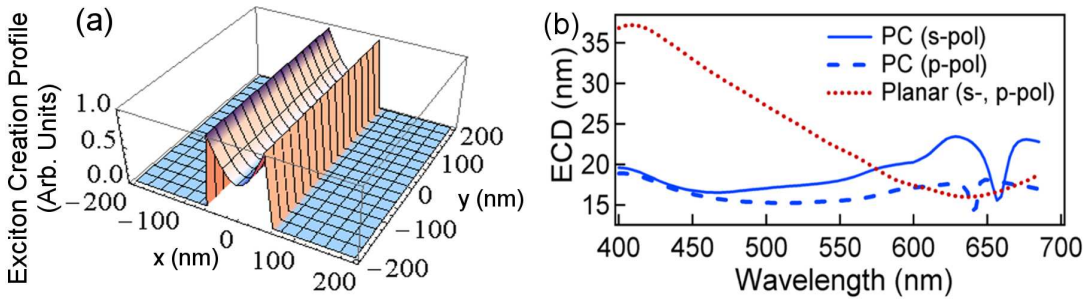


Figure 2.9: (a) Exciton creation profile of one unit cell for the 1-D periodic device at a depth of 150 nm with an incident p-polarized wavelength of 550 nm at normal incidence. (b) Spectral exciton creation distance (ECD) for the 1-D periodic device and planar control at normal incidence.

tions[65] should be conducted to determine how this geometry affects recombination and the exciton dissociation probability which also dictate the overall electronic performance. This will be discussed in full detail in Chapters 4 and 5.

## 2.7 Conclusion

In this chapter, simulation results are presented for a new class of organic BHJ solar cells, those that have a PC geometry. The physical dimensions and optical properties that maximize integrated absorption for P3HT:PCBM solar cells are provided. An optimal nanostructure thickness ($d_5$) is determined to be 200-300 nm, while a minimal index of refraction contrast of ∼0.3 is required between the two nanostructured materials where the LICM index must be lower than that of P3HT:PCBM. Secondly, the optical activity of excited quasiguided modes is characterized by identifying these modes in spectral absorption and photonic band diagrams. Both broad (short lifetime) and sharp (long lifetime) modes exist for the nanostructured devices. Exciton creation profiles for band edge quasiguided modes also indicate that these modes exhibit highly concentrated absorption in the P3HT:PCBM flash layer. As a final case study, it is demonstrated that a PC cell comprised of a photoactive layer of P3HT:PCBM bulk heterojunction blend and nc-ZnO can simultaneously enhance optical absorption and produce excitons closer to exit interfaces in P3HT:PCBM. Overall spectral absorption enhancements for the 1-D and 2-D periodic structures are 20% (one polarization) and 14%, respectively, with larger improvements observed near the band edge. These results will help guide the next chapter where PC solar cells are fabricated and tested.

# Chapter 3

# Realization of Photonic Crystal OPV

## 3.1 Introduction

As reviewed in Chapter 2, there have been extensive modeling efforts to enhance the absorption of light in the photoactive layer of organic solar cells[27,73–76]. Along with these modeling efforts, there has been tremendous progress in fabrication and measurement of light trapping devices and structures. In particular, schemes based on ray optics have provided enhancement in optical absorption, e.g. collector mirrors[92], microprism substrates[93], and V-folded configurations[94–96] but in these schemes absorption enhancement is not tailored to a desired spectral range. Methods based on wave optics have shown greater promise for light control where optical spacer designs[29,58] showcase the simplest technique in this class of methods. More complex diffraction grating[61,97,98] and surface plasmon[99] designs have also been investigated that offer the possibility to enhance absorption in a particular spectral range. Furthermore, the theoretical considerations of Chapter 2 for PC geometries suggest that absorption enhancements are anticipated for P3HT:PCBM solar cells with 100 nm active layers. In spite of this theoretical promise, there has been little progress in experimentally demonstrating PC effects in organic solar cells. While there has been success in nanopatterning the photoactive layer, the primary intention has been to provide an undulating surface for evaporating a metal diffraction grating[97,98,100] or to make an ordered BHJ device[63]. In the case of the ordered BHJ device, the currently accessible length scale of the PC (hundreds of nanometers) is not commensurate with the length scale for exciton migration to the donor/acceptor interface (tens of nanometers).

In this chapter, two-dimensional periodic PC organic solar cells made from highly ordered arrays of columnar features are presented. The PC is readily fabricated via Pattern Replication In Non-wetting Templates (P.R.I.N.T.)[101], a materials-agnostic process that lends itself to large area replication of nanoscale features. As

proofs of concept, two BHJ donors, poly(3-(2-methyl-2-hexylcarboxylate) thiophene-co-thiophene) (TDPTD) and P3HT, each paired with PCBM, are used to show that the fabrication method could be applied to any photoactive polymer processed from solution. For TDPTD:PCBM a 3-fold absorption enhancements is demonstrated near the band edge of this material system due to the PC geometry. Efficiency improvements of ∼70% result not only from improved absorption, but also from intriguing electrical improvements where both the FF and $V_{oc}$ are enhanced ∼10%. The PC structure is formed in a single P.R.I.N.T. step by nanopatterning the photoactive BHJ blend, a relatively high refractive index material, into a hexagonal array of posts with 400 nm periodicity. The BHJ then interfaces with a transparent, low refractive index form of nanocrystalline zinc oxide (nc-ZnO), which provides enough optical contrast to enable PC behavior. For P3HT:PCBM, the role of optical interference is presented and shown to be critical to optical absorption and lead to variations by as much as 90%. When absorption is maximized for both PC and planar cells a 13% enhancement is possible, which is similar to the theoretical investigations of Chapter 2. The success of PC and other light trapping techniques compared to planar solar cells are also reviewed.

Most of the results and figures of this chapter have been modified from the following publications:

[102]**J.R. Tumbleston**, D.-H. Ko, R. Lopez, and E.T. Samulski, *Characterizing enhanced performance of nanopatterned bulk heterojunction organic photovoltaics*, Proc. SPIE 7047, 70470S (2008).

[103]D.-H. Ko, **J.R. Tumbleston**, L. Zhang, S. Williams, J.M. DeSimone, R. Lopez, and E.T. Samulski, *Photonic crystal geometry for organic solar cells*, Nano Lett. 9, 2742 (2009).

[104]D.-H. Ko, **J.R. Tumbleston**, W. Schenck, R. Lopez, and E.T. Samulski, *Photonic crystal geometry for organic polymer:fullerene standard and inverted solar cells*, J. Phys. Chem. C 115, 4247 (2011).

## 3.2 Photonic Crystal OPV Fabrication

### 3.2.1 Making Nanopatterns Using P.R.I.N.T.

The Patterning (or Particles) Replication in Nonwetting Templates (P.R.I.N.T.) method[101] has been used to facilitate many applications in nanoscience including surface enhanced Raman spectroscopy[105], biomimicry of red blood cells[106], and fabrication of periodic gratings of various materials[107]. This technique has been proven to be effective in making structures on the order of microns[108] to smaller features on the order of tens of nanometers[109]. Seeing as the wavelength of visible light falls within this regime, P.R.I.N.T. serves as an exceptional technique to produce PC OPV devices.

Figure 3.1 shows nanopatterns of P3HT:PCBM with a variety of feature shapes including triangular, square,

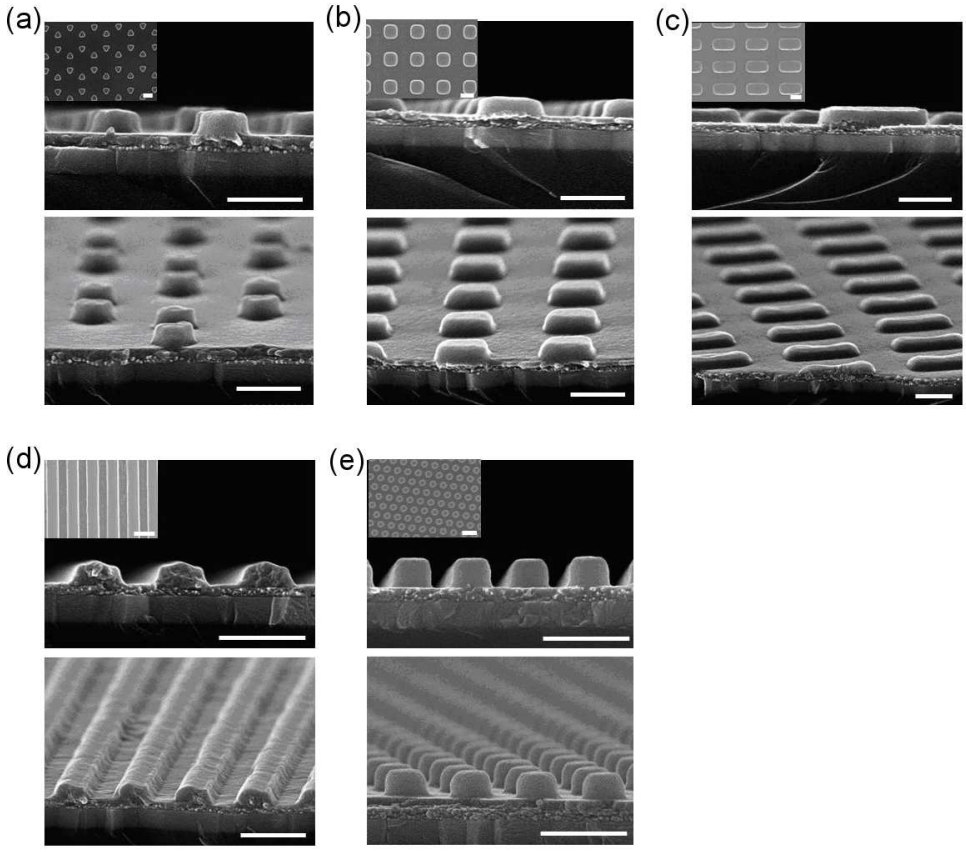


Figure 3.1: Scanning electron microscope (SEM) pictures for P3HT:PCBM replicas of PC nanopatterns using P.R.I.N.T. to fabricate features having a range of geometries: (a) hexagonal, (b) square, (c) rectangular, (d) linear grating, and (e) rows of columns. All patterns (a-e) are embossed into PEDOT:PSS on an ITO substrate (on glass). SEM pictures show respectively cross section views (top) and oblique views (bottom) with corresponding normal views (insets). All scale bars are 500 nm.

rectangular, grating and columnar. Due to the scalability of P.R.I.N.T., these patterns can be readily made over large areas (2.50 cm x 1.25 cm). Figure 3.2(a-e) demonstrates how these patterns are formed. A liquid 1 kDa PFPE-DMA ($\alpha$, $\omega$-functionalized dimethacrylate) precursor solution containing 1 wt% 2,2-diethoxyacetophenone (DEAP) is first poured over a nanopatterned silicon master template. The liquid precursor is then cross-linked using UV light for 3 min under a nitrogen purge. This provides an elastomeric mold of the master template after release from the nanostructured substrate. The mold is then placed on a spin-coated film of BHJ photoactive blend where pressure and heat are applied for typically 30 min. A torque of 1.69 Nm on the embossing set-up consistently yields a ~40 nm flash layer that connects the array of features and was determined to be the optimal thickness in Chapter 2.

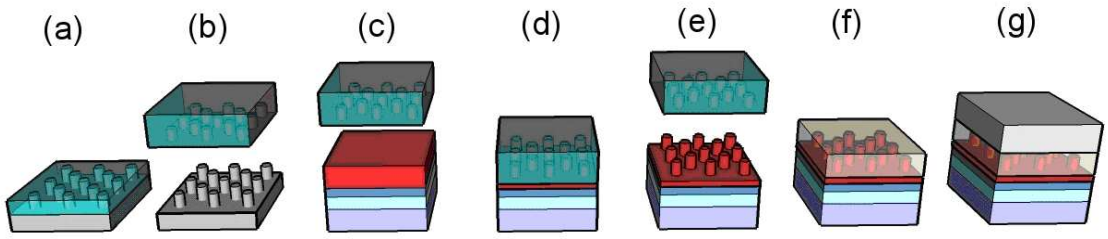


Figure 3.2: (a) A dimethacrylated-funtionalized PFPE is prepared and poured over a nanopatterned silicon master template. (b) The nanopatterned PFPE replica mold is generated by photochemically curing the PFPE. (c) A P3HT:PCBM solution is spincoated on an ITO/PEDOT:PSS-coated glass substrate (d) This layer is then patterned with the PFPE mold under pressure at 145 C for 30 min. (e) The PFPE replica is peeled off the substrate to give highly ordered and regular nanopatterns over the specified substrate area. (f)Next, nc-ZnO solution in methanol is spincoated on the nanopatterns, and (g) aluminum is thermally deposited as a cathode to complete the device.

### 3.2.2 Making a Complete Device

Figure 3.2 shows the complete process of device fabrication. The nanopatterning process described above is done on a glass substrate with ITO/PEDOT:PSS sequential layers. ITO-coated glass substrates are first sonicated with acetone, isopropyl alcohol, and distilled water for 10 min each, and then dried overnight in an oven (150 °C). The cleaned substrates are next treated with UV ozone for 20 min to make them more hydrophilic (UVO Cleaner 42, Jelight Company Inc.). Then, PEDOT:PSS (Baytron PH 500) is filtered with a 0.45 $\mu$m PVDF filter prior to spincoating on the ITO substrates with a target thickness of 40 nm. They are then dried for 10 min at 140 °C on a hotplate. The sample is next moved into an inert gas (purified nitrogen) glove box. Here, a solution of P3HT:PCBM is spincoated on the PEDOT:PSS prior to the P.R.I.N.T. procedure. For TDPTD:PCBM devices, the flash and nanopatterned layers are formed separately: a solution containing TDPTD (10 mg/mL) and PCBM (8 mg/mL) in chlorobenzene is filtered with a 0.45 $\mu$m PTFE filter and spincoated onto

the PEDOT:PSS-coated substrate to form a 40 nm flash layer and thermally cured (200 °C for 15 min). The thermal curing step deprotects the alternating poly(3-(2-methyl-2-hexylcarboxylate)thiophene-co-thiophene) to yield alternating poly(3-carboxylatethiophene-co-thiophene) making the film insoluble in chlorobenzene. Next, a more concentrated solution containing TDPTD (15 mg/mL) and PCBM (12 mg/mL) in chlorobenzene is spincoated on the cured flash layer. The new layer is patterned by the P.R.I.N.T. method. A planar cell is simultaneously fabricated by embossing the active layer with a flat PFPE mold. The patterning step is followed by spincoating various concentrations of nc-ZnO in methanol to obtain a desired thickness of nc-ZnO film. Finally the device is transferred into a vacuum chamber (2 x $10^{-6}$ mbar) and 110 nm of Al is deposited on defined cell areas (12 $mm^2$).

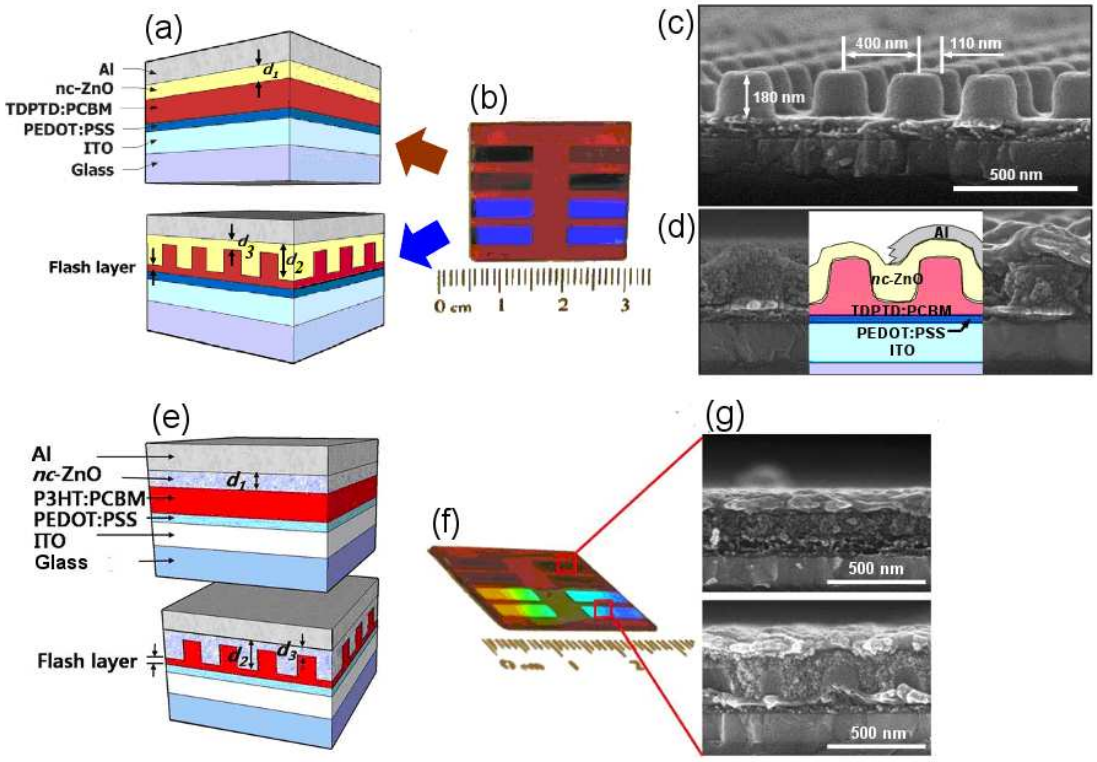


Figure 3.3: PC and planar solar cells using (a-d) TDPTD:PCBM and (e-g) P3HT:PCBM as the photoactive material. (a,e) Schematic of planar control (top) and PC (bottom) cells. (b,f) Photograph of planar cells (top) and iridescent PC cells (bottom) on the same device substrate. (c) SEM of hexagonal array of TDPTD:PCBM columns prior to back-filling with nc-ZnO. (d) SEM of PC cell showing the hierarchical arrangement of components (left without Al overcoat), right (from the top): Al/nc-ZnO/patterned and flash TDPTD:PCBM/PEDOT:PSS/ITO/glass substrate. (g) SEM showing the cross sections of planar (top) and PC cells (bottom) with P3HT:PCBM as the photoactive material.

Figure 3.3 shows a schematic, photograph, and SEM cross section of PC and planar control solar cells with TDPTD:PCBM as the photoactive material, while Fig. 3.3(e-g) shows similar images with P3HT:PCBM. In both cases, PC and planar cells are fabricated on the same device substrate, where PC cells can be easily distinguished due to the bright iridescence from the nanopatterned layer. Simultaneously fabricating PC and planar cells on the

Table 3.1: Thicknesses of nc-ZnO for PC and planar cells fabricated on five different device substrates using both TDPTD:PCBM and P3HT:PCBM. Values of $d_2$ that are less that the nanopattern height of 180 nm result in a wavy aluminum electrode as shown in the lower panel of Fig. 3.3(g).

| Device Number | Planar ($d_1$) | PC ($d_2$) | PC ($d_3$) |
|---|---|---|---|
| 1 | 50 | 30 | 10 |
| 2 | 90 | 100 | 40 |
| 3 | 130 | 150 | 60 |
| 4 | 200 | 220 | 70 |
| 5 | 280 | 300 | 120 |

same substrate ensures that each contains an equivalent volume of photoactive material and undergoes identical fabrication steps and thermal history. For the PC cells, the photoactive material constitutes both the planar flash layer (40 nm) and the hexagonal array of columnar features that are 180 nm in height. Further discussion regarding the choice of these dimensions will be discussed below.

Included in this thesis are results for a range of nc-ZnO thicknesses in order to optimize cell absorption for both PC and planar cells. These are included in Table 3.1.

## 3.3 Electro-optical Performance

### 3.3.1 Optical Properties

As was shown in Chapter 2, there must be a significant refractive index contrast in order for the nanopatterned cells to exhibit enhanced optical performance. Figure 3.4 shows the refractive index contrast between both photoactive materials, TDPTD:PCBM and P3HT:PCBM, and nc-ZnO. When combined with the 400 nm hexagonal periodicity of the PC, optimal conditions are met for band edge absorption enhancements in these photoactive materials.

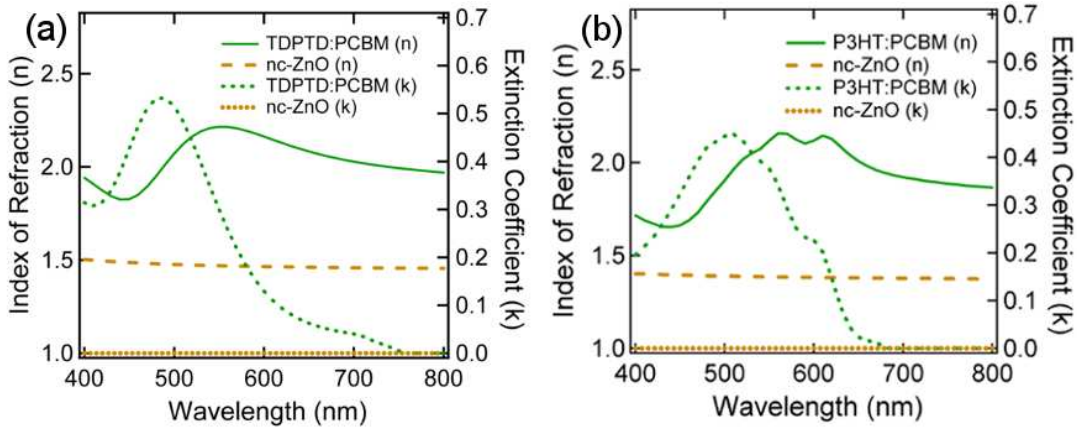


Figure 3.4: Index of refraction (n) and extinction coefficient (k) for TDPTD:PCBM, P3HT:PCBM, and nc-ZnO as measured via variable angle spectroscopic ellipsometry

Optical properties are measured using variable angle spectroscopic ellipsometry with a J.A. Woollam Co, Inc. V-VASE system. The complex refractive index of each material is measured individually on cleaned glass substrates. The optical properties of other cell materials are given in Fig. 3.5. For transparent materials, such as nc-ZnO and glass, a Cauchy model is used to obtain the index of refraction, while the general oscillator model with either Gaussians or Lorentz oscillators is used for absorbing materials. It is important to note that ITO, PEDOT:PSS, and Al have nonzero extinction coefficients and thus contribute to parasitic absorption losses. Only Al was considered to be optically lossy in Chapter 2 due to the low extinction coefficients of ITO and PEDOT:PSS. In this chapter, the loss for all three materials is considered. The extinction coefficient of glass is not shown because it is zero in this wavelength range. All materials are assumed to be isotropic, and there is close agreement with literature values[31]. It should be noted that anisotropy has been detected in device materials like PEDOT:PSS[32] and P3HT:PCBM[110], but under normal incidence, the electromagnetic fields only interact with measured in-plane optical properties.

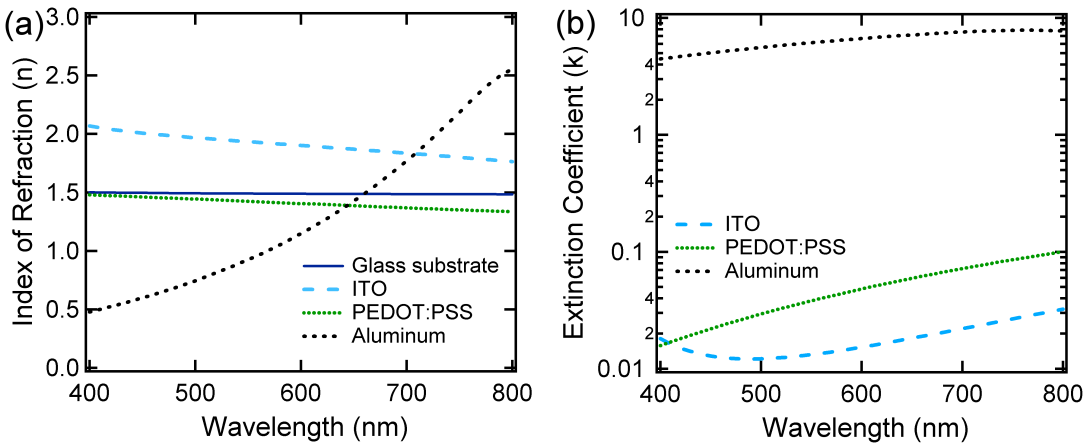


Figure 3.5: (a) Index of refraction (n) and (b) extinction coefficient (k) for glass substrate, ITO, PEDOT:PSS, and Al. The extinction coefficient of the glass substrate is zero in this wavelength range.

### 3.3.2 Enhanced Absorption and IPCE for TDPTD:PCBM Devices

Figure 3.6 shows the s-polarized zeroth order reflection measured at normal incidence for the PC and planar cells with TDPTD:PCBM as the photoactive material. P-polarization is nearly identical at normal incidence and is not shown. Due to negligible transmission and scattering, (the iridescence effects are only appreciable at large incidence angles), the reflection ($R$) is an approximation to the absorption ($A$) given by $A = 100 - R$. Due to the 90 nm active layer thickness of the planar cell, there is strong absorption in the visible range where the extinction coefficient of TDPTD:PCBM is high. This corresponds to essentially equivalent absorption in this wavelength

range for PC and planar cells. However, for wavelengths longer than 600 nm, there is much stronger absorption in the PC cell as evidenced by the reduced reflection. For example, for device No. 2, the absorption is enhanced 3.5 times for the PC cell over the planar one for $\lambda = 660$ nm. However, the broad drop in reflection observed for the PC cell for device No. 1 near $\lambda = 800$ nm is credited to absorption in the Al electrode that partially fills the area between the TDPTD:PCBM posts during evaporation due to a thin nc-ZnO layer. This broad feature has been reproduced in simulations and does not occur for the other devices where thicker nc-ZnO layers are used that prevent significant filling of Al between the TDPTD:PCBM posts.

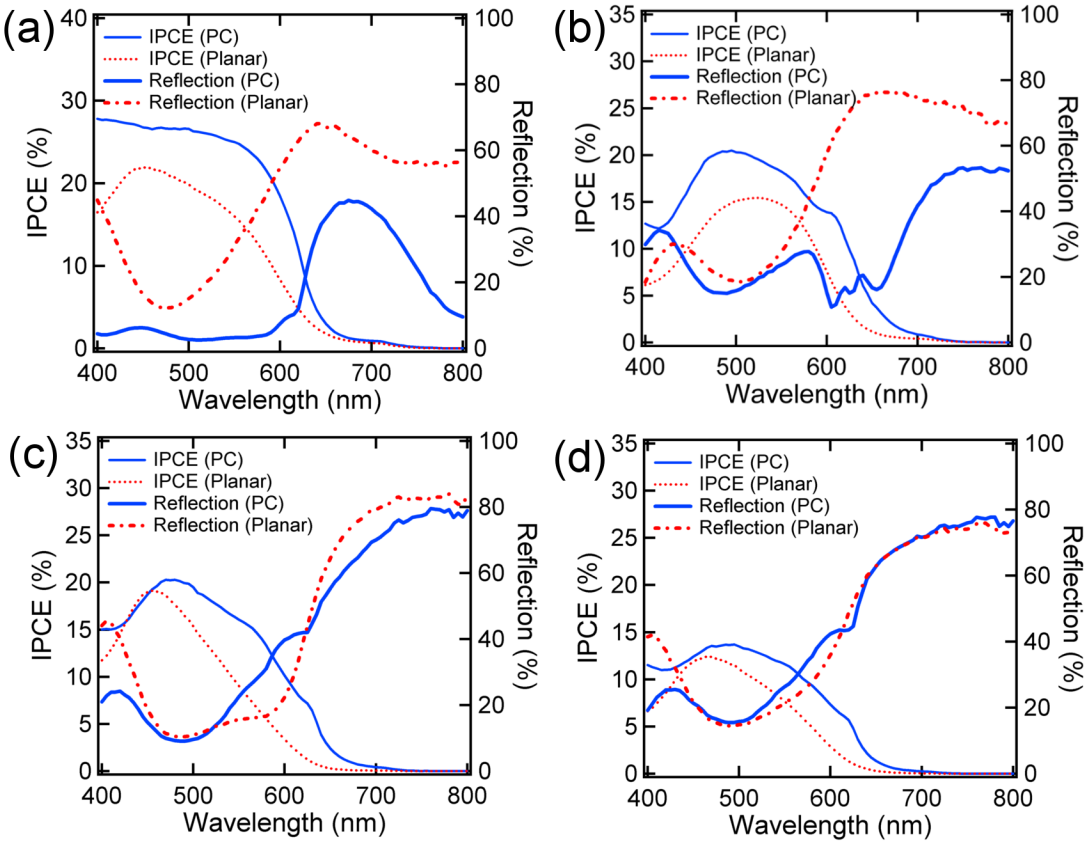


Figure 3.6: Normal incident device reflection and incident photon to current conversion efficiency (IPCE) for TDPTD:PCBM device (a) No. 1, (b) No. 2, (c) No 4, and (d) No. 5.

Also shown in Fig. 3.6 is the incident photon to current efficiency (IPCE) for the PC and planar cells. IPCE is measured in conjunction with device reflection in air using a 75W HS-190 monochromater by J.A. Woollam Co., Inc and an optical chopper with lock-in amplifier. This is a custom set-up made for this thesis where the measurement accuracy is described in the Appendix. Data are taken in both p- and s-polarizations with p-polarization oriented along the 400 nm periodicity of the hexagonal photonic crystal (s-polarization rotated 90°). No device degradation occurs over the maximum measurement time of 3 hrs. Interestingly, there is an enhancement in IPCE for wavelengths where the PC cell is absorbing more strongly, but there is also an

enhancement where they appear to have similar absorption in the visible range. A first step towards reconciling this effect is with a more precise determination of the absorption. The above mentioned approximation of A = 100 - R is a measure of the total absorption where losses in all internal layers are included. Even though PC and planar cells are fabricated on the same substrate and have equivalent volumes of all internal materials, the PC structure alters the optical profile in each internal layer due to its modulated thickness relative to the planar photoactive layer. This will cause changes in the optical field in layers that also absorb light but do not produce photocurrent, such as ITO and PEDOT:PSS. Thus, simply comparing the measured reflection only offers a first approximation to the photoactive absorption.

### 3.3.3 IQE Enhancement for TDPTD:PCBM Devices

The redistribution of optical losses may be individually quantified by fitting a solution to Maxwell's equations to the measured reflection data. Once this is achieved, absorption in each layer is determined by calculating the change in the Poynting vector from interface to interface as is frequently done for planar devices[58,111]. Using the scattering matrix optical model described in Chapter 2 along with the optical properties of the cell materials from Figs. 3.4 and 3.5, the physical dimensions of the device are varied over a range close to measured SEM values until an appropriate fit with the experimental data is obtained.

An important point to note is that optical coherence is lost in the relatively thick (1 mm) glass substrate, so it cannot be included directly in the simulation method. Reflection from the thin film stack where light is incident from a semi-infinite glass substrate is first calculated via the simulation method. The actual reflection that is compared to measurement is then calculated from an equation that is a function of the thin film stack reflection and the reflection coefficient from an air/glass interface. This procedure and subsequent equations are frequently used for optically modeling planar organic photovoltaic cells and is described elsewhere[26].

These results are given in Fig. 3.7 for the PC and planar cells for device No. 3. Good agreement is obtained between the theory and experiment for both polarizations at normal incidence. The model is then used to calculate absorption in the TDPTD:PCBM blend that will yield photocurrent in the external circuit. Blend absorption is plotted for both PC and planar cells for device No. 3 for s-polarization. This is a different device with different nc-ZnO thicknesses from those presented in Fig. 3.6, but the tendency of enhanced absorption and IPCE is qualitatively identical. There is still essentially equivalent photoactive absorption in the visible range with an enhancement towards the band edge. Specifically, a 4.8-fold absorption enhancement is achieved at $\lambda$ = 630 nm for the PC cell relative to the planar one. This contributes to an average tripling of absorption near the

band edge ($580 \leq \lambda \leq 750$ nm).

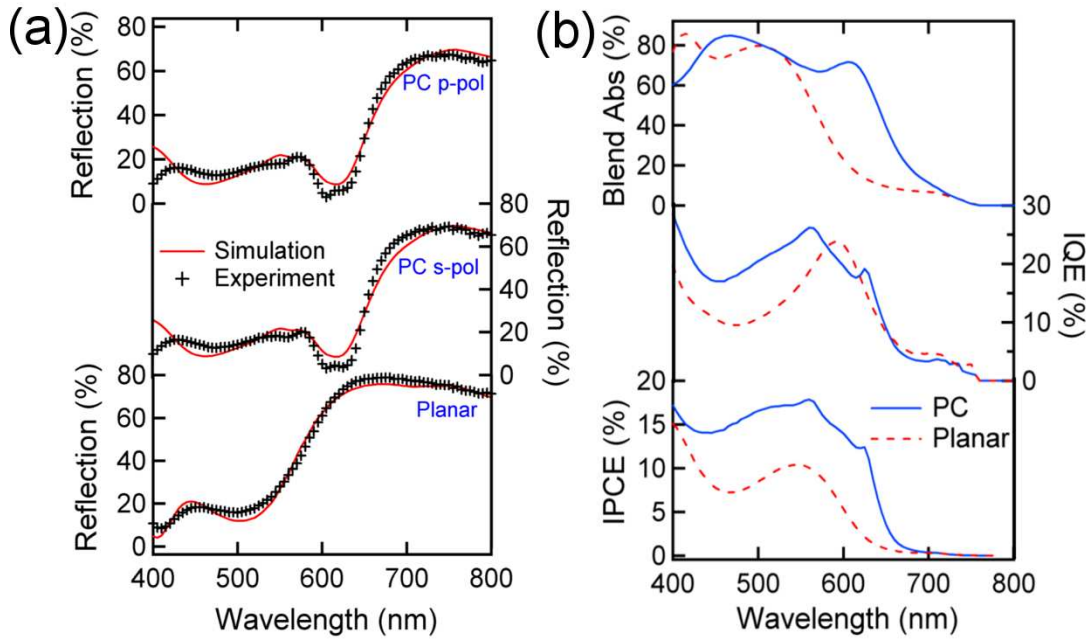


Figure 3.7: (a) Experimental and simulated zeroth order reflection for PC and planar cells for TDPTD:PCBM device No. 3 at normal incidence in both p- and s-polarization. The planar cell is equivalent in both polarizations. (b) Calculated TDPTD:PCBM absorption, IQE, and IPCE under s-polarized illumination.

Applying the simulation method to the devices did yield an accurate measure of photoactive absorption, but it did not explain the enhanced IPCE in the visible range where absorption is essentially equivalent between PC and planar cells. By calculating absorption in TDPTD:PCBM ($A_{BHJ}$) and measuring IPCE, the internal quantum efficiency (IQE) can be calculated by,

$$IPCE(\lambda) = IQE(\lambda)A_{BHJ}(\lambda). \tag{3.1}$$

The IQE is a measure of the electrical processes in the cells at short circuit and is given for PC and planar device No. 3 in Fig. 3.7(b). Electrical processes include exciton dissociation at the BHJ donor/acceptor interface, drift and diffusion of free charge carriers through the blend, and carrier collection at the electrodes. As shown in Fig. 3.7, the IQE is enhanced in the visible spectral range, which indicates an electrical enhancement for the PC cell. The root cause of this enhancement will be discussed in Chapter 4.

### 3.3.4 Observation of Resonant Modes

Up to now, PC performance enhancements have been described under normal light incidence. For non-normal illumination, resonant mode splitting occurs and generates absorption enhancements that exhibit a rich

photonic behavior. This is demonstrated in Fig. 3.8 for PC cells for TDPTD:PCBM device No. 3 where the differences between p- and s-polarization can now be resolved in both reflection and IPCE measurements from 12° to 40°. Under normal incidence, resonant mode degeneracy masks the actual number of modes excited in the PC geometry as indicated in the reflection data of Fig. 3.6 and 3.7. On the other hand, under non-normal conditions, three modes can be resolved in p-polarization with at least two modes in s-polarization near the band edge of TDPTD:PCBM. Enhancements in both polarizations are possible, because the PC geometry is periodic in both lateral dimensions. Arrows track the dispersion of the stronger modes along with the resulting IPCE enhancement. The spectral location of the band edge of TDPTD:PCBM is also apparent near $\lambda = 750$ nm, because the resonant modes as shown in reflection retain their shape even after they have red-shifted past the wavelength where TDPTD:PCBM becomes transparent and produces no photocurrent. These long wavelength excitations are possible because other strata in the cell such as PEDOT:PSS and ITO have non-zero extinction coefficients and absorb in the near-IR. Optical simulations confirm that ITO and PEDOT:PSS absorb a significant fraction of resonant mode energy for these incident angles even at wavelengths where photocurrent is produced. This limits the observed photocurrent enhancement.

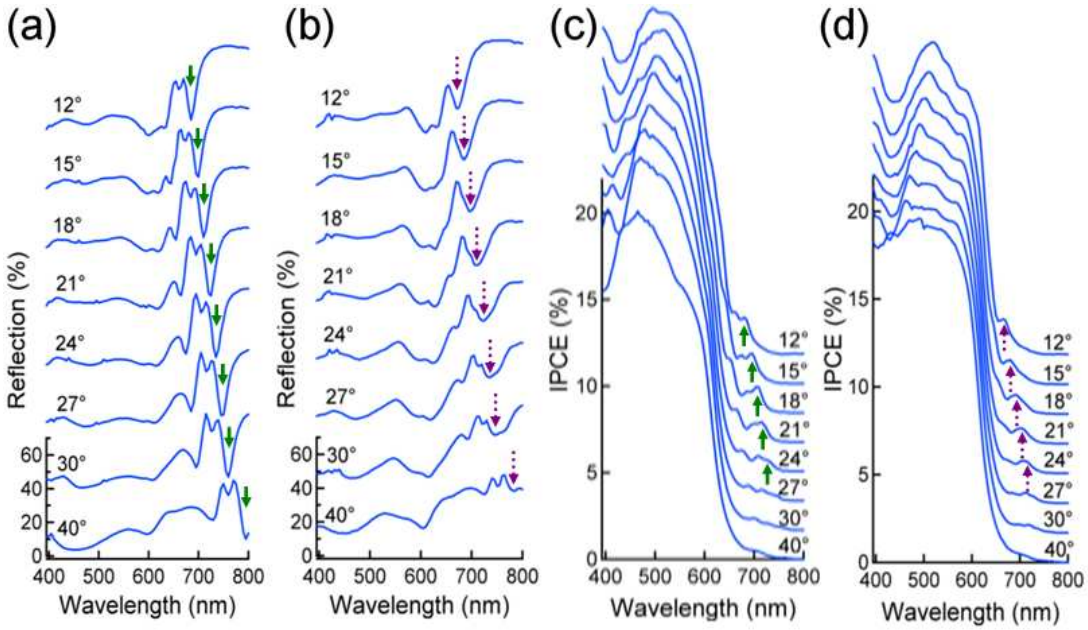


Figure 3.8: Angular dependent zeroth-order reflection and IPCE for PC cells for device No. 3; (a) p-polarized reflection, (b) s-polarized reflection, (c) p-polarized IPCE, and (d) s-polarized IPCE. The arrows denote sharp drops in reflection and corresponding increases in IPCE associated with resonant mode excitation.

This can be quantified with a complete picture of optical redistribution, including absorption in each layer along with zeroth order reflection and non-zero diffractive order scattering. This is given in Fig. 3.9 for device No. 3. The limited IPCE spikes associated with resonant modes under non-normal illumination is explained by

the interception of a significant fraction of optical energy by ITO and PEDOT:PSS as can be seen in Fig. 3.9(b) for the resonant mode centered at $\lambda = 685$ nm.

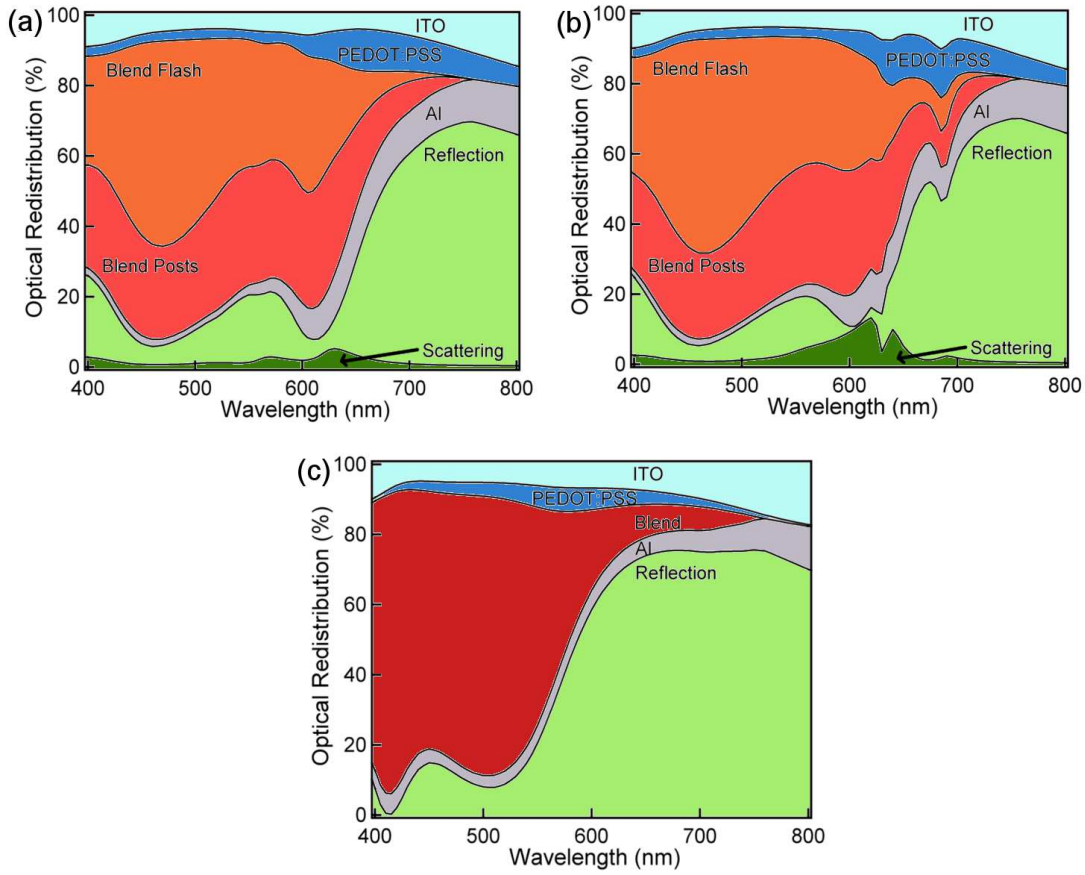


Figure 3.9: Optical redistribution for s-polarization at normal incidence for TDPTD:PCBM device No. 3. PC cell at (a) normal incidence and (b) 15°. (c) Planar device at normal incidence.

### 3.3.5 Efficiency Enhancement for TDPTD:PCBM PC Cells

In order to further investigate the electrical properties, device performance was evaluated in an inert atmosphere (purified nitrogen) under standard AM 1.5 testing conditions. The mean values of the $J_{sc}$, $V_{oc}$, FF, and efficiency are summarized in Fig. 3.10 where comparisons are made between PC and planar cells fabricated on the same substrate according to Table 3.1. An average enhancement of 10% is observed for $V_{oc}$ and 9% for FF for the PC cells. On the other hand, the $J_{sc}$ shows more variable enhancements due to changes in optical absorption that result from optical interference. Overall, there is an average 68% efficiency enhancement for PC cells. The improvement of the IQE, $V_{oc}$, and FF for PC cells will be addressed in Chapter 4. It is possible that the PC generates a more favorable carrier creation profile in the device that results in shorter transport paths for electrons and holes out of the BHJ blend (from Chapter 2). This may be facilitated by a 45% larger interface between

TDPTD:PCBM and nc-ZnO for the PC cells. The PC structure may also alter the static internal electric field in the photoactive region that could change the field-dependent dissociation of excitons at the TDPTD donor and PCBM acceptor interfaces.

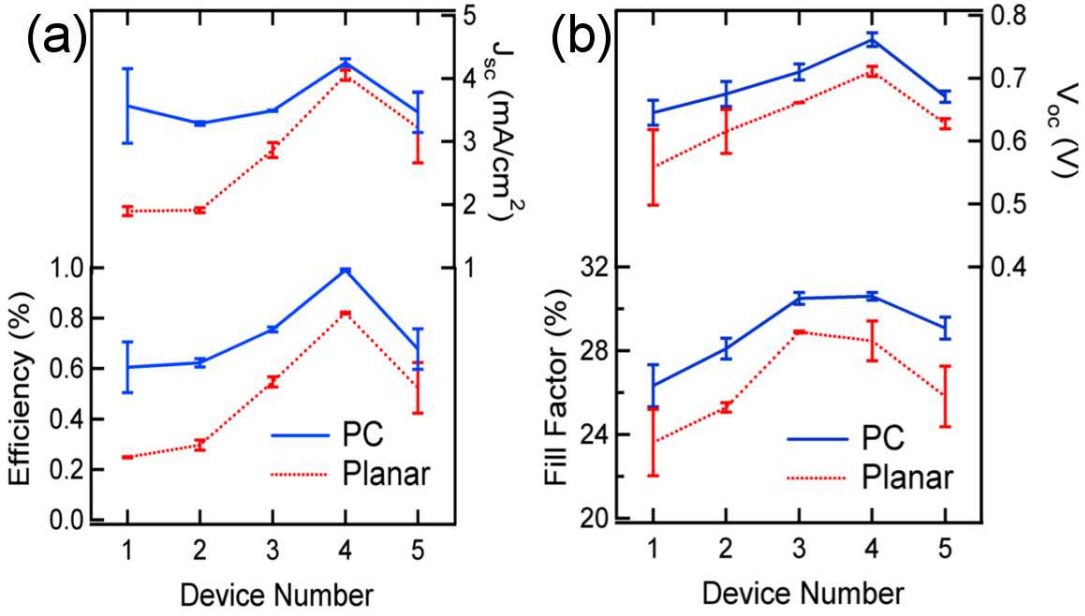


Figure 3.10: (a) Short circuit current ($J_{sc}$) and efficiency for PC and planar cells where comparisons are made between cells fabricated on the same device substrate. (b) The corresponding values of open circuit voltage ($V_{oc}$) and fill factor (FF).

### 3.3.6 Resonant Modes and Efficiency of P3HT:PCBM PC Cells

Like TDPTD:PCBM solar cells, resonant modes are detected for PC cells with P3HT:PCBM as the photoactive material. Figure 3.11 shows device reflection for s-polarized light under 15° incidence. The loss of reflection at certain wavelengths is even apparent to the naked eye when comparing planar and PC cells fabricated on the same substrate (insets of Fig. 3.11(a)). Furthermore, the presence of resonant modes is clear in Fig. 3.11(b) by the blue- and red-shifts as the incident angle changes from 12° to 30°. Even though the reduction in reflection is significant, P3HT:PCBM becomes transparent around $\lambda = 650$ nm. Thus, any additional absorption due to resonant mode excitation can only occur if they exist for wavelengths lower than the band-edge. Seeing as both ITO and PEDOT:PSS are used in these devices, it is probable that a portion of resonant mode excitations are absorbed in these materials.

In terms of optical redistribution at normal incidence, for the PC cell (Fig. 3.12(a)), absorption in P3HT:PCBM is approximately equal between the thin 40 nm flash layer (42%) and 180 nm tall columns (58%), while Al and ITO also contribute to absorption above 650 nm where P3HT:PCBM is transparent. Absorption in the pho-

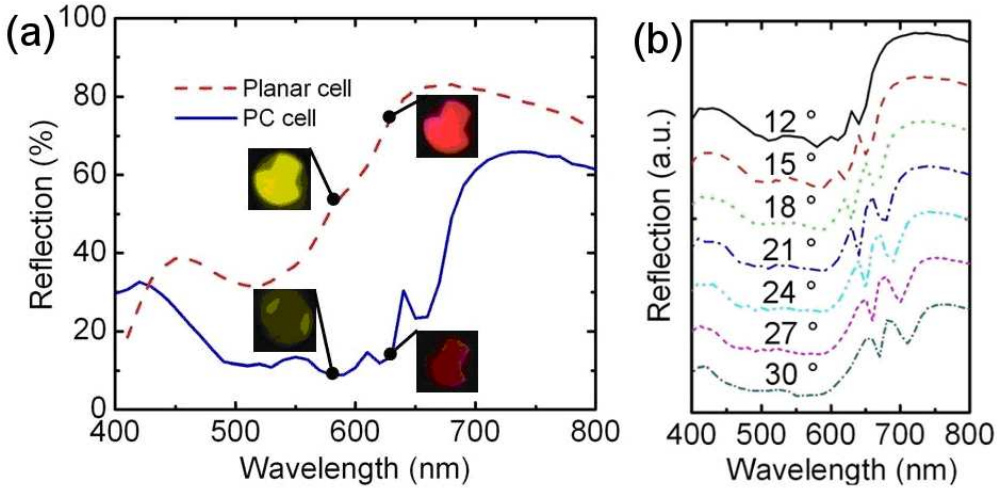


Figure 3.11: (a) Zeroth order reflection for PC and planar cells for s-polarized light at 15° incidence for PC and planar cells with P3HT:PCBM as the photoactive material. The insets show camera image differences between PC and planar cells, a coarse indicator of the differences in reflection. (b) Angular dependent reflection, which shows the excitation of resonant modes in the device structure.

toactive layer is the only optical loss that leads to the creation of excitons; this is quantified by calculating the total exciton generation rate. The latter is obtained by multiplying the fraction of absorption in P3HT:PCBM from the optical redistribution by the AM 1.5 solar spectrum[88] and integrating over the wavelengths where P3HT:PCBM is absorptive. This is then multiplied by the thickness of the photoactive layer, or in the case of PC cells, a P3HT:PCBM film thickness with an equivalent volume of the flash and nanopatterned layers. This calculation indicates that P3HT:PCBM absorption in the PC cell is about 50% higher relative to the planar cell (PC cell: 6.38 x $10^{20}$ $s^{-1}m^{-2}$, planar cell: 4.15 x $10^{20}$ $s^{-1}m^{-2}$). A similar difference is noted in the current-voltage measurement. Under 85 mW/cm$^2$ illumination, the $J_{sc}$ for PC cells (8.93 mA/cm$^2$) is 40% higher than the planar cell (6.36 mA/cm$^2$), as shown in Figure 3.12(b). It should be noted that the observed efficiency for the PC cell is 2.91% with $V_{oc}$ = of 0.61 V and FF = 46%.

Even though the PC cells have higher absorption and $J_{sc}$ relative to the planar cell fabricated on the same substrate, optical interference plays a major role in determining the absorption and the resulting $J_{sc}$ for both PC and planar cells. For instance, the thickness of the transparent, PC backfill material, nc-ZnO, affects absorption making it important to explore a range of backfill thicknesses to ascertain the maximum absorption. Figure 3.12(d) shows the total exciton generation rate calculated with the optical model as a function of nc-ZnO flash thickness ($d_3$) and film thickness ($d_1$) for PC and planar cells, respectively. For the PC cell, the nc-ZnO thickness between the columns ($d_2$) is fixed to the column height of 180 nm. The experimental data points (symbols in Fig. 3.12(d)) mark fabricated devices where simulated reflection spectra have been fitted to the measured reflection

by varying physical dimensions. Using the best fit optical model, the total exciton generation rate is determined. The calculations (curved lines) are performed using an ITO thickness of 150 nm and PEDOT:PSS thickness of 42 nm, which are derived from the average layer thicknesses for all devices. Absorption for both PC and planar cells oscillates with nc-ZnO thickness where a 90% variation from maximum to minimum is noted for planar cells. This is a critical point and supports the methodology of making devices with a range of nc-ZnO thicknesses, because simply making one device could lead to simultaneous fabrication of maximum absorbing PC cells and minimum absorbing planar cells (or vise versa) on the same device substrate. This is the case for the device presented in Fig. 3.12(a-c). However, comparing the peak values of the total exciton generation rate for each cell type suggests there is a 13% absorption enhancement for PC cells. This is consistent with the models of Chapter 2.

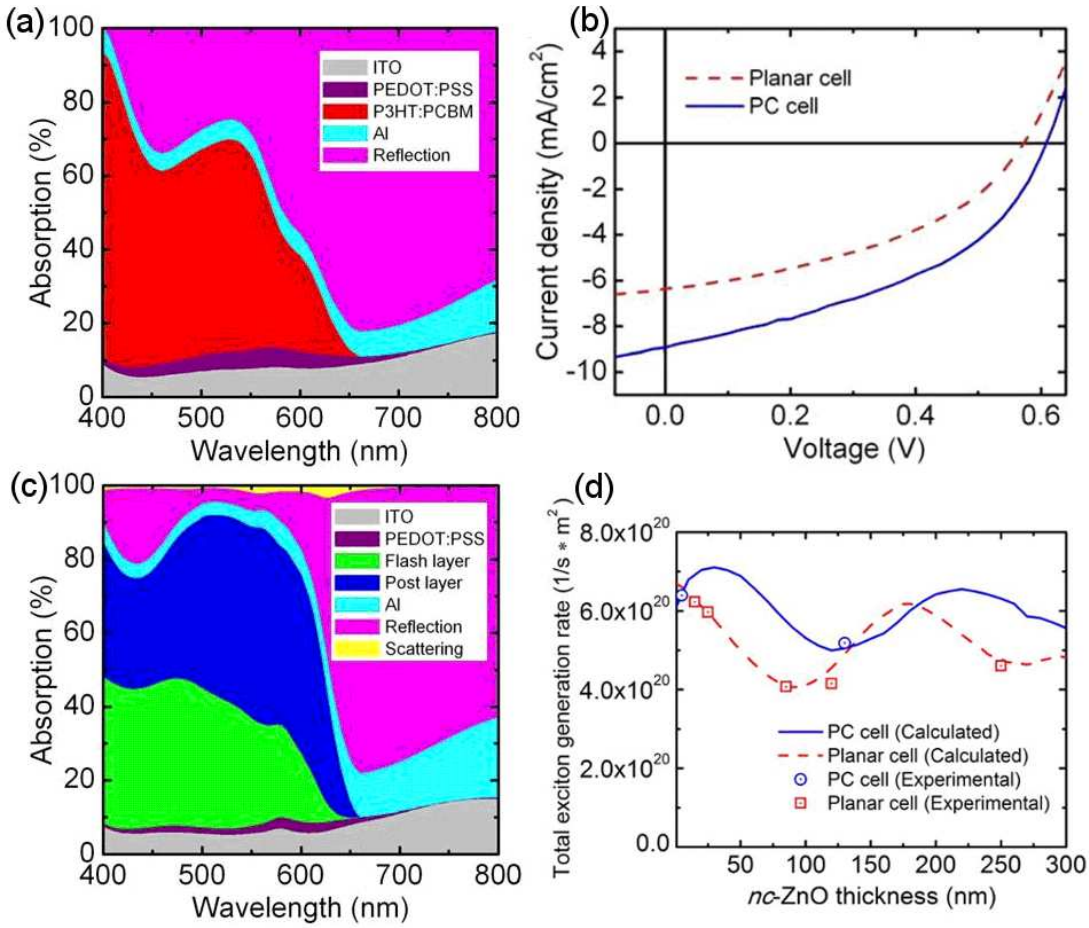


Figure 3.12: Optical redistributions at normal incidence for (a) planar and (c) PC cells under normal incidence with P3HT:PCBM as the photoactive material. (b) Current density vs. voltage (J-V) behavior for PC and planar cells where the PC cell shows higher absorption compared to the planar cell, which follows the prediction by the optical model. (d) Total exciton generation rate as a function of nc-ZnO overlayer thickness ($d_3$) and planar film thickness ($d_1$) for PC and planar cells, respectively. Symbols correspond to fabricated devices that lie along the calculated curve for all nc-ZnO thicknesses between 0 and 300 nm.

### 3.3.7 Patterning Lessens Impact of Optical Interference

Figure 3.13 shows the total exciton generation rate of PC cells for various flash layer thicknesses. The volume of P3HT:PCBM is conserved for each case meaning that PC cells with thick flash layers have correspondingly short nanopattern columnar features. While there is only slight variation in the maximum for each case, there is a significant reduction in the amplitude of oscillation of the total exciton generation rate with varying nc-ZnO thickness. This is an important point, because for the thinnest flash layer (10 nm), which has the tallest nanopatterned columns, there is the smallest oscillation with nc-ZnO thickness. This occurs, because this cell has the largest total thickness, where the optical field remains concentrated in P3HT:PCBM as the nc-ZnO thickness is varied. The opposite is true for the planar cell that has the thinnest total thickness (90 nm) and correspondingly largest oscillation in total exciton generation rate. The characteristic that the PC cell is able to stifle variations in absorption due to optical interference is a positive trait to this type of device architecture.

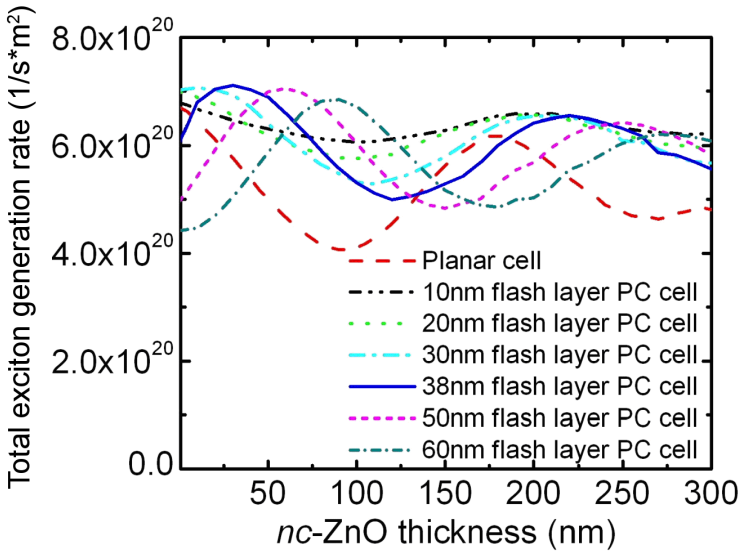


Figure 3.13: Total exciton generation rates for variable flash layer thickness for PC cells. The cell with the thinnest flash layer (i.e. thickest nanostructure layer) suffers the least from absorption fluctuations, while the cell with the thickest flash layer (the planar control cell) has the greatest variation.

## 3.4 Patterning Efficiency: The Bottom Line

Thus far, absorption enhancements have been shown for PC cells relative to fabricated planar control cells. In this section, the broader impact of patterning will be addressed in relation to literature device performance. First, all comparable flat cells are contacted with a flat PFPE mold in order to ensure that flat and patterned cells undergo the same processing conditions. When compared to planar cells that are not contacted with PFPE,

Table 3.2: Comparison of performance parameters for PC and literature planar cells. The first set of P3HT:PCBM devices with nc-ZnO are under 85 mW/cm$^2$ illumination. Other notable light trapping and planar devices with P3HT:PCBM as the active layer are shown at the bottom of the table.

| Cell Configuration | $J_{sc}$ (mA/cm$^2$) | $V_{oc}$ (V) | FF (%) | PCE (%) |
|---|---|---|---|---|
| PC P3HT:PCBM pattern w/ nc-ZnO | 8.93 | 0.61 | 46 | 2.91 |
| Lit [29]: Planar P3HT:PCBM w/ $TiO_x$ | 11.1 | 0.61 | 66 | 5.0 |
| PC TDPTD:PCBM pattern w/ nc-ZnO | 4.25 | 0.76 | 29 | 0.99 |
| Lit [63]: Bilayer TDPTD:PCBM pattern | 1.19 | 0.78 | 48 | 0.80 |
| PC P3HT:PCBM pattern w/ nc-ZnO and CuPc | 6.22 | 0.52 | 45 | 1.44 |
| Lit [112]: Planar P3HT:PCBM w/ CuPc only | 12.54 | 0.64 | 51 | 4.13 |
| PC MDMO-PPV:PCBM pattern w/ nc-ZnO | 1.6 | 0.83 | 43 | 0.57 |
| Lit [113]: Planar MDMO-PPV:PCBM | 5.25 | 0.82 | 61 | 2.5 |
| PC $TiO_2$ pattern w/ P3HT:PCBM and $WO_3$ | 2.85 | 0.51 | 25 | 0.36 |
| Lit [114]: Planar P3HT:PCBM w/ $TiO_2$ and $WO_3$ | 7.20 | 0.60 | 60 | 2.58 |
| Lit [97]: Grating P3HT:PCBM using PDMS stamp | 10.9 | 0.62 | 64 | 4.3 |
| Lit [115]: Grating ITO filled with P3HT:PCBM | 10.5 | 0.52 | 60 | 3.4 |
| Lit [7]: Planar P3HT:PCBM | 10.6 | 0.61 | 67 | 4.4 |

planar cells that are contacted have reduced performance. This was a general trend observed over the course of this thesis and varied depending on the preparation conditions of PFPE and device materials. This was least critical for TDPTD:PCBM devices. The reduction mainly occurred in the FF and could be due to contamination, morphology changes while under contact, or induced nonuniformity while under pressure.

Solving this problem was attempted by patterning an oxide, such as $TiO_2$, that could be thoroughly cleaned prior to spincoating a BHJ blend on top of the nanopattern. Even so, poor overall device performance still remained due to the thick $TiO_2$ layer used for the nanopattern that resulted in very high serial resistance (see Table 3.2).

Representatives of the highest performing PC cells with various device configurations fabricated during this thesis are given in Table 3.2. Both device types discussed in detail above (P3HT:PCBM and TDPTD:PCBM interfaced with nc-ZnO) are shown with the nc-ZnO thickness that gives the best performance (averaged over 4 PC cells). Other device configurations are also given that include different active and patterned materials. When compared to planar device configurations in the literature that have similar device materials, only TDTPD:PCBM has improved performance. In many ways it is not appropriate to compare PC cells with planar cells from other groups, due to variations in measurement conditions, polymer polydispersity, preparation conditions (including PFPE contact), and materials supplier. However, at the end of the day, the efficiency alone is critical and will drive future research. Most notably, the highest performing P3HT:PCBM PC cells in this thesis have PCE ~3%. This is also the case for devices with gratings of P3HT:PCBM made by stamping with PDMS [97] and gratings of ITO filled with P3HT:PCBM [115] explored by other groups. In both cases, the device efficiency is on par

or worse than planar P3HT:PCBM devices that underwent solvent annealing and demonstrated PCE = 4.4% back in 2005 [7]. During the course of this thesis, other device configurations not listed in Table 3.2 were also made including patterned PEDOT:PSS (surfactant added that gave highly ordered patterns but also reduced $V_{oc}$) and patterned P3HT:PCBM filled with thick layers of $WO_3$. Even in these cases PCE > 3% was not achieved. However, relative to planar cells with PFPE contact, enhanced absorption was commonly noted along with the excitation of resonant modes. In all cases, excellent, highly ordered nanopatterns of either active material or sol-gel oxide were observed in SEM. In some cases enhancements in PCE followed. In the conclusion of these thesis, future directions for light trapping and nanostructures will be addressed based on these results.

## 3.5 Conclusion

In summary, this chapter has reviewed the fabrication of BHJ organic solar cells with PC geometries. This has been achieved using the materials-agnostic P.R.I.N.T. process where ordered arrays of submicron features can be made in a single step. The PC structure boosts optical absorption relative to planar cells with PFPE contact. Furthermore, it provides a method to target specifically desired regions of the solar spectrum for absorption enhancements via a photonic structure that exhibits multiple resonances. This is demonstrated for two active materials, TDPTD:PCBM and P3HT:PCBM. Most importantly, the optical model used in Chapter 2 to predict absorption enhancements is confirmed in this Chapter and serves as a valuable tool for the design of future light trapping structures.

# Chapter 4

# Space Charge and Parasitic Resistances

## 4.1 Introduction

In Chapters 2 and 3 of this thesis, optical simulations, fabrication, and measurements are described for a new type of organic solar cell architecture that involves a PC geometry. For these cells it is possible to enhance the absorption of light without increasing the active layer thickness and thereby circumvent the thickness tradeoff described in Chapter 1.

Up to now, the focus of this thesis has been on optical performance. However, for the active material TDPTD:PCBM, enhanced IQE, FF, and $V_{oc}$ were observed for PC cells. Optical performance alone is not adequate to explain these results, so a more thorough description of the electrical properties of BHJ solar cells is required.

The underlying intricacy of device operation as described in Chapter 1 has lead to the use of multiple models to predict the current density vs. voltage (J-V) behavior under different operation conditions. For example, drift/diffusion formalisms have been proposed[65] and used extensively[19,55,59] to describe charge transfer (CT) state dissociation and free carrier transport, two of the electrical processes outlined in Chapter 1. On the other hand, the equivalent circuit model[116], is commonly applied in part due to its relative ease of implementation[53,67,117].

In this chapter, the drift/diffusion model is introduced and applied to device operation of PC cells. When combined with the optical model, a complete electro-optical description of BHJ solar cells is achieved. A 1-D periodic PC cell with MDMO-PPV:PCBM as the active material is modeled as a case study. Even though absorption enhancements are predicted, the final $J_{sc}$ is lower for the PC cell when compared to a comparable planar cell. This is due to bimolecular recombination in the nanopatterned posts due to the weak electric field.

Given this result, the effect of the boundary conditions on predicted device performance are thoroughly explored. Ultimately, it is found that the PC geometry is not predicted to enhance efficiency due to space-charge build-up.

As predicted from the electro-optical model, space-charge build-up leading to high levels of bimolecular recombination can be tested by measuring the light intensity dependence of the photocurrent as described in Chapter 1. In the process of conducting these experiments, it is found that high levels of series resistance ($R_{sr}$) can affect light intensity measurements in the same way as significant bimolecular recombination. This leads to a complete study of parasitic resistances, both series ($R_{sr}$) and shunt ($R_{sh}$), and how these resistances influence light intensity measurements. This is done for two donor materials, P3HT and MDMO-PPV, both combined with PCBM, where results are compared with the equivalent circuit model. Finally, the chapter is ended with an example system where $R_{sr}$ is dominate, inverted BHJ devices with $TiO_x$ as an electron transport layer.

Most of the results and figures of this chapter have been modified from the following publications:

[33]D.-H. Ko, **J.R. Tumbleston**, M.-R. Ok, H. Chun, R. Lopez, and E.T. Samulski, *Suppression of bimolecular recombination by UV-sensitive electron transport layers in organic solar cells*, J. Appl. Phys. 108, 083101 (2010).

[118]**J.R. Tumbleston**, D.-H. Ko, E.T. Samulski, and R. Lopez, *Nonideal parasitic resistance effects in bulk heterojunction organic solar cells*, J. Appl. Phys. 108, 084514 (2010).

[119]**J.R. Tumbleston**, D.-H. Ko, R. Lopez, and E.T. Samulski, *Electro-optical model of photonic crystal bulk heterojunction organic solar cells*, AIP Conf. Proc. 1280, 121 (2010).

## 4.2 Drift/Diffusion Model

The drift/diffusion model includes a solution to Poisson's and the current continuity equations whereby negatively-charge electrons ($n$) and positively-charge holes ($p$) move via drift and diffusion towards their respective electrodes. Before carrier collection, photogenerated carriers have some probability of dissociation in the internal electric field ($P_{CT}$) as dictated by Onsager-Braun theory[46] and must escape Langevin-type bimolecular recombination ($B_{photo}$) during transit[120].

The continutiy equations for electrons and holes are as follows,

$$-\frac{1}{q}\vec{\nabla}\cdot\vec{J_n} = P_{CT}G - (1-P_{CT})\,B_{photo} \tag{4.1}$$

$$\frac{1}{q}\vec{\nabla}\cdot\vec{J_p} = P_{CT}G - (1-P_{CT})\,B_{photo} \tag{4.2}$$

where the right hand side is the net generation rate, $U$, of free carriers. Next, the current equations include drift

and diffusion of these charges,

$$\vec{J_n} = -qn\mu_n\vec{\nabla}V + \mu_n kT\vec{\nabla}n \tag{4.3}$$

$$\vec{J_p} = -qp\mu_p\vec{\nabla}V - \mu_p kT\vec{\nabla}p \tag{4.4}$$

Finally, Poisson's equation accouts for the modification of the potential due to space charge,

$$\epsilon\vec{\nabla^2}V = q\,(p-n) \tag{4.5}$$

These equations are solved in *COMSOL Multiphysics* using ohmic boundary conditions[65]. For planar BHJ active layers the system is solved in one dimension along the height or z-direction of the active layer. This is a reasonable approximation given that lateral dimensions (x- and y-directions) are on the order of millimeters, while the thickness is roughly 100 nm. Another approximation of this model is that all photoexcited excitons reach the donor/acceptor interface and dissociate into bound CT states, which assumes an ideal morphology. In the Appendix, it is shown that the simulation in *COMSOL Multiphysics* gives the same result as is found in literature and is an accurate method to solve this system of equations.

After its proposal in 2005 by Koster et al.[65], there has been widespread use of this model to describe the light intensity dependence of $J_{sc}$[121] and $V_{oc}$[122], the effect of cathode work function[52], the influence of annealing on P3HT:PCBM device performance[68], and the affect of weight percentage of PCBM in MDMO-PPV:PCBM solar cells[71]. Along with polymer/fullerene BHJ devices, the model has also been applied to polymer/polymer blends[123] and polymer/oxide blends[124]. These results are summarized in the review by Blom et al.[19] where the model has been used to predict the maximum efficiency of BHJ devices[13]. In spite of this widespread use, the accuracy of both $P_{CT}$[125,126] and $B_{photo}$[127,128] in an effective medium formalism are still under intense debate[59,129]. This will be discussed in the conclusion of this thesis, and is in part due to the assumption of a perfect morphology and the observed reduced strength of Langevin bimolecular recombination for P3HT:PCBM solar cells.

## 4.3 Electro-optical Model of PC Solar Cells

While the model is well-cited for BHJ solar cells with planar photoactive layers, there is a need to model the electrical performance of devices with nonplanar geometries. Along with the PC solar cells presented in

Chapters 2 and 3, there are other organic device designs where the sub-micron periodicity of the photoactive layer along the lateral directions could affect electrical performance [97,130]. This requires two- or three-dimensional solutions to the drift/diffusion model with appropriate boundary conditions. When combined with the optical model of Chapter 2, a complete electro-optical model of device performance would be obtained for PC and other nanopatterned solar cells.

Here, two-dimensional (2-D) electro-optical simulations of the operation of BHJ organic solar cells with PC photoactive layers are presented. The model is applied to the test case of a one-dimensional (1-D) periodic PC device and a conventional planar control cell with MDMO-PPV:PCBM as the photoactive BHJ material. Enhancements of 16% in the optical performance for the PC device relative to the planar cell are observed. On the other hand, the electrical model predicts that the PC geometry alters the internal electric field in the photoactive region to decrease the electrical performance.

### 4.3.1 Test Case: 1-D Periodic MDMO-PPV:PCBM PC Solar Cells

Figure 4.1 shows a schematic of the model PC and planar solar cells. Both are constructed on glass substrates followed by anode contacts of 178 nm of ITO and 50 nm of PEDOT:PSS. The photoactive material, MDMO-PPV:PCBM, forms a nanostructured matrix for nc-ZnO in the PC device. The contrast of the index of refraction between MDMO-PPV:PCBM and nc-ZnO forms a PC photoactive layer. For the planar device, nc-ZnO acts as an optical spacer as shown in Chapters 2 and 3. Finally, aluminum is used as the cathode.

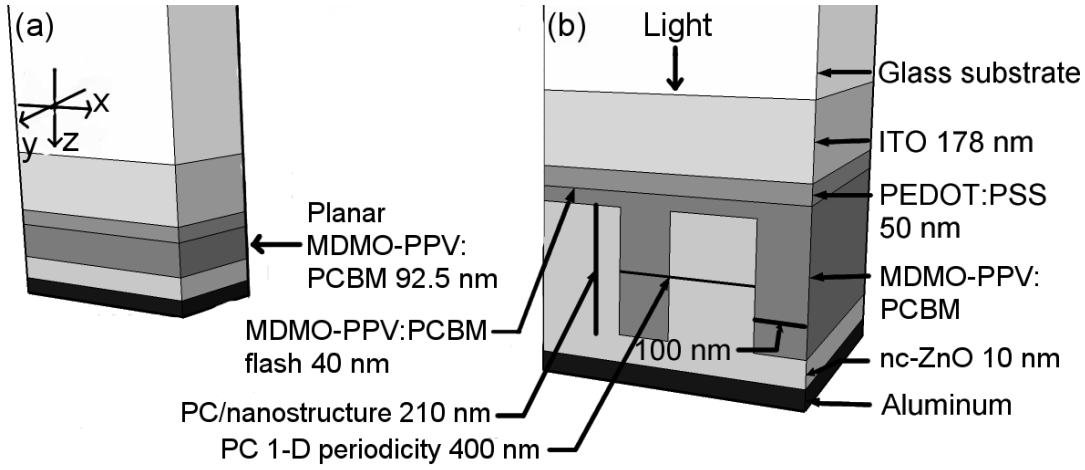


Figure 4.1: Schematic of (a) conventional planar and (b) PC solar cells. Device (b) is classified as a PC device due to the index of refraction contrast between MDMO-PPV:PCBM and nc-ZnO along with the 400 nm periodicity of the nanopattern in the x-direction.

As for the choice of physical dimensions, it was shown in Chapter 2 for P3HT:PCBM that a nanopatterned

PC layer thickness of ∼210 nm with 400 nm periodicity is optimal for maximized absorption enhancements for a 1-D periodic PC device. Even though a different BHJ is used here, these dimensions are incorporated due to the similarity between the optical properties of P3HT:PCBM and MDMO-PPV:PCBM. Furthermore, a thin flash layer of 40 nm is used as it is the common thickness obtained from the P.R.I.N.T. process. The film thickness of nc-ZnO for the planar device and nc-ZnO flash thickness for the PC cell is determined by varying both thicknesses to maximize MDMO-PPV:PCBM absorption as previously described in Chapter 2. Coincidentally, both values are 10 nm. For the planar device, the photoactive layer thickness is set to have an equivalent volume as the PC cell. This equates to 92.5 nm. As usual, the optical properties of all cell materials are measured using spectroscopic ellipsometry and closely match those from Chapter 3 and literature[31]. In terms of electrical properties, all standard parameters for MDMO-PPV:PCBM (e.g. electron and hole mobilities, dielectric constant, etc.) are used[65].

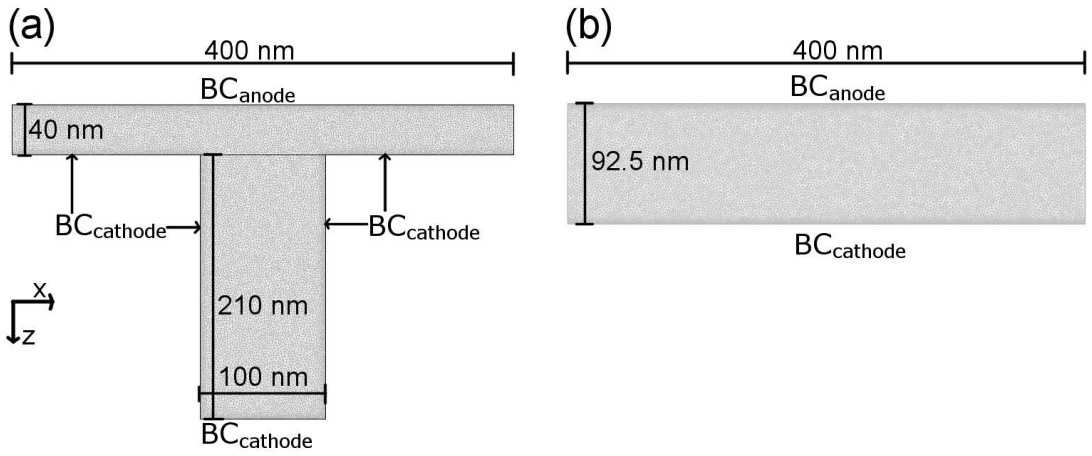


Figure 4.2: Cross sections of (a) PC and (b) planar devices used in the 2-D electrical model. Boundary conditions are labeled where the mesh of ∼23,000 finite elements is shown. Periodic boundary conditions are applied on the left and right vertical boundaries of each device at $x = 0$ and $x = 400$ nm.

Finally, the boundary conditions play an important role in the electrical performance. As with aluminum, the conduction band of nc-ZnO aligns closely with the LUMO level of PCBM, so ohmic contacts are assumed. Figure 4.2 shows the 2-D domain of the PC and planar cells where the anode and cathode boundary conditions are labeled, $BC_{anode}$ and $BC_{cathode}$, respectively. Both domains represent device cross sections of MDMO-PPV:PCBM where periodic boundary conditions are applied at $x = 0$ and $x = 400$ nm to simulate one period of the PC geometry. For the planar device, the boundary conditions are applied as for the 1-D planar solution except over a line boundary instead of a point. For the PC device, the anode boundary condition is applied as in the 2-D planar case, but the cathode boundary condition is applied for all five MDMO-PPV:PCBM/nc-ZnO interfaces. An alternative method would be to include the nc-ZnO in the simulation and have parallel boundary

conditions. This impact of this will be discussed in a later section. As shown in Fig. 4.2, a high resolution finite element mesh is used for both PC and planar devices where a finer mesh is incorporated at the cathode and anode boundaries where the solutions change rapidly. Overall, ∼23,000 elements are used for the PC and planar devices resulting in a problem with ∼150,000 degrees of freedom when the equation set is solved simultaneously.

### 4.3.2 Improved Absorption but Reduced Performance

First, the redistribution of incident light in both cells are calculated using the optical model. The fraction of light absorbed by MDMO-PPV:PCBM is then weighted against the AM 1.5 solar spectrum[88] to calculate $G$ and input into Eqns. 4.1 and 4.2 to link the optical and electrical models. An average value for $G$ is used where $G_{flash}$ represents the flash layer and $G_{NS}$ represents the nanostructured PC layer with 210 nm thickness. For the planar cell, $G_{planar}$ is a constant in the photoactive layer. A comparison between using the average or spatially-dependent $G$ will be discussed in Chapter 5.

Applying the optical model to the PC and planar devices described above results in absorption enhancements in MDMO-PPV:PCBM for the PC cell relative to the planar device. The optical redistribution of incident light is shown in Fig. 4.3 for s- and p-polarizations at normal incidence. When weighted against the AM 1.5 solar spectrum the exciton generation rate for the planar cell is $G_{planar} = 2.85 \times 10^{27}\ 1/m^3 s$. The rate for the PC device is computed separately for the flash and nanostructured layers where $G_{flash} = 3.00 \times 10^{27}\ 1/m^3 s$ and $G_{NS} = 3.53 \times 10^{27}\ 1/m^3 s$. These result in 5% and 24% enhancements for the flash and PC layers when compared to the planar cell, respectively. When averaged by a weight proportional to their volume, an overall 16% absorption enhancement is achieved. This is similar to enhancements noted for P3HT:PCBM and TDPTD:PCBM solar cells from Chapters 2 and 3.

Figure 4.3 also demonstrates the striking difference in optical redistribution for the PC cell for s- and p-polarization. S-polarization has an electric field oriented in the x-direction, while p-polarization is oriented in the y-direction. The exciton generation rates given above are an average of both polarizations. Quantitatively, $G_{NS}$ for s-polarization is 49% larger than for p-polarization, while $G_{flash}$ is essentially equal. Part of the improved absorption comes in the form of resonant mode excitation that occurs for s-polarization. One mode located near $\lambda = 590$ nm, provides absorption enhancement in MDMO-PPV:PCBM, while one located near $\lambda = 665$ nm is more highly concentrated in the ITO layer.

It is also evident from Fig. 4.3 that the primary limiting factor in optical performance is not absorption from non-photoactive layers like ITO and PEDOT:PSS, but from reflection. Especially for the planar device, a large

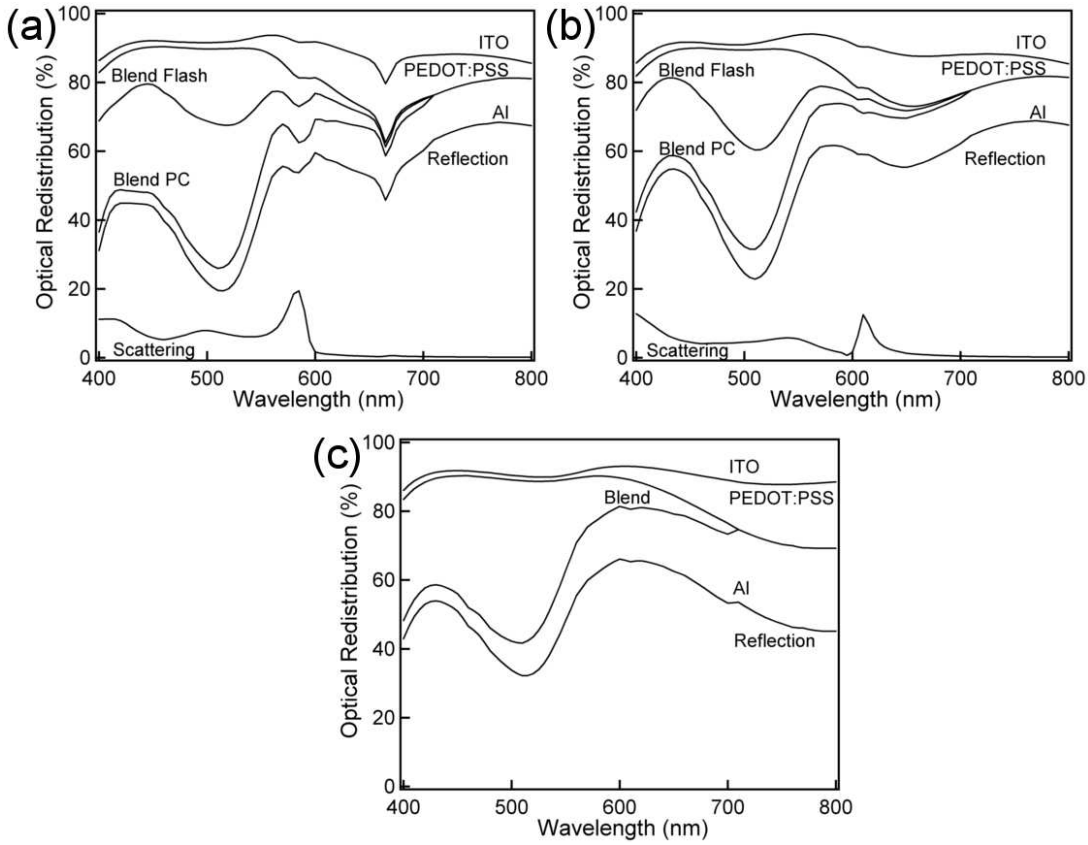


Figure 4.3: Optical redistribution of incident light for PC cell in (a) s-polarization and (b) p-polarization at normal incidence. (c) Optical redistribution for the planar cell at normal incidence in both polarizations.

fraction of incident light is reflected even in the visible range where MDMO-PPV:PCBM strongly absorbs. This is partially due to the 92.5 nm thickness of the photoactive layer. The extinction coefficient of MDMO-PPV:PCBM is also lower than that of other polymer:fullerene BHJ blends like P3HT:PCBM.

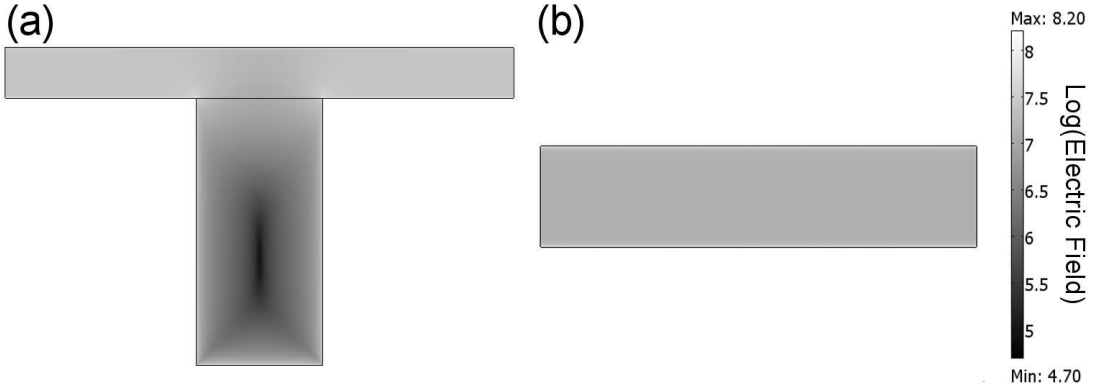


Figure 4.4: Logarithm of internal electric field at short-circuit for (a) PC and (b) planar cells. The electric field is enhanced for the PC geometry in the flash layer but reduced in the nanostructured layer.

Even though the reduced volume of MDMO-PPV:PCBM limits the optical performance for both PC and planar cells studied here, a reduced photoactive thickness for planar cells has been shown to be beneficial to the electrical performance[31]. The thickness dictates the strength of the internal electric field, which drives both $P_{CT}$ and carrier collection. Due to intrinsic physical properties of MDMO-PPV:PCBM, $P_{CT} = 61\%$ at short-circuit for a photoactive thickness of 120 nm and steadily increases for thinner layers[31]. In terms of carrier collection, for planar cells with thicknesses around 100 nm, almost all carriers reach the contacts to produce photocurrent at short-circuit.

Figure 4.4 shows the logarithm of the internal electric field at short-circuit for the PC and planar cells. For the planar cell, the field is essentially constant throughout the photoactive layer except near the anode and cathode boundaries. Here it is stronger due to the build-up of space charge in the form of holes near the anode and electrons near the cathode. For the PC cell, the field varies significantly throughout the photoactive region. On average, it is observed to be over two times stronger in the flash layer compared to the planar device but less than half as strong in the nanostructured layer. Furthermore, the field reaches it lowest value in the middle of the nanostructure. Due to the dependence of the internal field on $P_{CT}$ and carrier collection, the PC geometry is predicted to have a significant influence on the extracted photocurrent.

The exciton dissociation probability is shown for both PC and planar cells at short-circuit in Fig. 4.5. The planar cell behaves as expected where an average value of $P = 64\%$ is obtained[31]. As with the internal field, $P_{CT}$ increases near the anode and cathode boundaries and is essentially constant throughout the bulk. For the


Figure 4.5: Exciton dissociation probability, $P_{CT}$, for (a) PC and (b) planar cells. $P_{CT}$ is enhanced in the flash layer but reduced in the nanostructured layer relative to the planar cell.

PC cell, the variation in the field for the flash and nanostructured layers yields average values of $P_{flash} = 76\%$ and $P_{NS} = 50\%$. An average value of $P = 61\%$ for the PC cell signifies a slight reduction compared to the planar cell. Furthermore, the nanostructured layer of the PC cell has a larger $G$ than the flash layer, which happens to be the region with weaker $P_{CT}$.

Figure 4.6 shows the other electrical process dependent on the internal field, the bimolecular recombination rate ($B_{photo}$ in Eqns. 4.1 and 4.2). This rate describes the loss of free charge carriers due to recombination. For the planar cell, there is minimal recombination throughout the photoactive layer. Near the cathode boundary, there is a slight increase due to the order of magnitude difference in electron and hole mobility for MDMO-PPV:PCBM, but this does not lead to significant recombination. On average, only 5% of free charge carriers undergo bimolecular recombination for the planar device. On the other hand, for the PC cell, there are large differences in the recombination rates for the two layers. In the flash layer, only 2% of free carriers recombine, while a massive 71% recombine in the nanostructured layer. On average, this equates to an 8.4-fold increase in recombination compared to the planar cell.

The culminating calculation from the electro-optical model is $J_{sc}$. This is a measure of the combined electrical and optical performance. Even with the enhanced absorption of the PC cell, $J_{sc} = 17.9$ A/m$^2$ while for the planar cell $J_{sc} = 25.2$ A/m$^2$. Due to near equal levels of $P_{CT}$ for the PC and planar cells, the reduction in $J_{sc}$ can be attributed to the signification bimolecular recombination rate for the PC device that occurs in the nanostructured layer.


Figure 4.6: Bimolecular recombination rate, $B_{photo}$ in units of $\left(1/m^3 s\right)$, for (a) PC and (b) planar cells. Very low bimolecular recombination occurs in the flash layer of the PC cell and the entire planar cell. Due to the weak internal electric field in the nanostructured layer of the PC cell, strong recombination occurs.

### 4.3.3 Bondary Conditions Play a Big Role in Device Performance

Given the improvement in light absorption, it is interesting that there is reduced performance for the PC cell from above in terms of $J_{sc}$. In the example above, this is due to the reduce electric field inside the post that significantly strengthens bimolecular recombination losses. However, this model does not explicitly include the electron transport layer (nc-ZnO) in the drift/diffusion model. This can be done by simply interfacing the ETL next to the BHJ nanopattern and choosing reasonable values for the dielectric constant and electron mobility of the ETL. Also, no free carriers are created in this material, so $G$ is assumed to be zero. The same ohmic boundary conditions can be applied to the flat anode side of the BHJ and flat cathode side of the ETL. This is shown in Fig. 4.7 along with the boundary conditions where the ETL is disregarded as used in the previous section.

Figure 4.7 demonstrates the influence of the boundary conditions on the internal field for a P3HT:PCBM BHJ with an equivalent volume of P3HT:PCBM as a 100 nm thick planar cell. The relative dielectric constant of the ETL is taken to be 10.2, $G$ is taken as constant throughout the BHJ where all cases have equal values, and $\mu_{n,p}$ match those for P3HT:PCBM. It is not shown here, but the critical parameter that influences device performance for a model that includes the ETL is $\mu_n$. The value used here ($\mu_n = 2.0$ x $10^{-7}$ $m^2$/Vs) is suitable to have minimal influence on the J-V curve for a planar cell when the ETL is included in the model. Likewise, this value is close to that measured for another ETL, $TiO_x$ [29], where the ETL does not reduce electrical performance compared to a planar cell without an ETL [58,104].

Figure 4.7 shows that depending on the mobility of electrons and holes and whether or not the ETL is included has a significant influence on the internal field and build-up of space charge. For example, Fig. 4.7(c) shows the

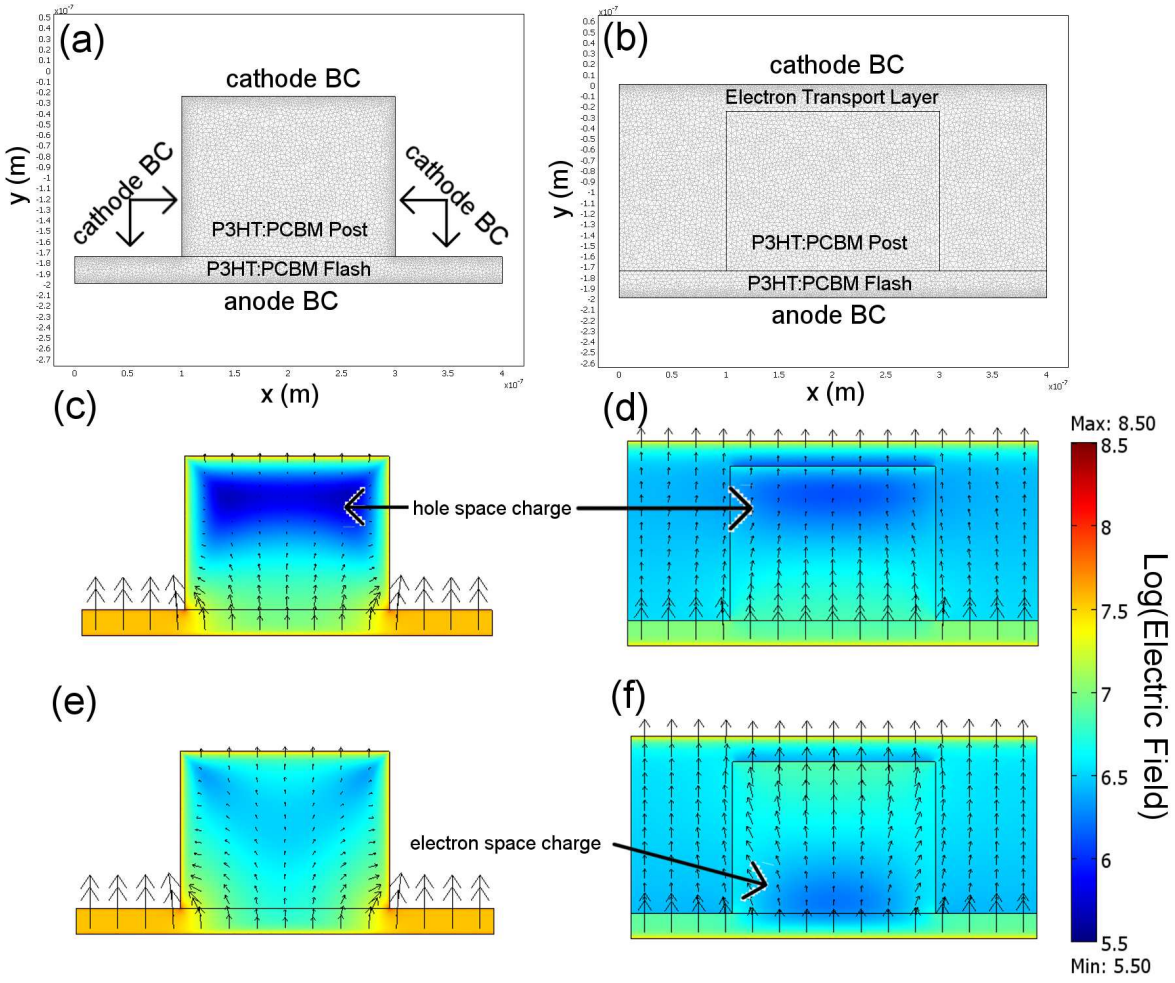


Figure 4.7: Schematics of (a) PC cell without ETL and (b) PC cell with ETL where the finite element mesh is shown. Parameters for P3HT:PCBM are used. Please note the different boundary conditions for each. (c-f) Log of electric field at short-circuit for each structure using (c,d) $\mu_n = 20\mu_p$ and (e,f) $\mu_n = \frac{1}{20}\mu_p$. Depending on the mobility, space charge is apparent for the slower carrier, especially for (c). Arrows in (c-f) indicate the negative direction of the electric field, or the direction of electron transport. Depending on the boundary conditions applied, the field lines are either curved for (c,e) or almost vertical for (d,f).

model without an ETL where $\mu_n = 20\mu_h$. Because the holes need to travel a longer distance than the electrons to escape the BHJ and they have a much lower mobility, there is a build-up of space charge and weakening in the internal field. Figure 4.8 shows that this has a profound influence on device performance where the efficiency is reduced for this case. On the other hand, if $\mu_n = \frac{1}{20}\mu_h$, the holes are swifter than the electrons and are able to cover their longer transport path set-up by the geometry of the nanopattern. In terms of device performance, this case performs as well as that of the planar cell. When the ETL is included, the same effects occur, just on a smaller scale. When using an ETL, it is better to have $\mu_n < \mu_p$. For a hole transporting layer, the opposite would be true. Furthermore, the field lines are essentially vertical when the ETL is included (Fig. 4.7(d,e)) whereas they have tremendous curvature when the ETL is not included.

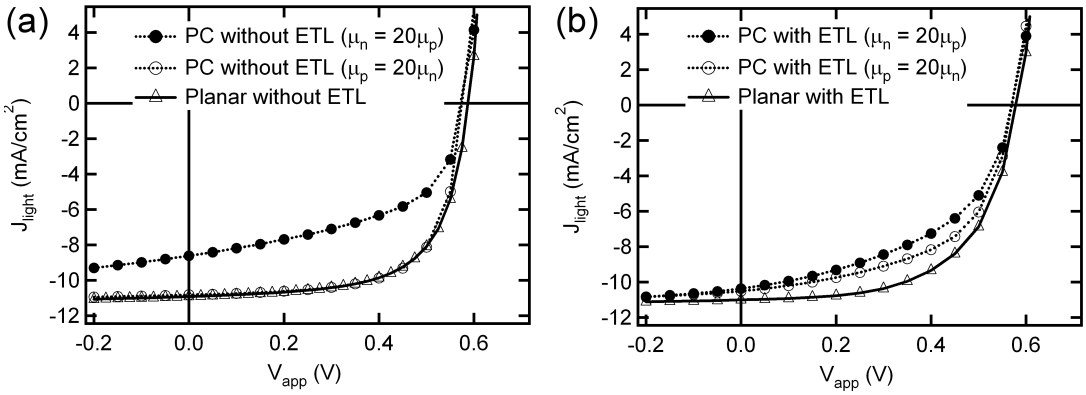


Figure 4.8: Simulated device performance of P3HT:PCBM devices (a) with and (b) without an electron transporting layer as shown in Fig. 4.7. In all cases, PC cell performance is comparable to or worse that planar cell performance. Light absorption is equal for all cases showing only the effect of the geometry on electrical performance.

It is observed that the application of boundary conditions in the model has a strong influence on device performance. Whichever is the correct application, it should be noted from Fig. 4.8 that the PC cell, regardless of mobility values or decision to include the ETL, does not outperform the planar cell. For the case of $\mu_n < \mu_p$, the PC cells are comparable to the planar cells. However, BHJ systems like P3HT:PCBM and MDMO-PPV:PCBM have $\mu_n > \mu_p$, which indicates that a hole instead of electron transporting layer would be better for device performance. None of the fabrication attempts presented in this thesis match this requirement. Likewise, the improved electrical performance for TDPTD:PCBM solar cells remains puzzling. Based on these results, exciton dissociation and charge transport do not appear as likely candidates to explain the observed improvements.

## 4.4 Affect of Parasitic Resistances

In order to determine if the levels of space-charge predicted in the PC models above are accurate, light intensity measurements of PC cells need to be done. As described in Chapter 1, a linear scaling of the photocurrent with light intensity would signify low levels of recombination and challenge the models presented above. Along with space charge build-up that leads to bimolecular recombination[68,131], light intensity measurements are also commonly related to other physical mechanisms like CT state dissociation[122] and charge trapping effects[123]. Therefore, it is a powerful technique to study the efficiency of underlying physical processes in BHJ solar cells.

However, it is not widely recognized that non-ideal parasitic resistances can also affect the scaling of the photocurrent with light intensity. In this section, the influence of parasitic resistances is fully explored. Handling $R_{sr}$ and $R_{sh}$ is also compared between both drift/diffusion and equivalent circuit models, which is significantly different. While $R_{sr}$ and $R_{sh}$ are clearly defined parameters in the equivalent circuit model, they are assumed to be ideal in drift/diffusion approaches. In other words, $R_{sr}$ is near zero, while $R_{sh}$ approaches infinity. Since drift/diffusion models capture more of the fundamental physics of BHJ solar cells, it is imperative to systematically explore the impact of relaxing these conditions. Given that different photoactive materials have different intrinsic properties, it is important to determine the influence of non-ideal parasitic resistances for different BHJ solar cells.

Furthermore, even though there is widespread use of each type of model to explain OPV operation, there has been little work to determine relationships between the way each describes the same physical process. For example, it is widely believed that CT state dissociation is a critical process in photocurrent generation for BHJ solar cells, regardless of donor and acceptor material.[131] The signature of this process in the standard J-V measurement is a photocurrent that increases under reverse bias and eventually saturates.[47] In the equivalent circuit model, a non-ideal $R_{sh}$ fits this trend around short-circuit,[14,132] while an electric field dependent probability of CT state dissociation ($P_{CT}$) from Onsager-Braun theory[46] is utilized in the drift/diffusion approach.[65] Up to now, no relationship has been posited between these two descriptions. A turn is taken away from studying PC cells for the remainder of this chapter in order to fully understand the interplay between light intensity, parasitic resistances, and fundamental recombination processes.

### 4.4.1 Comparing Equivalent Circuit and Drift/Diffusion Models

Frequently, explanations for device $J_{sc}$, $V_{oc}$, and FF are linked to altered $R_{sr}$ and $R_{sh}$. For example, inserting electron and/or hole transporting layers between the photoactive layer and electrodes can increase power conversion efficiency (PCE) where a reduction in $R_{sr}$ is commonly cited.[114,133,134] Likewise, a low $R_{sh}$ has been used to explain pinhole shorting through the photoactive layer.[7,132] These explanations are conveniently tied to the equivalent circuit model where $R_{sr}$ and $R_{sh}$ are included in a simple mathematical framework. Even though more complicated multiple diode[135] and mobility-dependent models[136] have been utilized, the most basic equivalent circuit model for BHJ solar cells[53] was developed for inorganic devices:[116]

$$J = J_0 \left[ exp\left( \frac{q\left(V_{app} - JR_{sr}\right)}{n_d k_B T} \right) - 1 \right] + \frac{V_{app} - JR_{sr}}{R_{sh}} - J_{photo} \tag{4.6}$$

where $J$ is the measured current density, $J_0$ is the reverse saturation current density, $q$ is the elementary charge, $n_d$ is the diode ideality factor, $k_B$ is Boltzmann's constant, $T$ is the temperature, $V_{app}$ is the applied voltage, and $J_{photo}$ is the voltage-independent photogenerated current density.

While this model simply incorporates devices resistances, it does not elucidate the underlying physics of photocurrent generation, e.g., CT state dissociation and free carrier transport. As described above, these processes are explicit terms in the drift/diffusion model.

In order to demonstrate the impact of non-ideal resistances for different BHJ systems, $R_{sr}$ is first addressed. As opposed to non-ideal $R_{sh}$, $R_{sr}$ has a greater influence on device performance under light intensities approaching 1 Sun as will be discussed below. For this reason, $R_{sr}$ is more commonly employed as an explanation for poor device performance. In the equivalent circuit model, an increase in $R_{sr}$ essentially reduces the potential difference across the device. This reduction can be incorporated into the drift/diffusion framework by adding a term to the voltage boundary conditions applied at the anode and cathode ends of the photoactive layer:

$$V_{anode} - V_{cathode} = V_{gap} - \left(V_{app} - JR_{sr}\right) \tag{4.7}$$

where $V_{gap}$ is the built-in voltage set by the energy levels of the donor/acceptor system, $V_{app}$ is the applied voltage, and $J$ is the extracted current density dependent on $V_{app}$. This modification to the boundary conditions insures that $V_{oc}$ will be independent of $R_{sr}$ as is the case for the equivalent circuit model.[53] At open-circuit, $J = 0$, so there is no modification to the boundary condition at this voltage.

### 4.4.2 Experimental Details

In order to control $R_{sr}$, a variable external resistance load, $R_{srE}$, was connected in series with the BHJ devices and adjusted from 0 Ω to 1x10$^4$ Ω as shown in Fig. 4.9(a). Current measurements were then performed under variable applied bias and light intensity. The two BHJ active materials chosen herein, MDMO-PPV:PCBM and P3HT:PCBM, were selected based on their different field dependencies of $P_{CT}$.[68] In the Braun-Onsager approach, $P_{CT}$ is dependent on the internal electric field as shown in Fig. 4.9(b). Two parameters that control the field dependence of $P_{CT}$, both the electron/hole pair separation distance ($a$) and decay rate ($k_f$) were fit to match the measured current under illumination ($J_{light}$). The field dependence of $P_{CT}$ qualitatively matches that reported for P3HT:PCBM (weak field dependence)[68] and MDMO-PPV:PCBM (strong field dependence)[65]. All model parameters are listed in Table 4.1 including the method of determination (i.e. independently measured, fit to $J_{light}$, or taken from literature). It should be noted that the exciton generation rate ($G$) and active layer thickness ($t$) were measured independently by applying an optical model to the measured device reflection using optical properties determined from spectroscopic ellipsometry (see Chapter 3). Finally, in the comparison between the equivalent circuit and drift/diffusion models, parameters for the equivalent circuit model were required for MDMO-PPV:PCBM devices and are given at the bottom of Table 4.1.

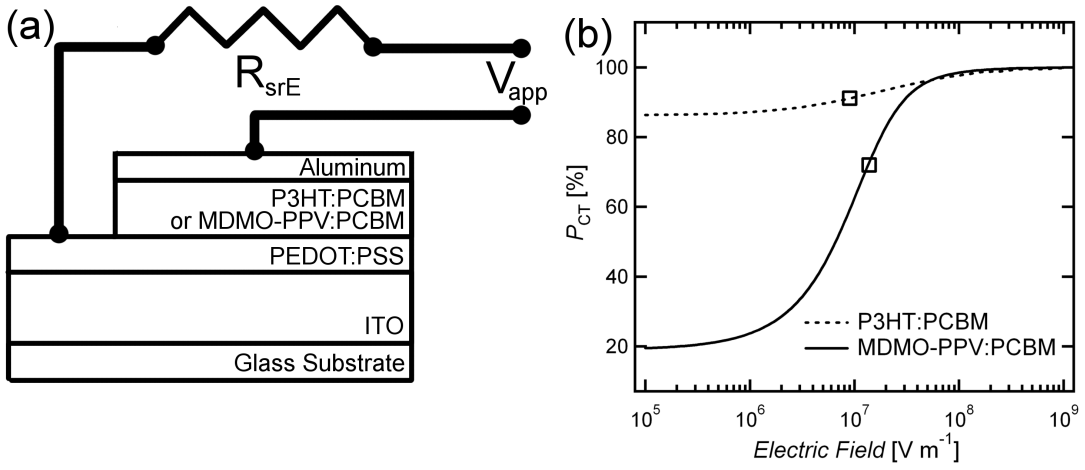


Figure 4.9: (a) Schematic of experimental setup where a variable external resistor ($R_{srE}$) is connected in series with BHJ devices. (b) Dissociation probability of CT state ($P_{CT}$) for both P3HT:PCBM and MDMO-PPV:PCBM from Onsager-Braun theory. Squares represent $P_{CT}$ under short-circuit conditions for $R_{sr} \rightarrow 0$ Ω cm$^2$.

Devices were prepared by first sonicating ITO-coated (140 nm) glass substrates in acetone, isopropyl alcohol, and distilled water for 10 min each and then dried in an oven overnight (150 °C). Next, the cleaned substrates were treated with UV ozone for 20 min (UVO Cleaner 42, Jelight Company Inc.). A solution of PEDOT:PSS (Baytron PH500) was then spincoated (40 nm) and annealed in air at 140 °C for 10 min. The samples where then

Table 4.1: Parameters used for drift/diffusion (top section) and equivalent circuit (bottom section) modeling of devices with P3HT:PCBM and MDMO-PPV:PCBM as the photoactive layer.

| Parameter | Symbol [unit] | P3HT:PCBM | MDMO-PPV:PCBM | Method |
|---|---|---|---|---|
| electron mobility | $\mu_n$ [$m^2V^{-1}s^{-1}$] | $2.0x10^{-7}$ | $2.5x10^{-7}$ | Lit.[13,65] |
| hole mobility | $\mu_p$ [$m^2V^{-1}s^{-1}$] | $1.5x10^{-8}$ | $3.0x10^{-8}$ | Lit.[13,65] |
| exciton generation rate | $G$ [$m^{-3}s^{-1}$] | $7.3x10^{27}$ | $3.9x10^{27}$ | measured |
| built-in voltage | $V_{gap}$ [V] | 0.90 | 1.24 | fit |
| active layer thickness | $t$ [m] | $1.0x10^{-7}$ | $9.0x10^{-8}$ | measured |
| e/h pair separation distance | $a$ [m] | $1.8x10^{-9}$ | $3.2x10^{-9}$ | fit |
| e/h pair decay rate | $k_f$ [$s^{-1}$] | $2.0x10^{4}$ | $1.3x10^{8}$ | fit |
| dielectric constant | $\epsilon$ [$C^2N^{-1}m^{-2}$] | $3.0x10^{-11}$ | $3.0x10^{-11}$ | Lit.[13,65] |
| temperature | $T$ [K] | 300 | 300 | measured |
| density of states | $N_0$ [$m^3$] | $2.5x10^{25}$ | $2.5x10^{25}$ | Lit.[65] |
| diode ideality factor | $n_d$ [unitless] | n/a | 2.0 | Lit.[137] |
| reverse saturation current | $J_0$ [$Am^{-2}$] | n/a | $1.0x10^{-5}$ | fit |

moved to an inert gas (purified nitrogen) glovebox where a solution of either P3HT (15 mg $mL^{-1}$) and PCBM (12 mg $mL^{-1}$) or MDMO-PPV (4 mg $mL^{-1}$) and PCBM (16 mg $mL^{-1}$) in chlorobenzene was spincoated on the ITO/PEDOT:PSS coated substrates. Finally, the devices were transferred to a vacuum chamber (2 x $10^{-6}$ torr) where 90 nm Al was deposited on defined cell areas (12 $mm^2$). P3HT:PCBM devices were annealed at 150 °C for 30 min in the glovebox prior to characterization.

### 4.4.3 Influence of Non-ideal $R_{sr}$

Figure 4.10 shows the modeled and experimental J-V characteristics under AM 1.5 illumination for devices with P3HT:PCBM and MDMO-PPV:PCBM as the photoactive layer with varying $R_{sr}$. Here, $R_{sr}$ is determined by taking the inverse slope of the experimental data roughly 0.2 V higher in bias than open-circuit. These values are then used in the modified boundary condition of the drift/diffusion model to simulate the J-V curves. While there is slight overestimation in taking the slope at these voltages compared to higher ones near 2 V[7], it is more accurate than the common approach of taking the slope at open-circuit,[114] and protects against device breakdown during repeated measurements. From this figure, it is clear that the modification to the voltage boundary condition is an appropriate way to model $R_{sr}$ in the drift/diffusion formalism. Not only does $V_{oc}$ remain constant, but changes in $R_{sr}$ closely match those of the known external resistor, $R_{srE}$.

Figure 4.11 shows $J_{sc}$, FF, and PCE as functions of $R_{sr}$ for both P3HT:PCBM and MDMO-PPV:PCBM devices. As $R_{sr}$ increases, there are cross-over points for all three measures of performance where MDMO-PPV:PCBM devices outperform P3HT:PCBM solar cells. Furthermore, the $J_{sc}$ is less affected than the FF under increasing $R_{sr}$ for both device types. While this is a well known result for the equivalent circuit model,[53] it is not expected that there would be such striking differences between BHJ solar cells with different photoactive

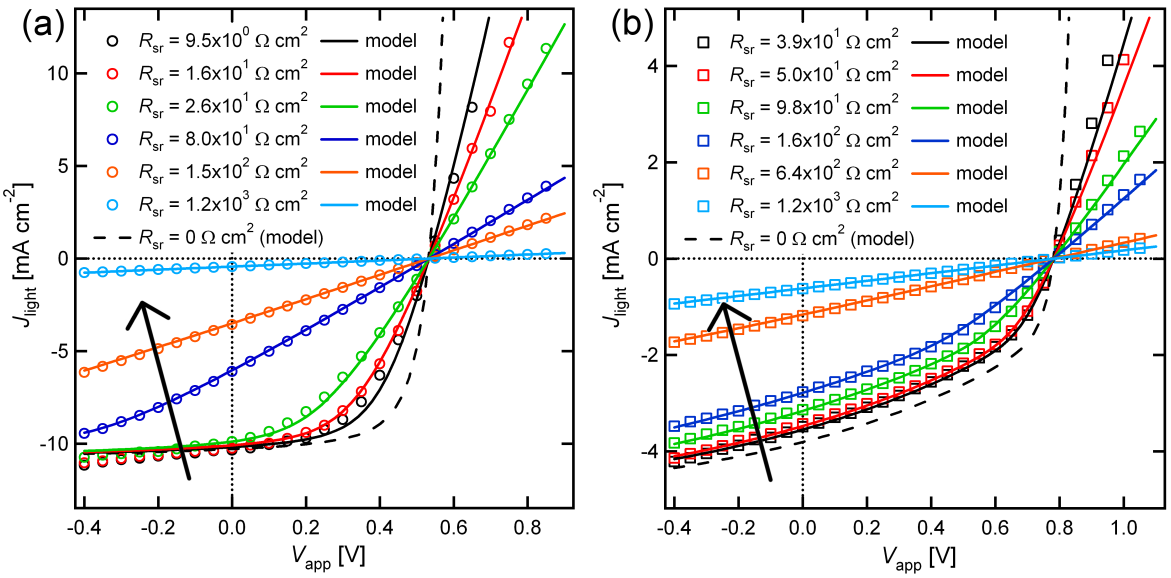


Figure 4.10: Experimental and modeled J-V curves for (a) P3HT:PCBM and (b) MDMO-PPV:PCBM as the photoactive layer with different $R_{sr}$. Arrows indicate increasing $R_{sr}$. Models are derived from the drift/diffusion approach using the electric field dependent probability of CT state dissociation ($P_{CT}$) of Fig. 4.9(b).

layers. In particular, the FF of MDMO-PPV:PCBM devices is less sensitive to $R_{sr}$: it exhibits a more gradual decline with increasing $R_{sr}$. Likewise, the FF for P3HT:PCBM devices begins to drop almost immediately compared to behavior with MDMO-PPV:PCBM and reaches the minimum of 25% at a much lower $R_{sr}$ value.

These observations are attributed to the combination of differing field dependencies of $P_{CT}$ (see Fig. 4.9(b)) and light absorption. First, for ideal $R_{sr}$, a weak $P_{CT}$ field dependence is desired, so that the photocurrent, which is proportional to $P_{CT}$, will remain high at the maximum power point and yield a high FF. However, as $R_{sr}$ increases away from ideality, a strong field dependence, as is the case for MDMO-PPV:PCBM, causes the photocurrent to drop at both short-circuit and maximum power point. This results in a FF that is less sensitive to $R_{sr}$. Further insight is gained by simulating a fictitious MDMO-PPV:PCBM solar cell where $P_{CT}$ is replaced with that for P3HT:PCBM. Compared to actual MDMO-PPV:PCBM devices, the weaker $P_{CT}$ field dependence causes the FF to increase from 45% to 77% for $R_{sr} \to 0\ \Omega\ \text{cm}^2$. However, the FF also undergoes a sharper decline for increasing $R_{sr}$, which closely resembles the dependence for P3HT:PCBM devices. Finally, light absorption, as quantified by the $G \cdot t$ product (see Table 4.1), can also limit the FF for ideal $R_{sr}$ as evidenced by comparing P3HT:PCBM devices with the fictitious MDMO-PPV:PCBM solar cell model. The FF dependence essentially shifts up and to the right for lower light absorption. In conclusion, both light absorption and the field dependence of $P_{CT}$ affect solar cell response to $R_{sr}$.

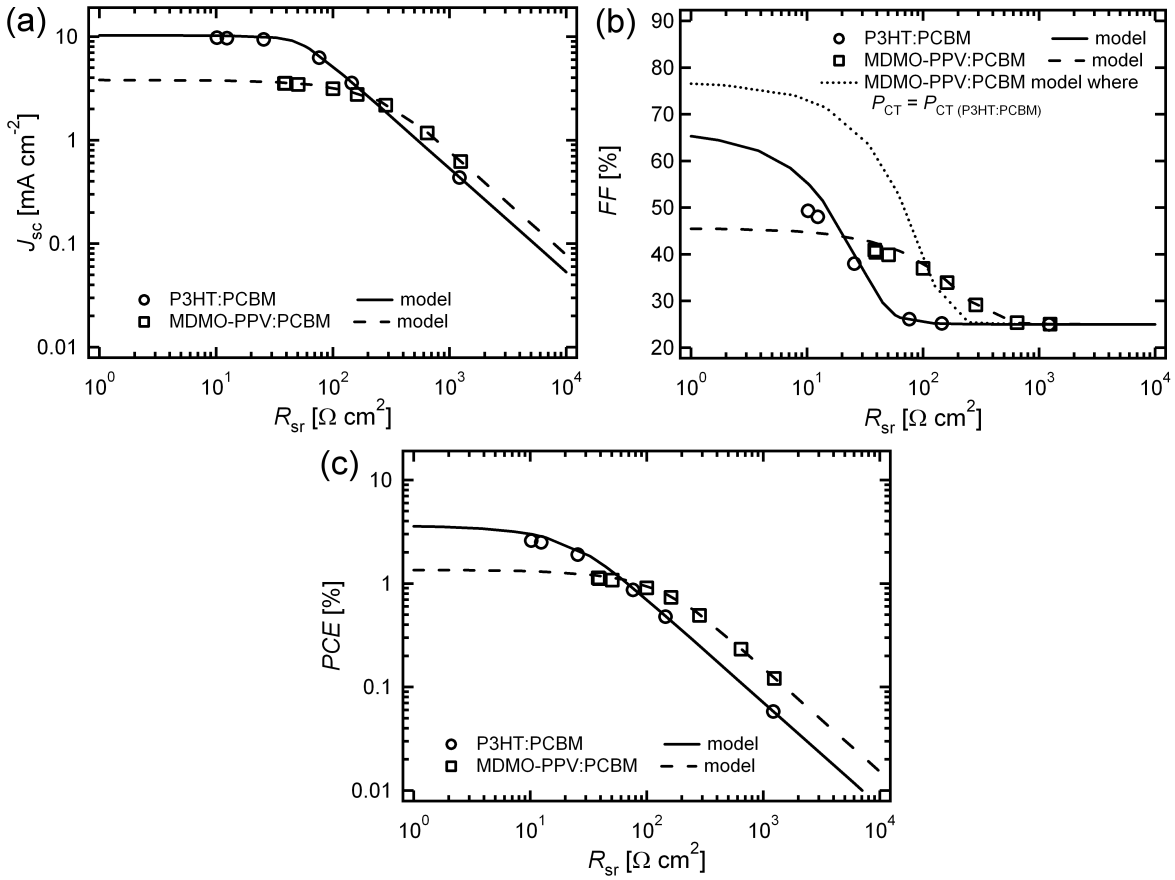


Figure 4.11: (a) $J_{sc}$, (b) FF, and (c) PCE of devices with P3HT:PCBM and MDMO-PPV:PCBM as the photoactive layer under 1 Sun conditions as functions of $R_{sr}$. A fictitious MDMO-PPV:PCBM device where $P_{CT}$ is replaced with that of P3HT:PCBM is also given for FF in (b).

### 4.4.4 Non-ideal Resistances and Light Intensity Measurements

In this section, the relationship between non-ideal resistances and light absorption is more systematically explored by analyzing the light intensity dependence of the photocurrent. Frequently, light intensity is related to photocurrent output, usually at short-circuit, through a power law relationship.[56,131,138,139] Non-linearities can indicate significant bimolecular recombination that can even induce space-charge limited behavior[51].

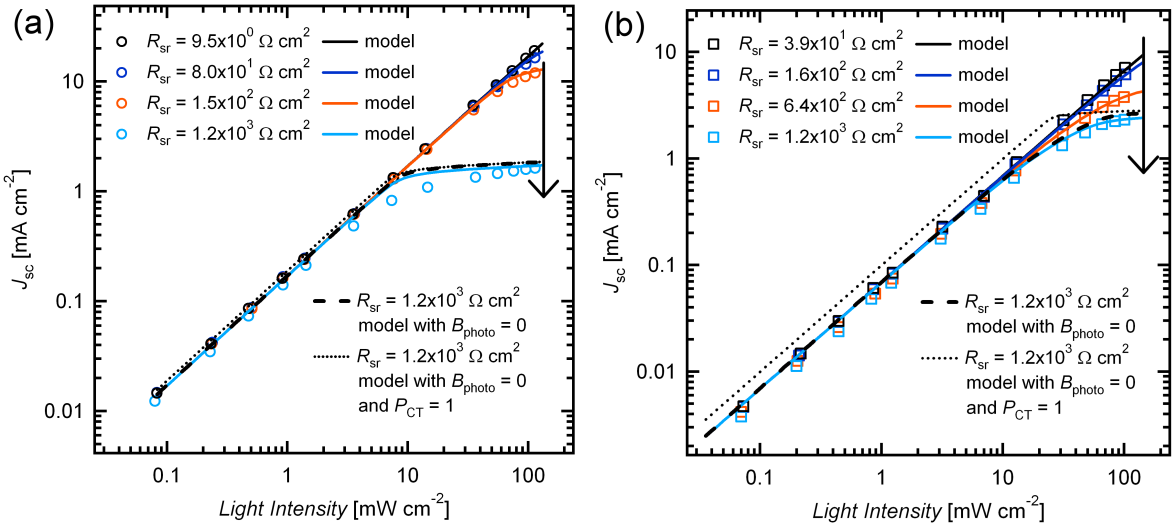


Figure 4.12: Light intensity dependence of $J_{sc}$ for devices with (a) P3HT:PCBM and (b) MDMO-PPV:PCBM as the photoactive material where arrows indicate increasing $R_{sr}$. Model predictions are also given where $B_{photo}$ = 0 along with simulations of ideal devices where $P_{CT}$ = 1 for all electric fields and $B_{photo}$ = 0.

Figure 4.12 shows the light intensity dependence and drift/diffusion model predictions of $J_{sc}$ for both P3HT:PCBM and MDMO-PPV:PCBM devices under variable $\lambda$ = 532 nm laser illumination. The response is linear over the entire range for the lowest $R_{sr}$ and becomes sub-linear for high light intensity as $R_{sr}$ increases. Usually, the sub-linearities would be due to significant bimolecular recombination as is often the case when this type of behavior is observed. However, when the non-linear regions are fit to a power law, the exponent is below that for a space charge limited device (i.e. 0.75)[51] and approaches logarithmic behavior.

The physical explanation for the non-linearity can be probed by turning off bimolecular recombination in the model (i.e. setting $B_{photo}$ in Eqns. 4.1 and 4.2 to zero) for the most non-linear case of $R_{sr}$ = 1.2 x 10$^3$ Ω cm$^2$. If there is significant loss due to $B_{photo}$, then the current should increase in the non-linear region and again become linear when $B_{photo}$ is eliminated. However, near 100 mW cm$^{-2}$ the model prediction only increases by about 10% for both P3HT:PCBM and MDMO-PPV:PCBM devices. Going a step further, $P_{CT}$ may also be equated to unity for all electric fields, which, when combined with $B_{photo}$ = 0, eliminates all photogenerated current loss processes in the model. Interestingly, the $J_{sc}$ only increases slightly and still retains non-linear behavior for

this ideal case. Even though these measurements are carried out at short-circuit, when they are analyzed with regard to the effective applied voltage (i.e. $V_{app}$ - $JR_{sr}$ in Eqns. 4.6 and 4.7), it becomes clear that for high $R_{sr}$, the short-circuit measurement actually approaches open-circuit conditions. Thus, the dark or injected current dictated by the exponential term in Eqn. 4.6 works to reduce $J_{photo}$ even at short-circuit. The near logarithmic LI scaling is not surprising as the light intensity dependence of $J_{sc}$ for high $R_{sr}$ is actually identical to that at open-circuit.

From these results, the assumption of ideal $R_{sr}$ when scaling to light intensity is justified if $R_{sr}$ is below 1.0x10$^2$ Ω cm$^2$. For some reported devices, interface and contact resistances reach this level.[67,117] Furthermore, the photocurrent near open-circuit is also frequently scaled to light intensity[68,131] where smaller $R_{sr}$ losses will have a greater impact.

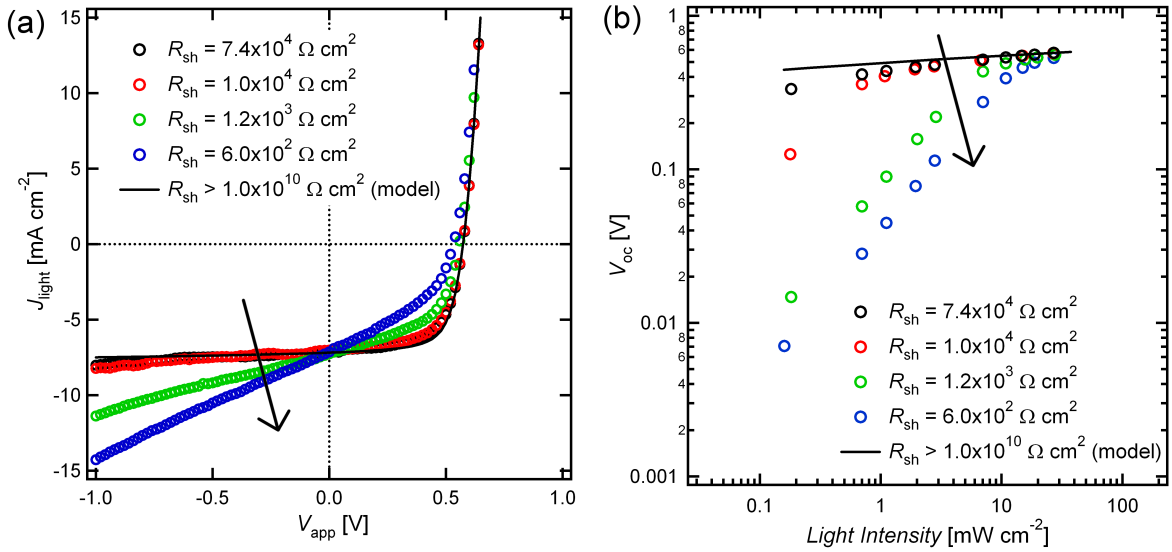


Figure 4.13: (a) J-V curve under 30 mW cm$^{-2}$ $\lambda$ = 532 nm laser illumination with varying levels of $R_{sh}$ as determined from the inverse slope of the $J_{dark}$ curves at short-circuit. Arrows indicate decreasing $R_{sh}$. (b) Light intensity dependence of $V_{oc}$ where high $R_{sh}$ results in the usual logarithmic behavior, while reduced $R_{sh}$ causes the dependence to be linear for low light intensity.

Like non-ideal $R_{sr}$ under high light intensity, $R_{sh}$ under low light intensity can skew determination of the scaling of $V_{oc}$. Usually, this dependence is logarithmic[122] even though trapping and other effects can cause modifications.[123] The effect of non-ideal $R_{sh}$ is demonstrated by placing a known resistor in parallel with the device instead of in series. Figure 4.13(a) shows the effect of the J-V curve for P3HT:PCBM solar cells for an incident intensity of 20 mW cm$^2$ under $\lambda$ = 532 nm laser illumination. Here, $R_{sh}$ is calculated from the inverse slope of the dark J-V curve.[7] Even though changes are hardly noticeable until values fall below $R_{sh}$ = 1.0x10$^4$ Ω cm$^2$, there are obvious modifications for the light intensity dependence of $V_{oc}$. Likewise, the drift/diffusion

model is determined to assume an ideal $R_{sh}$ of at least 1.0x10$^{10}$ $\Omega$ cm$^2$. This assumption makes little difference in the J-V curve under illumination, but does impact the scaling of $V_{oc}$.

Interestingly, the $V_{oc}$ light intensity dependence shows greater deviation for non-ideal $R_{sh}$ in the low intensity regime, whereas the scaling of $J_{sc}$ for non-ideal $R_{sr}$ is modified under higher light intensities (see Fig. 4.12). Furthermore, non-ideal $R_{sr}$ does not impact $V_{oc}$, while non-ideal $R_{sh}$ does not affect $J_{sc}$. It is thus important to consider these scaling modifications when attempting to link the light intensity dependence of $V_{oc}$ to fundamental physical processes, especially under low illumination levels[131,138].

### 4.4.5 Description of CT State Dissociation in Competing Models

Now that we have considered the light intensity scaling of both $J_{sc}$ and $V_{oc}$, it is important to compare both the equivalent circuit and drift/diffusion model's treatment of CT state dissociation. The experimental signature of this process in the standard J-V measurement is a photocurrent that increases under reverse bias and eventually saturates. As previously explained in the drift/diffusion model, CT state dissociation is handled by the field dependence of $P_{CT}$ as given by the Onsager-Braun formalism (Fig. 4.9(b)). However, in the equivalent circuit approach, CT state dissociation can be modeled by splitting the shunt resistance under illumination, $R_{shL}$, into two parts, one that describes the shunt resistance in the dark, attributed to device pinholes and current leakage, $R_{sh}$, and another that handles CT state dissociation, $R_{shCT}$:

$$R_{shL}^{-1} = R_{sh}^{-1} + R_{shCT}^{-1} \tag{4.8}$$

Herein, $R_{shL}$ is measured under illumination to be the inverse slope of the J-V curve at short-circuit. Likewise, $R_{sh}$ is taken as the inverse slope in the dark, which allows $R_{shCT}$ to be be calculated. As shown in the previous section, $R_{sh}$ is determined to take values above 1.0x10$^{10}$ $\Omega$ cm$^2$ in the drift/diffusion model. Furthermore, $R_{shCT}$ has previously been related to device photoshunts[132] and was only recently linked to CT state dissociation processes in the equivalent circuit approach[14]. For BHJ blends like MDMO-PPV:PCBM with strong $P_{CT}$ field dependence, the slope at short-circuit is higher than for weakly dependent $P_{CT}$ materials like P3HT:PCBM (see Fig. 4.10). In the equivalent circuit model, this leads to lower values of $R_{shCT}$.

Figure 4.14(b) gives the experimental light intensity dependence of $R_{shCT}$ for MDMO-PPV:PCBM devices under various levels of $\lambda = 532$ nm laser illumination. This result agrees with $R_{shCT}$ calculations of the predicted J-V curves from the drift/diffusion model. However, under variation of light intensity, the drift/diffusion model

does not require a light intensity dependent $P_{CT}$. On the contrary, a single field dependent function for $P_{CT}$ is adequate. This is indicated in Fig. 4.14(a) by the constant $P_{CT}$ determined at short-circuit. This comparison demonstrates the relationship between the drift/diffusion approach that uses a light intensity independent $P_{CT}$ and the equivalent circuit model that incorporates a shunt resistance that varies with light intensity. For MDMO-PPV:PCBM devices, $R_{shCT}$ = 340 Ω cm$^2$ under 100 mW cm$^{-2}$ illumination corresponds to $P_{CT}$ = 70% at short-circuit.

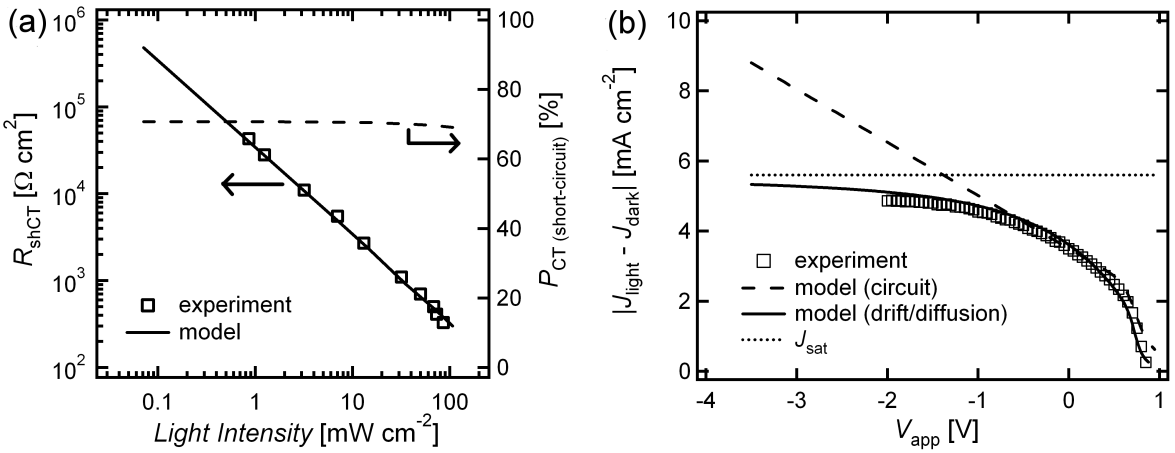


Figure 4.14: (a) Experimental and modeled $R_{shCT}$ that describes CT state dissociation in the equivalent circuit model (Eqn. 4.6) for devices with MDMO-PPV:PCBM as the active layer. In the drift/diffusion model, this corresponds to a $P_{CT}$ that is independent of light intensity. (b) Experimental photocurrent ($|J_{light} - J_{dark}|$) of MDMO-PPV:PCBM devices with both equivalent circuit and drift/diffusion model predictions. At high reverse bias, the equivalent circuit prediction is larger than the saturated photocurrent ($J_{sat}$) that is dictated solely by light absorption.

While this straightforward relationship between each model's treatment of CT state dissociation bridges a gap between the two formalisms, the equivalent circuit model does make a prediction of the photocurrent ($|J_{light} - J_{dark}|$) that is unphysical. As shown in Figure 4.14(b), the experimental photocurrent for MDMO-PPV:PCBM under 1 Sun conditions approaches a maximum value at high reverse bias, known as the saturated photocurrent ($J_{sat}$)[47]. Here, the photocurrent is completely controlled by light absorption as high internal fields prohibit both mono- and bimolecular recombination losses. While the drift/diffusion model approaches $J_{sat}$ under high reverse bias, the equivalent circuit model (parameters from Table 4.1) predicts the photocurrent to exceed $J_{sat}$ under high reverse bias. This occurs due to the light intensity dependence of $R_{shCT}$, which causes $R_{shL}$ to be lower under illumination than in the dark. This result offers an argument against treatment of CT state dissociation as a modified shunt resistance[14,132].

Even though reverse bias application is outside the range of power generation, this result is important when modeling BHJ devices with a strong field dependence of $P_{CT}$ and equivalently low $R_{shCT}$, such as polymer-

polymer and low-bandgap systems. On the other hand, blends not limited by monomolecular recombination with a weak $P_{CT}$ field dependence and high $R_{shCT}$, such as P3HT:PCBM[53] and other high performing systems[9,10], will cause the photocurrent to surpass $J_{sat}$ only at reverse biases approaching device breakdown.

## 4.5 $R_{sr}$ Case Study: $TiO_2$ as Electron Transporting Layer in BHJ Solar Cells

In order to demonstrate the usefulness of the observations of the previous section, a model system with significant $R_{sr}$ is presented to show the influence of $R_{sr}$ on device performance. Herein, inverted organic photovoltaic (iOPV) solar cells with amorphous titanium dioxide ($TiO_x$) and anatase $TiO_2$ as an electron transporting layer (ETL) are shown to have significant changes in $R_{sr}$ when illuminated with ultraviolet (UV) radiation. Use of ETLs is widespread in the literature[24] where $TiO_x$[28,140,141], $TiO_2$[114,142], ZnO[143], $V_2O_5$[144], and $Cs_2CO_3$[144] have been used. In particular, the UV sensitivity of $TiO_x$ has been studied and is known to affect iOPV device performance[24] but not in detail. Devices for this experiment were prepared using the standard methods presented in this thesis. $TiO_2$ sol-gel was synthesized by a previously reported method[29] and spincasted on ITO substrates and annealed at 150 °C for 1 hr in air to form amorphous $TiO_x$ films. For $TiO_2$ electron transporting layers, the spincasted film were annealed at 450 °C for 30 min in air.

### 4.5.1 Device Performance and UV Mechanism

Figure 4.15(a,b) shows that the dark ($J_{dark}$) and light ($J_{light}$) current densities in $TiO_x$ devices undergo considerable changes after 30 min time intervals of UV illumination. Clearly, the dark rectification, $J_{sc}$, and the FF are extremely poor prior to UV exposure leading to efficiencies well below 0.01%. Following consecutive UV illumination periods, performance steadily increases by more than two orders of magnitude and approaches saturation values. The UV response is somewhat sensitive to the $TiO_x$ thickness as shown in Fig. 4.15(c) where $J_{sc}$, $V_{oc}$, FF, and $R_{sr}$ are shown after each successive 30 min exposure to UV light. Longer exposure periods are needed to achieve saturation for thicker ETLs: $J_{sc}$ is saturated after 60 min and 120 min for devices with 25 nm and 50 nm of $TiO_x$, respectively. The change is most dramatic in $J_{sc}$, which increases from 0.07 to 8.3 mA/cm$^2$ after a 120 min UV exposure (25 nm $TiO_x$ device). The FF also improves from 15% to 51% yielding an efficiency of 2.8%. However, devices with $TiO_2$ as the ETL are relatively insensitive to even prolonged UV illumination where the efficiency is near its saturation value prior to UV exposure. In spite of the dramatic

changes observed in $J_{sc}$ and FF, Fig. 4.15(c) also indicates that $V_{oc}$ remains constant after each cycle of UV illumination. Furthermore, $R_{sr}$ undergoes a dramatic reduction of three orders of magnitude for devices with $TiO_x$ as the ETL.

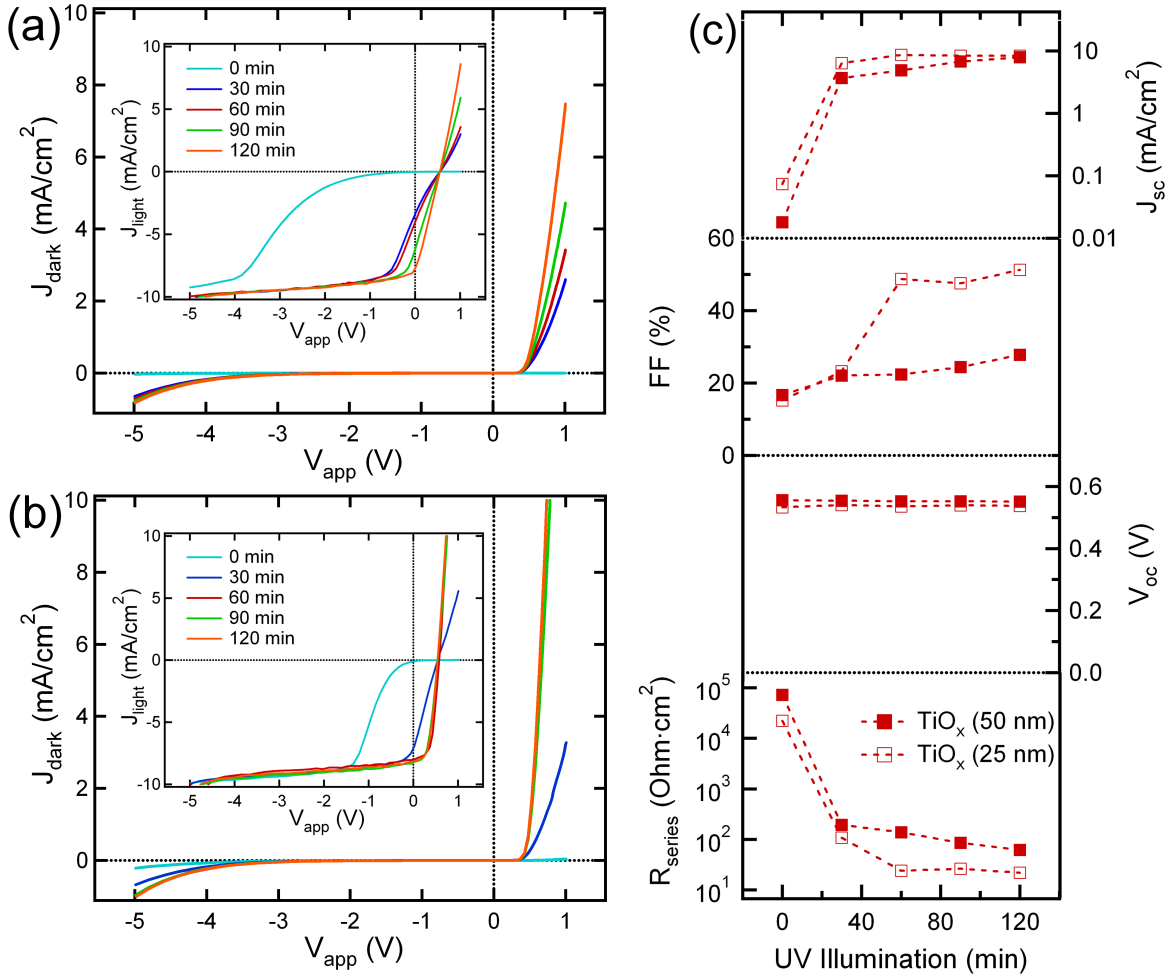


Figure 4.15: Dark current and light current (inset) densities for iOPV devices with (a) 50 nm and (b) 25 nm of $TiO_x$ as the ETL under solar simulated light (with a UV cut-off filter) after successive 30 min UV ($\lambda$ = 365 nm) exposure times. (c) Short-circuit current ($J_{sc}$), fill factor (FF), open-circuit voltage ($V_{oc}$), and series resistance ($R_{series}$) of devices with $TiO_x$ as the ETL after successive 30 min intervals of UV exposure.

Given that UV exposure does not have a significant influence on performance for devices with $TiO_2$ as the ETL, the change must reside in the $TiO_x$ layer itself. The electrical properties are characterized by measuring the dark resistivity after varying the UV illumination time for isolated layers in sandwich devices of ITO/$TiO_x$ or $TiO_2$/Al with the same dimensions as the iOPV devices. It is not shown here[33], but $TiO_x$ resistivity decreases by an order of magnitude (from 1.0 x $10^7$ to 1.2 x $10^6$ Ωcm), and approaches the resistivity of $TiO_2$ (which is almost unaffected by UV illumination). For simple metal-oxide diodes, changes in resistivity under both UV illumination and positive bias application have been attributed to an electrochemical mechanism that involves the filling of negatively charged oxygen traps in the metal-oxide[145]. The injection of free electrons and holes under

forward bias and the creation of electron/hole pairs during UV illumination separately result in a free electron left behind in the conduction band of the ETL causing an increase in the conductivity. Indeed, it was observed here that holding the device under positive bias for specified time intervals in the dark has the same effect on device performance as UV illumination [33].

### 4.5.2 $R_{sr}$ Model and Light Intensity

In order to understand how a resistivity change confined to the ETL influences the physical processes in the photoactive layer, the drift/diffusion model is applied using the modified $R_{sr}$ boundary condition (Eqn. 4.7). The measured changes in $TiO_x$ layer resistivity, in conjunction with the photoactive material's UV-independence, imply that UV exposure only affects the electrical transport properties of the ETL. Furthermore, the device $V_{oc}$ remains constant under UV illumination indicating that the ETL energy levels are unaffected [146]. Thus, the UV effect is modeled as a change in the effective potential difference across the photoactive layer leading to a weakening of the internal electric field. In this way, a UV-dependent serial resistance is incorporated into the model and used as a fitting parameter to approximate the current-voltage data in the first and forth quadrants. Series resistance values fall within 20% of the measured values in Fig. 4.15(c). Other model parameters describing P3HT:PCBM are taken as constant including the exciton generation rate determined from optical modeling (not shown) ($G$ = 6.75 x $10^{27}$), carrier mobilities, dielectric constant, and built-in voltage from above. The model simulations are shown in Fig. 4.16(a) where the trends of Fig. 4.15(c) for $V_{oc}$, $J_{sc}$, and FF are reproduced.

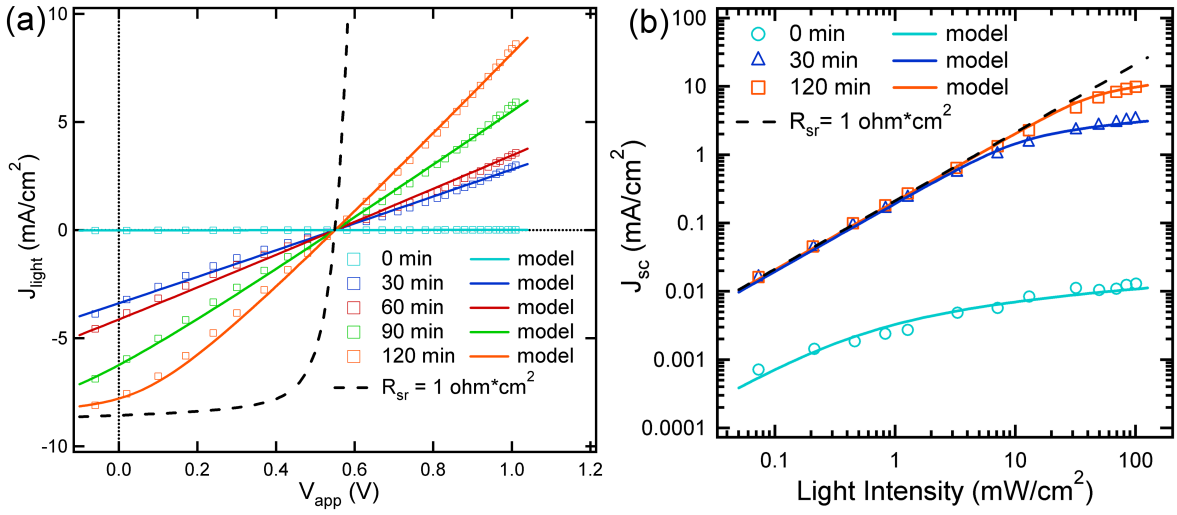


Figure 4.16: (a) Experimental and simulated light current density ($J_{light}$) for each cycle of UV illumination. (b) $J_{sc}$ as a function of $\lambda$ = 532 nm laser light intensity for a device with $TiO_x$ as the ETL prior to UV exposure and after 30 and 120 min exposure. With successive UV illumination and corresponding reductions in $R_{sr}$, the scaling of $J_{sr}$ with light intensity becomes more linear.

The significance of $B_{photo}$ in limiting $J_{photo}$ can be probed by measuring $J_{sc}$ over a range of light intensities where a non-linear dependence signals the prevalence of this process as described above. When measuring a device with high $R_{sr}$, this tendency is also expected. Due to the UV-controlled $R_{sr}$ observed here, the relationship between $J_{sc}$ and light intensity should become increasingly linear for prolonged UV illumination. This prediction is observed as shown in Fig. 4.16(b) where $J_{sc}$ is given as a function of light intensity under $\lambda = 532$ nm laser illumination. Sub-linear behavior is observed beginning below 1 mW/cm$^2$ for the 30 min UV illuminated device, and at higher intensity (above 1 mW/cm$^2$) for the device where the performance becomes UV saturated (120 min). Furthermore, it is found by fitting a power law relationship between 10 and 100 mW/cm$^2$, that the scaling exponent takes respective values of 0.38 and 0.73 for 30 min and 120 min of UV illumination. Regardless of UV exposure, $J_{sc}$ is increasingly affected by diode losses as the light intensity is increased as shown in the previous section.

As a final comment, it should be noted that the $R_{sr}$ model is not able to reproduce the s-shaped part of the J-V curves (negative bias) in Fig. 4.15(a,b). It is not shown here, but drift/diffusion models of a planar ETL with a high level of fix charge in Poisson's equation (Eqn. 4.5) (i.e. trap cites) is able to reproduce this part of the curve. However, the J-V curves above open-circuit do not match as well. Therefore, a combination model of trap cites and $R_{sr}$ is most likely the correct model to reproduce all the features of the experimental data. S-shaped J-V curves have been discussed elsewhere in the literature[54].

## 4.6 Conclusion

In conclusion, an electro-optical model for the operation of PC BHJ organic solar cells has been described. The model is applied to the test case of a 1-D periodic PC device and a conventional planar control cell with MDMO-PPV:PCBM as the photoactive BHJ material. The strong bimolecular recombination rates predicted for the PC cell limits performance compared to the planar cell even with enhanced optical absorption. In terms of the device model, this effect is due to the choice of boundary conditions and whether or not the electron transport layer is included. For all cases, electrical performance of PC cells is comparable to or worst than planar cells. Measurement of the light intensity dependence of the photocurrent should be undertaken to determine if the levels of space charge predicted by the model are correct. Finally, it is found that light intensity measurements of devices with non-ideal $R_{sr}$ and $R_{sh}$ obscure the scaling of $J_{sc}$ and $V_{oc}$ with light intensity, which is commonly tied to fundamental device physics like bimolecular recombination. This is shown to be the case for devices with

variable $R_{sr}$ where $TiO_x$ is used as an electron transporting layer.

# Chapter 5

# Free Carrier Transport

## 5.1 Introduction

In the electrical models of PC device performance shown in the previous chapter, significant bimolecular recombination was predicted due to the weakening of the electric field inside the nanostructures and relatively long transport paths out of the BHJ. The levels of recombination were dependent on both the device geometry and mobilities of electrons and holes. However, the maximum transport lengths of free carriers in BHJ devices should be confirmed. Due to the strong internal electric fields in BHJ devices, transport lengths have been traditionally characterized in terms of electron ($n$) and hole ($p$) drift lengths:

$$L_{n,p} = \mu_{n,p}\tau_{n,p}E \tag{5.1}$$

where $\mu_{n,p}$ is the carrier mobility, $\tau_{n,p}$ is the carrier lifetime, and $E$ is the internal electric field. Usually, $\mu_{n,p}$ is the desired quantity and can be measured under steady state with space charge limited current (SCLC)[71] and field effect transistor (FET)[70,147] techniques. The low mobility values determined from these methods compared to inorganic semiconductors has lead to the belief that active layer thicknesses of planar solar cells must be kept around 100 nm in order to reduce transport losses[9,29]. Given the different device geometries and measurement conditions for these methods, $\mu_{n,p}$ can span orders of magnitude depending on the technique due to its dependence on carrier density[148], polymer chain orientation[149], and whether or not the donor and acceptor are mixed or in pure phases[68,147]. In particular, for the standard BHJ material system, P3HT:PCBM, both $\mu_n > \mu_p$[68] and $\mu_n < \mu_p$[28,147] have been observed. Because these results depend on the technique and are conducted without illumination, it is difficult to guarantee that the derived transport lengths will appropriately describe the charge transport of photogenerated carriers in a working device. Contact barriers also play a critical

role for methods like SCLC where carriers are injected[150], which could be more effectively avoided by measuring photogenerated current that is extracted from the device[52]. While various transient techniques also exist that monitor the dynamics of charge transport[151], they can be more complex and intricate to implement than steady state measurements. Therefore, a simple steady state method would be advantageous to determine $L_{n,p}$ for photogenerated carriers in a working device under standard operating conditions.

In this chapter, $L_{n,p}$ are measured for solar cells under illumination. A novel method is demonstrated for P3HT:PCBM in order to compare these results with other transport measurements for this donor/acceptor system. By measuring the scaling of the photocurrent with light intensity over a range of applied voltages for different local exciton generation profiles ($G(z)$), $L_p$ = 90 nm in P3HT, while $L_n > 340$ nm in PCBM under standard annealing and preparation conditions. Electron and hole transport are probed independently by measuring both standard and inverted devices. Furthermore, a scaling exponent below that for the traditional space charge limited photocurrent (i.e. 0.75) is observed due to the dependence of charge transport on $G(z)$. The analysis is supported with an electro-optical model, which elucidates regions in the photoactive layer where free carrier loss occurs. Finally, the results clarify the reasons why thick active layers of P3HT:PCBM have lead to high device performance in the literature. They also help explain the predictions of space-charge in the PC electro-optical models in Chapter 4.



[152]**J.R. Tumbleston**, D.-H. Ko, E.T. Samulski, and R. Lopez *Analyzing local exciton generation profiles as a means to extract transport lengths in organic solar cells*, Phys. Rev. B 82, 205325 (2010).

## 5.2 Experiment

In order to compare transport of electrons and holes, both standard and inverted solar cells were fabricated. Schematics of these devices are shown in Fig. 5.1(a-b). Cleaned ITO-coated (150 nm; $\rho$ = 5E-4 $\Omega$ cm) glass substrates were coated with either PEDOT:PSS (55 nm; Baytron PH500) or sol-gel $TiO_x$[29] for standard and inverted devices, respectively. Standard device substrates were annealed in air at 140 °C for 10 min, while inverted substrates were heated in an oven at 450 °C for 60 min to convert $TiO_x$ to anatase $TiO_2$ (20 nm). Next, solutions of either P3HT (15 or 30 mg/mL) and PCBM (12 or 24 mg/mL) in a 1:0.8 ratio in chlorobenzene were spincoated at speeds ranging from 500 to 1300 RPM to achieve desired active layer thicknesses ($t$) between 80 and 390 nm. Finally, either Al (90 nm) or $WO_3$/Ag (10 nm/90 nm) were thermally evaporated as the back contact (12 $mm^2$

active area) for standard and inverted devices, respectively. Standard devices were annealed at 145 °C for 10 min after evaporation, while inverted devices received the same thermal treatment prior to electrode deposition.

Measurement under 1 Sun conditions was conducted in the glovebox, while the photocurrent under high incident angle (65°) was measured in air using a blue laser ($\lambda = 473$ nm). The photocurrent from the laser along with the incident light intensity ($P_{light}$) were measured simultaneously via a beam splitter on the optical set-up. No degradation occurred during device measurement time (< 3 hrs/device). Furthermore, significant reflection losses from the air/glass substrate interface were avoided by placing the glass substrate (side opposite active layer) in contact with a half-cylinder and index matching oil. This configuration prevented the incident beam from bending toward normal due to refraction in the glass substrate.

In spite of the differing electrodes, electron/hole transporting layer materials, and thermal treatment of ITO, both inverted and standard devices have similar performance under 1 Sun conditions for devices with $t = 130$ nm (thicker active layers will be discussed below). Short-circuit currents ($J_{sc}$) of 10.4 and 9.2 mA/cm$^2$, open-circuit voltages ($V_{oc}$) of 0.57 and 0.60 V, fill factors (FF) of 53 and 51%, efficiencies of 3.1 and 2.8%, series resistances (inverse slope at 0.75 V) of 8.8 and 9.3 Ω cm$^2$, and shunt resistances (inverse slope of dark current at 0.0 V) of 0.4 and 0.5 MΩ cm$^2$ were achieved for inverted and standard devices, respectively. Furthermore, atomic force microscopy (Fig. 5.1(c-f)) of the top surface of P3HT:PCBM spincast on both $TiO_2$ and PEDOT:PSS showed insignificant differences in film morphology. Based on these results, it is argued that changes in carrier transport in P3HT:PCBM related to morphology differences due to choice of electron/hole transporting layers are minimal compared to modification of the transport based on $G(z)$.

In this chapter, $G(z)$ ($z$ dependence dropped and implied for remainder of this work) is determined in the photoactive layer using the transfer matrix model introduced in Chapter 2, which has been used for both standard[31,66] and inverted devices[28,76,153]. Optical properties of each material layer are determined via spectroscopic ellipsometry, which closely match reported values in Chapter 3 and literature[31,33]. Layer thicknesses are measured with cross-section scanning electron microscopy and verified with profilometry and by fitting simulations of the spectral reflection to the measured reflection by varying layer thicknesses[111].

To model electrical performance, $G$ is used as input in the drift/diffusion effective medium model presented in the previous chapter. This metal/insulator/metal picture is a simplification of the studied devices where the transporting layers are disregarded along with any Schottky barriers. However, the similar $V_{oc}$ and series resistance for each device type indicates contacts that are comparable in function. Furthermore, the inclusion of slight barriers should not significantly affect carrier extraction especially for voltages below maximum power

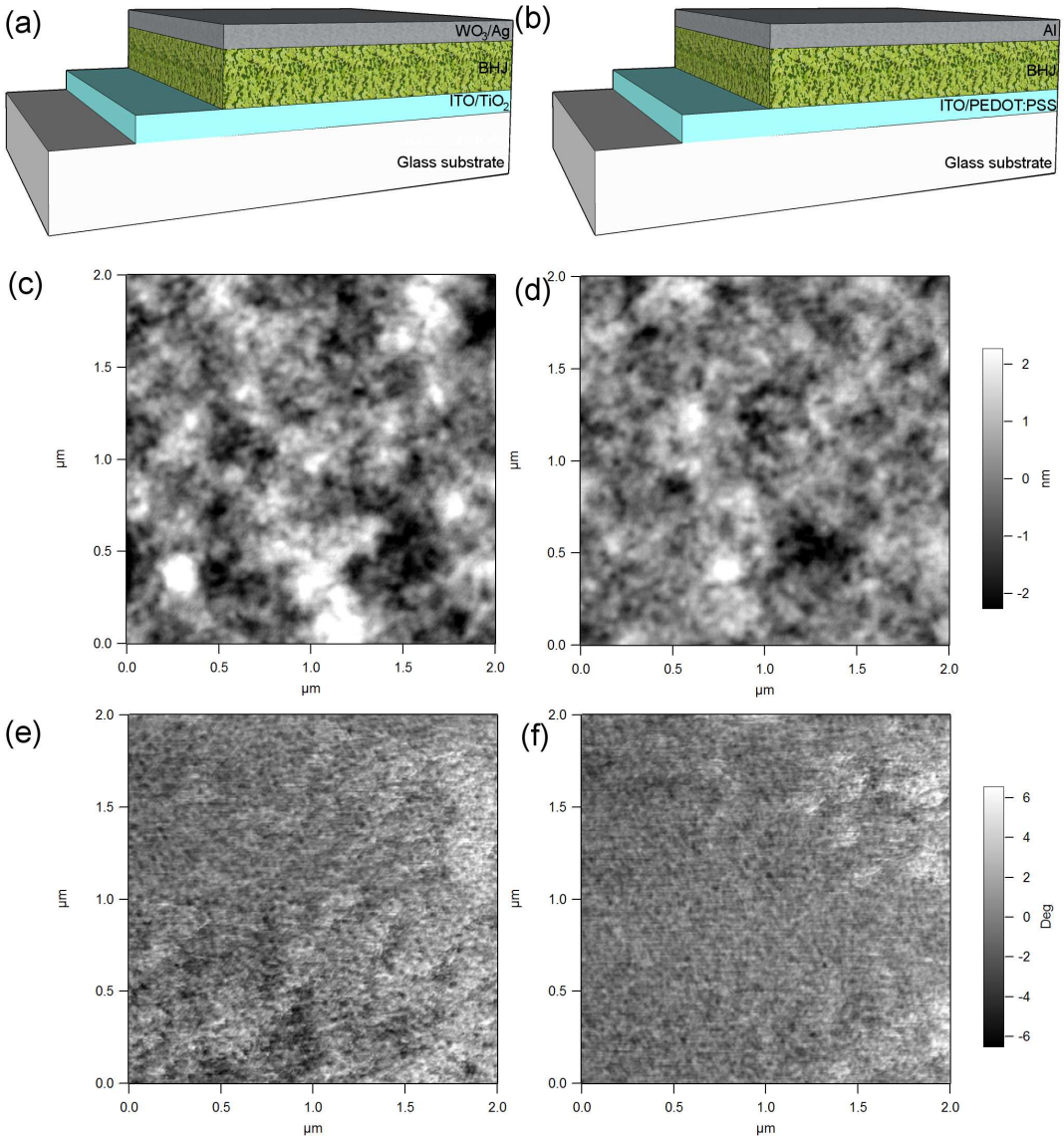


Figure 5.1: Schematics of (a) inverted and (b) standard BHJ devices. The active material is P3HT:PCBM. Atomic force microscopy topology (c,d) and phase (e,f) of top surface of P3HT:PCBM spincast on ITO/$TiO_2$ for the inverted device (c,e) and ITO/PEDOT:PSS for the standard device (d,f) with active layer thickness of 130 nm. Minimal differences are noted between inverted and standard devices, which support that they have similar active layer morphologies even though different transporting layers are used.

point where the conclusions from this work are drawn[154]. Besides $G$, other parameters in the electrical model are taken from literature for P3HT:PCBM[68] including $\mu_n$ (2.0 x $10^{-7}$ $m^2$/Vs), $\mu_p$ (1.0 x $10^{-8}$ $m^2$/Vs), relative dielectric constant (3.4), electron/hole pair separation distance (1.8 nm), exciton decay rate (2.0 x $10^4$ $s^{-1}$), and effective density of states (2.5 x $10^{25}$ $m^{-3}$). The parameter that dictates $V_{oc}$ in the model, the effective band gap (0.95 eV), is fit to the experimental data. Finally, the modified form of Langevin bimolecular recombination[120] is used to explicitly relate loss of carriers during transit to the slowest carrier species.

## 5.3 Comparing Standard and Inverted Devices

### 5.3.1 Exciton Generation Profile Sets Required Transport Distances

Even though multiple steps occur between exciton generation and carrier transport, it is assumed that the profile of free carrier generation essentially matches that of exciton generation due to the short (<20 nm)[37,155] diffusion length of photoexcited excitons to the donor/acceptor interface. Figure 5.2 shows $G$ for both inverted and standard solar cells with $t$ = 390 nm and $P_{light}$ = 10.0 and 10.9 mW/$cm^2$, respectively. Due to the high angle (65°) and relatively short excitation wavelength ($\lambda$ = 473 nm), an exponentially decreasing $G$ profile is set-up in the photoactive layer. Under these conditions, $G$ drops by three orders of magnitude from one side of the active layer to the other for both devices. This type of profile is very different from those under normal incidence for thinner active layers that vary by an order of magnitude where the maximum is centered in the middle of the active layer[58,66,76]. In this study, monotonically decreasing profiles are guaranteed even for thinner active layers due to the chosen incident angle and wavelength.

As shown in Fig. 5.2, the average hole has a much longer distance to travel than the average electron for the inverted device. The opposite is true for the standard solar cell. In this way, the average required transport distance for electrons and holes ($D_{n,p}$) are set simply by choosing inverted or standard devices with a specific $t$. For example, $D_n$ is defined for inverted devices by weighting $G$ by the distance ($z$) to the cathode:

$$D_n = \frac{\int_0^t (G)\,(z)\,dz}{\int_0^t (G)\,dz}. \tag{5.2}$$

$D_p$ is then given by $t - D_n$ where similar expressions are used to determine $D_{n,p}$ for standard devices. The incident wavelength essentially sets $D_{n,p}$ where $D_p$ = 310 and 230 nm for $\lambda$ = 473 and 600 nm, respectively, under normal incidence for the inverted device with $t$ = 390 nm. By increasing the incident angle to 65°, $D_p$ is

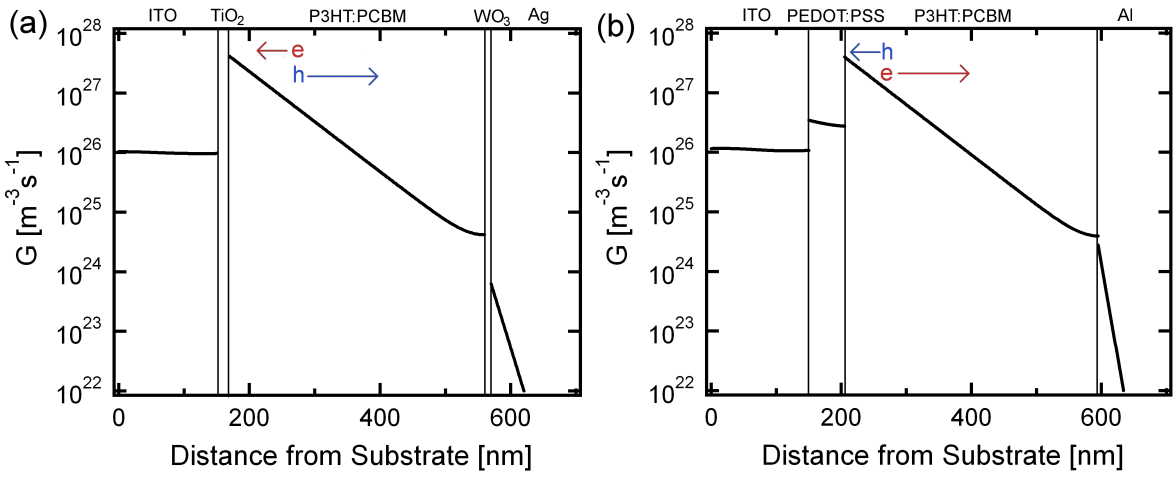


Figure 5.2: Local exciton generation profile ($G$) for (a) inverted and (b) standard device architectures with active layer thicknesses of 390 nm under 10.0 and 10.9 mW/cm$^2$ $\lambda$ = 473 nm (p-polarized) incident light intensity, respectively, at 65° incidence. $G$ represents the generation rate of excitons in the active layer, while it signifies parasitic absorption losses in all other materials. It is determined from an optical model and sets the average required transport distance for electrons and holes in the active layer depending on the device type. Arrows indicate the direction of electron and hole transport where the average hole is required to travel much further than the average electron for the inverted device. The opposite is true for the standard device.

lengthened to 340 and 250 nm for these wavelengths, respectively. Herein, a high angle (65°) and relatively short excitation wavelength ($\lambda$ = 473 nm) are used to set-up the longest possible values of $D_{n,p}$ for each $t$. In this chapter, $D_p$ is varied from 340 nm for inverted solar cells with $t$ = 390 nm down to 40 nm for standard devices with $t$ = 130 nm. A similar range is obtained for $D_n$. It should be noted that the incident light polarization also affects $G$ under non-normal incidence but has a negligible effect on $D_{n,p}$ values compared to the differences obtained by varying $t$. All work presented here is for p-polarized illumination as nearly identical results were obtained under s-polarization.

### 5.3.2 Photocurrent Scaling With Light Intensity

Determining if $D_{n,p}$ set by $G$ are too far for electrons or holes to travel is done by measuring the photocurrent ($J_{photo} = |J_{light} - J_{dark}|$) over a range of light intensities ($P_{light}$) and fitting to a power law relationship. Because $J_{photo}$ describes the current output solely due to photogeneration, the effects of series and shunt resistance that modify electrical performance under illumination are removed[131]. However, high series resistance can affect the power law scaling of $J_{photo}$ as shown in the previous chapter, but values measured herein range between 5 and 35 Ω cm$^2$, which are not high enough to have a significant impact.

Figure 5.3 shows $J_{photo}$ under various $P_{light}$ for both device types with $t$ = 390 nm. $J_{photo}$ is given over a range of reverse and forward applied voltages ($V_{app}$) up to $V_{oc}$ where the conclusions of this work are drawn from

voltages below maximum power point and into the reverse bias regime. It is clear that the shapes of the curves are very different for inverted and standard solar cells. For example, the inverted device requires high reverse bias application ($V_{app}$ = -5 V) in order to reach the saturated photocurrent ($J_{sat}$) under the highest $P_{light}$, while the standard device nearly saturates at short-circuit.

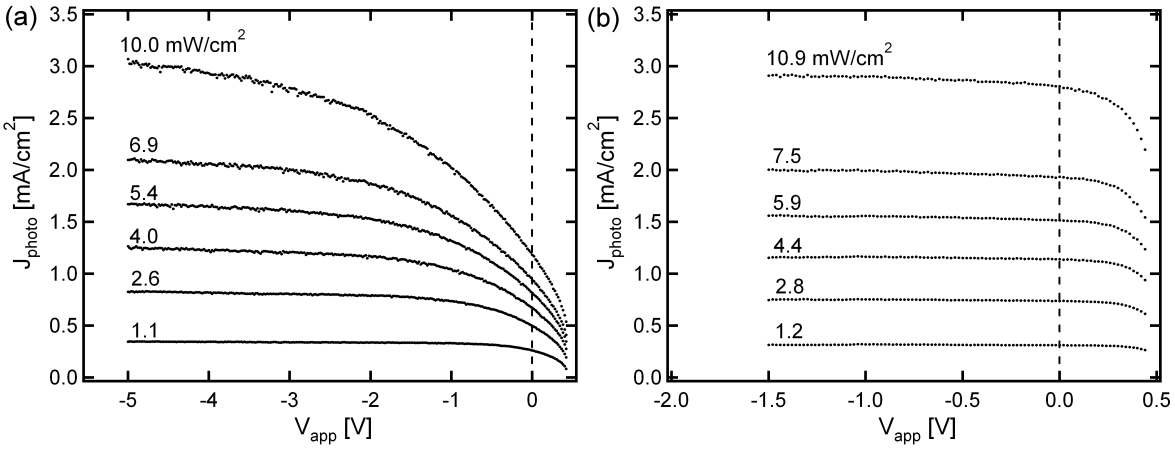


Figure 5.3: Photocurrent ($J_{photo} = |J_{light} - J_{dark}|$) over a range of applied voltages ($V_{app}$) for (a) inverted and (b) standard device architectures with active layer thicknesses of 390 nm under a range of $\lambda = 473$ nm laser light intensities ($P_{light}$) and 65° incidence. The inverted device requires high reverse bias in order for $J_{photo}$ to reach the saturated photocurrent for the highest $P_{light}$. Conversely, $J_{photo}$ for the standard device nearly saturates at short-circuit.

The cause of the different behaviors for inverted and standard devices can be further understood by determining the power law scaling of the photocurrent with light intensity ($P_{light}$):

$$J_{photo} = \beta \, (P_{light})^{\alpha} \tag{5.3}$$

where $\beta$ is a constant. By varying $P_{light}$, bimolecular recombination can be triggered due to its dependence on the product of electron and hole concentration [139]. Because this is the loss process of free carriers, linearity of $\alpha$ indicates the unrestricted, lossless transport of carriers to the electrodes. In this way, bimolecular recombination can be separated from other loss processes that reduce $J_{photo}$ below $J_{sat}$ and also depend on $V_{app}$, such as the electric field dependence of exciton dissociation [47]. Even though exciton dissociation also depends on $V_{app}$, it is monomolecular in nature and is accompanied by a linear scaling of $J_{photo}$ with $P_{light}$. It should be noted that bimolecular and other higher order recombination processes [156] are not distinguished here. Simply put, a nonlinear scaling of $J_{photo}$ with $P_{light}$ is interpreted as an indicator of loss of free carriers during transit that is labeled as bimolecular recombination. Also, the dependence of $\alpha$ on carrier density indicates that the number of free carriers must be similar for all devices in order to make accurate comparisons between the various device

configurations. This is confirmed from similar $J_{sat}$ values (Fig. 5.3) and from the optical model that indicates that the photoactive layer absorbs between 77% and 90% of the incident light for both standard and inverted devices regardless of $t$. Furthermore, $J_{sat}$ under the maximum $P_{light}$ from the laser is between 1/4 and 1/3 of the measured $J_{sat}$ under 1 Sun conditions. This sets the effective maximum sun-equivalent intensity of the laser to be between 1/4 and 1/3 Sun.

While $\alpha$ is usually only cited at short-circuit [56,131], it is determined here at each $V_{app}$ to show clear non-linear and linear regimes. Values are given in Fig. 5.4 for both inverted and standard devices with different active layer thicknesses ($80 \leq t \leq 390$ nm). It is observed for inverted devices that increasing $t$ causes $\alpha$ to deviate from unity for greater reverse bias application (i.e. higher internal electric fields). On the other hand, for standard devices with $t = 130$ and 390 nm, $\alpha$ remains close to unity over the entire voltage range. Under these illumination conditions with monotonically decreasing $G$, inverted devices suffer from recombination due to limited free carrier transport, while standard devices do not.

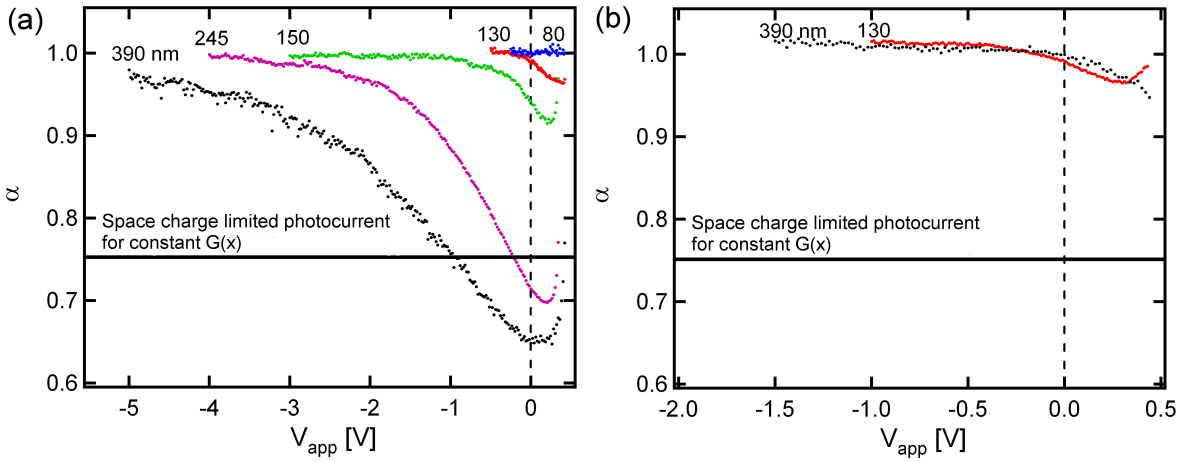


Figure 5.4: Scaling factors ($\alpha$) when the photocurrent is fit to a power law, $J_{photo} = \beta\,(P_{light})^{\alpha}$ for (a) inverted and (b) standard device architectures with various active layer thicknesses ($t$) under $\lambda = 473$ nm illumination and 65° incidence. Non-linearities are observed at higher reverse bias as $t$ is increased for inverted devices, while both thicknesses of standard devices show linear scaling. The case of space charge limited photocurrent for constant $G$ ($\alpha = 0.75$) is also shown for reference.

The contrasting transport between standard and inverted devices indicates that hole transport is limited for P3HT:PCBM under the prescribed preparation conditions for thicker values of $t$. For the thickest inverted solar cell ($t = 390$ nm), $D_p = 340$ nm, while $D_n = 50$ nm. A large negative $V_{app}$ (i.e. high electric field) is required to achieve $\alpha = 1.0$ where all the carriers are forced out of the active layer without recombining. However, as $t$ is reduced, the $V_{app}$ where $\alpha = 1.0$ moves toward the forward bias regime. For the $t = 130$ nm device, slight non-linearity is only observed near maximum power point, which means that $L_p > D_p$ even for the low electric

fields that approach open-circuit conditions. $D_p$ = 90 nm for the $t$ = 130 nm device, so it is determined that $L_p$ = 90 nm for P3HT. Conversely, $D_n$ is probed for the standard devices, where transport is not limited for even the largest $t$ as $\alpha$ remains close to unity even up to maximum power point. For the $t$ = 390 nm device $D_n$ = 340 nm, which is not long enough overcome $L_n$. Therefore, a lower limit of $L_n > 340$ nm is determined in PCBM for the annealed P3HT:PCBM system.

Another equally important observation from Fig. 5.4 is $\alpha$ values below 0.75 for the inverted devices with $t$ = 245 and 390 nm. It has been shown for solar cells where $\mu_n$ and $\mu_p$ differ by two orders of magnitude, space charge limited photocurrent occurs with $\alpha = 0.75$ [51]. However, this lower limit of $\alpha$ is achieved if $G$ can be approximated as constant in the active layer. For the $t$ = 390 nm inverted device, $G$ varies by three orders of magnitude (Fig. 5.2(a)). This imposes the average hole to travel much further ($D_p$ = 340 nm) than under a constant generation profile ($D_p = t/2$ = 195 nm). Thus, there appears to be a significant impact of $G$ on $\alpha$ reaching values at or below 0.75. This signifies that severely unbalanced transport and space charge limited photocurrent can be strongly influenced by $G$ along with $\mu_{n,p}$ values. In terms of the scaling of $J_{photo}$ with $V_{app}$ a power dependence of 0.45 for -2.0 $\leq V_{app} \leq$ 0 is determined for the inverted device under highest $P_{light}$. This type of voltage scaling is also indicative of space charge limiting behavior, especially when observed under reverse bias away from open circuit. No such behavior is observed for the standard devices.

Finally, the effect of bimolecular recombination on inverted device performance is also observed in device fill factor (FF). Figure 5.5 shows the FF for light intensities used to determine $\alpha$ from Fig. 5.4. It is evident that as $t$ increases, the FF drops accordingly. For standard devices (not shown), the FF values are similar to those for the $t$ = 80 nm inverted device. Because $R_{sr}$ is similar for all devices and monomolecular recombination only plays a minor role as observed above, the reduction in FF attributed to thicker $t$ is related to enhancement in bimolecular recombination due to the increase in $D_p$ imposed by $G$.

### 5.3.3 Interplay Between Local Exciton Generation and Recombination

While the macroscopic description of charge transport is given by measurement of $L_{n,p}$, further insight can be gained with a model that describes the local profile of recombination in P3HT:PCBM. While various models have been proposed that assume identical carrier transport between electrons and holes [136,157], the drift/diffusion model allows for unbalanced charge transport and non-constant $G$ [65]. In this model, transport is described using $\mu_{n,p}$, where $\mu_n = 20\mu_p$ [68] given the result that $L_n > L_p$. It should also be noted that $\mu_{n,p}$ are taken to be constant throughout the active layer to reflect bulk measurements of $L_{n,p}$ even though charge transport can vary

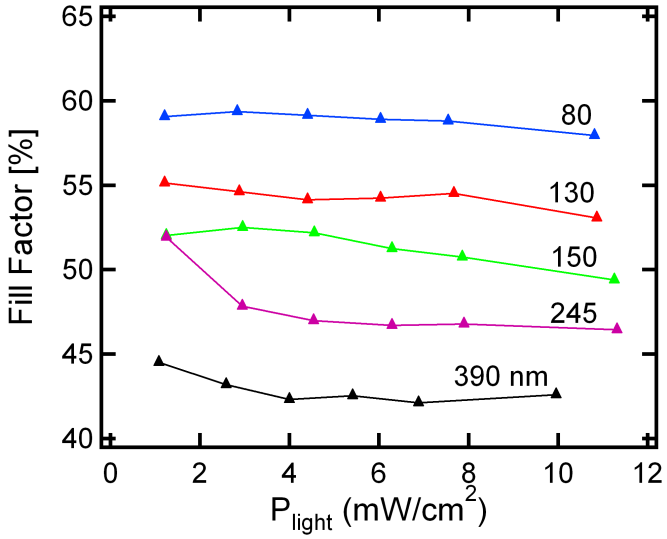


Figure 5.5: Fill factor (FF) for inverted devices with varying active layer thickness ($t$) as measured from the data for Fig. 5.4(a). The FF for standard devices (not shown) is similar to that of the $t$ = 80 nm inverted device indicating that the longer transport distance set by the exciton generation profile for thicker photoactive layers can greatly reduce the FF.

on the microscale for BHJ solar cells[41].

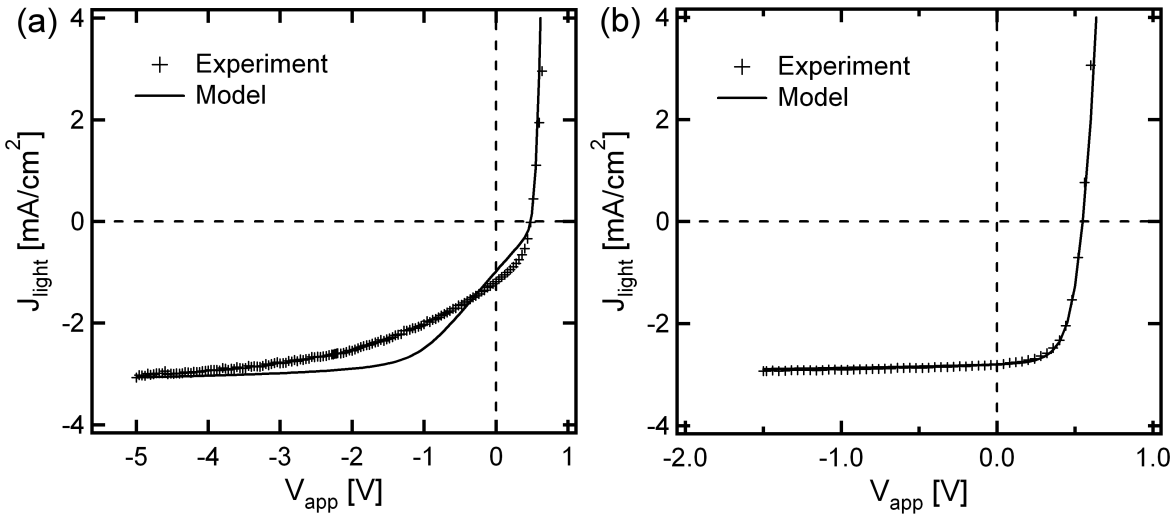


Figure 5.6: Experimental and modeled current density under illumination ($J_{light}$) vs. applied voltage ($V_{app}$) for (a) inverted and (b) standard devices with active layer thicknesses of 390 nm under the illumination conditions for Fig. 5.2. Simulations are generated by inputting $G$ from Fig. 5.2 in the drift/diffusion model of the active layer with an electron and hole mobility ($\mu_{n,p}$) mismatch ($\mu_n = 20\mu_p$) to represent the shorter hole than electron transport length ($L_n > L_p$).

Figure 5.6 shows the measured current density under illumination ($J_{light}$) for the inverted and standard devices with $t$ = 390 nm under laser illumination with $P_{light}$ = 10.0 and 10.9 mW/cm$^2$, respectively. When the generation profiles of Fig. 5.2 are input in the model keeping all other parameters constant, very different behavior is predicted for standard and inverted devices. Compared to the standard device, the inverted solar cell has a much lower $J_{sc}$ and FF, which matches the trends of the experimental data. Saturation of $J_{light}$ is also

observed to occur under high reverse bias conditions, while it saturates near short-circuit for the standard solar cell. The saturation voltages of $J_{light}$ also qualitatively match those for both $J_{photo}$ and $\alpha$ of Fig. 5.3 and Fig. 5.4, respectively.

The utility of the model can now be realized by calculating the net generation rate ($U$)[65] of free carriers for both inverted and standard devices at short-circuit ($t = 390$ nm). Figure 5.7(a) shows that for the inverted device $U$ is reduced near the cathode by orders of magnitude due to bimolecular recombination. This ultimately leads to a reduction in photocurrent extraction (Fig. 5.6), because the majority of the slower carrier species (i.e. holes) need to transport much further than $L_p$ resulting in a build-up of space charge and reduction in the internal field near the cathode. On the other hand, for the standard device, $U$ essentially matches $G$ of Fig. 5.2 which indicates minimal recombination. Even though the active layer is very thick, high extracted current is achieved, because both $D_p < L_p$ and $D_n < L_n$ are satisfied for the standard device.

This intuitive picture is further exemplified by calculating the fraction of carriers that undergo bimolecular recombination $R_{fraction}$ for both devices (Fig. 5.7(b)). It is noted that the strength of recombination is more significant in areas of the active layer where holes have a further distance to travel. This is especially true for the inverted device where most of the carriers are created far from the anode as set by $G$ (Fig. 5.2(a)). However, even for the standard device where few carriers are created far from the anode (Fig. 5.2(b)), there is still significant recombination in this region of the active layer.

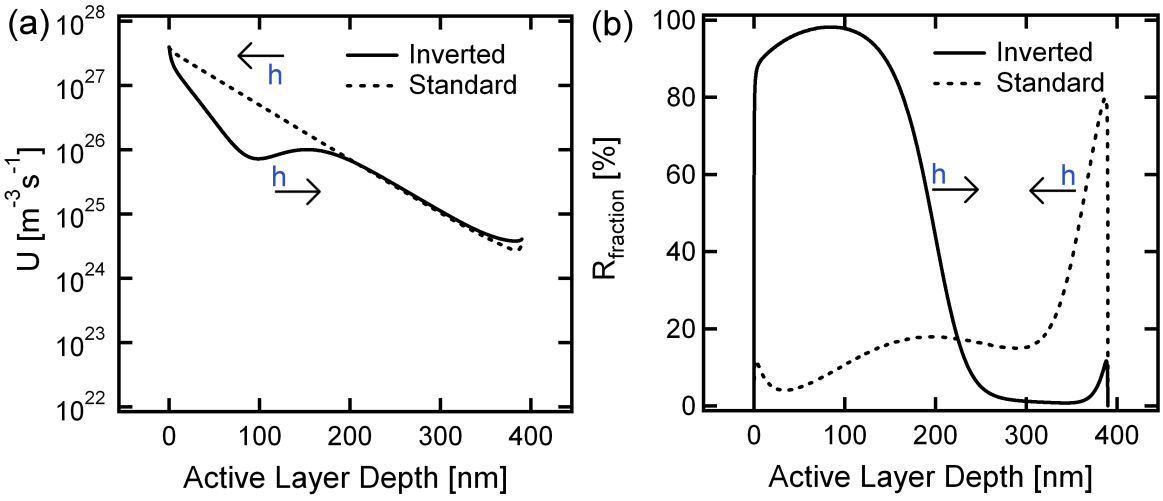


Figure 5.7: (a) Net generation rate ($U$) and (b) fraction of carriers that undergo bimolecular recombination ($R_{fraction}$) at short-circuit for both inverted and standard devices with active layer thicknesses of 390 nm as modeled in Fig. 5.6. Arrows indicate opposite direction of hole transport for inverted and standard solar cells.

### 5.3.4 Implications for 1 Sun Operation

Even though the non-constant $G$ profiles (Fig. 5.2) in this chapter are useful in determining $L_n$ and $L_p$, they are different from the generation profiles under 1 Sun conditions at normal incidence. In this section, device performance using the exact 1 Sun $G$ and average value of the 1 Sun exciton generation rate ($\langle G \rangle$) are modeled and compared for both standard and inverted solar cells as a function of $t$. Figure 5.8 shows the ratio of $J_{sc}$ values predicted from the model using $G$ compared to those using $\langle G \rangle$ under 1 Sun illumination and normal incidence. It should be noted that $G$ is determined for 1 Sun illumination by integrating all $G$ profiles over the spectral range where P3HT:PCBM absorbs light ($350 \leq \lambda \leq 675$) using the wavelength dependent light intensities from the AM 1.5 spectrum. It is clear that up to $t = 180$ nm, there is little difference in $J_{sc}$, which indicates minimal recombination losses. However, as the active layer is increased, $J_{sc}$ computed from $G$ is larger than that using $\langle G \rangle$ for standard devices. This occurs because $\langle G \rangle$ creates more holes further from the anode causing an increase in recombination and drop in output current. The opposite is true for the inverted devices where use of $G$ results in a smaller $J_{sc}$ compared to use of $\langle G \rangle$. For this case, $\langle G \rangle$ creates more holes closer to the anode and effectively assists in charge transport. This result agrees well with the previous determination of $L_{n,p}$ where a device thickness above $2L_p$ begins to show significant signs of recombination losses. However, for standard devices, $t$ can be increased beyond $2L_p$ due to the non-constant $G$ that creates more carriers closer to the anode, which ultimately assists hole transport.

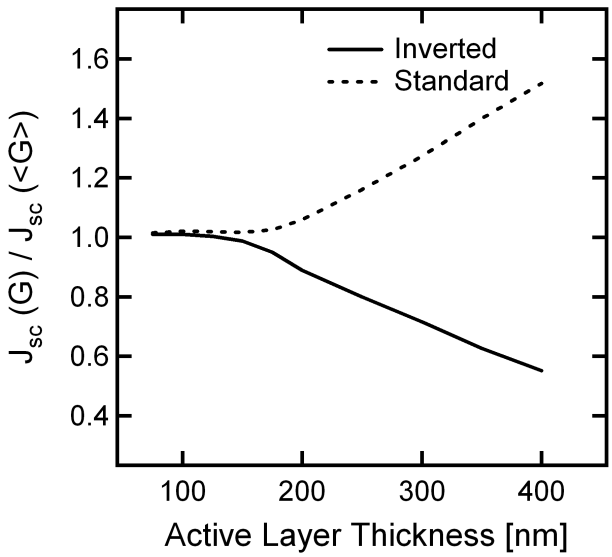


Figure 5.8: Ratio of short-circuit current ($J_{sc}$) using exact exciton generation profile under 1 Sun illumination and normal incidence ($G$) compared to the average profile ($\langle G \rangle$) for inverted and standard devices as a function of active layer thickness.

In terms of 1 Sun performance, this work supports that of others who have shown high performance for standard P3HT:PCBM solar cells with $t \geq 350$ nm as mentioned in Chapter 1[56,158]. For active layers of this thickness, $L_n > L_p$ actually assists device performance and allows for thicker active layers to be used, because carrier creation is weighted more heavily toward the anode. In this work, standard devices with $t = 390$ nm achieved 1 Sun efficiencies of 3.5%, which is higher than those with $t = 130$ nm (2.8%). The higher efficiency is due entirely to higher $J_{sc}$ from enhanced light absorption as $V_{oc}$ (0.59 V) and FF (52%) are similar. On the other hand, $L_n > L_p$ proves detrimental to thicker inverted device performance where the efficiency for $t = 390$ nm devices remains near 1% due to reduced $FF$ (43%) and $J_{sc}$ (5.2 mA/cm$^2$). However, $\mu_n < \mu_p$ has also been observed when doctor blading the active layer from ortho-xylene[28], which would then assist inverted device performance by making $L_n < L_p$. Either way, $L_n \neq L_p$ can actually allow for the use of thicker active layers ($t > 200$ nm) to absorb more light without significant transport losses. This is especially true for BHJ blends like P3HT:PCBM that do not suffer from monomolecular recombination losses that may become more significant as $t$ increases like MDMO-PPV:PCBM[31].

## 5.4 Observation of $L_n > L_p$ in Single Device

In the section above, it was demonstrated that $L_n > L_p$ by measuring standard and inverted device architectures. In this section, the same result is obtained by measuring a single standard device with thin Al electrode. Enough light can be transmitted through a 10 nm thick Al layer, so that the device can be illuminated from the back side. Even with this thin layer, $R_{sr}$ is low enough to escape the nonlinear dependence of $J_{photo}$ on $P_{light}$ with high $R_{sr}$ as described in the previous chapter. The results below are for two devices, one with 90 nm and another with 225 nm active layer thicknesses.

### 5.4.1 Optical Profiles When Illuminating From Different Sides

Figure 5.9 shows the normalized exciton generation rates in P3HT:PCBM when illuminating from the ITO and Al sides of the device under normal incidence using $\lambda = 473$ nm. For the $t = 90$ nm device, $D_n$ and $D_p$ are approximately equal regardless of illumination direction. This is not the case for the 225 nm active layer where $D_n = 160$ nm and $D_p = 160$ when illuminating from the ITO and Al sides, respectively.

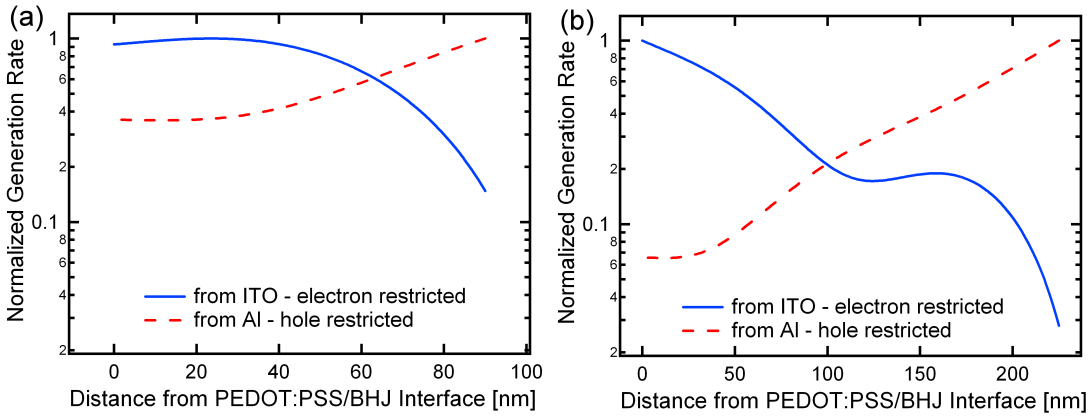


Figure 5.9: Normalized exciton generation rates for (a) 90 nm and (b) 225 nm active layer thicknesses. The profiles for the 225 nm thick device offer enough attenuation to result in long $D_n$ (illuminated from ITO) and $D_p$ (illuminated from Al) values to probe carrier transport.

### 5.4.2 Same Trend for Single Device: Restricted Hole Transport

Figure 5.10 shows the photocurrents under different $P_{light}$ for the $t = 225$ device. At negative bias, the photocurrent saturates to $J_{sat}$ and provides a measure of the number of carriers generated for each light intensity. The intensity of the laser is varied by an appropriate amount in order to guarantee that the photocurrents are equal before the scaling exponent, $\alpha$, is determined. When illuminating from the Al side, a significant amount of light is either reflected or absorbed, because ~2.7 times higher light intensity is required to generate the same number of carriers as when illuminated from the ITO side. The plots also indicate that a higher electric field (i.e. higher reverse bias) is required in order for the curves to saturate.

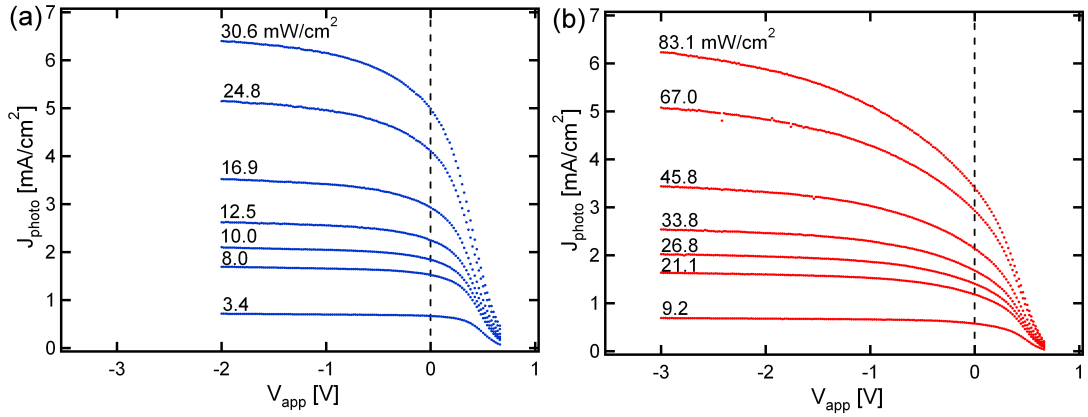


Figure 5.10: Photocurrent under different illumination intensities a normal incidence with the $\lambda = 473$ nm laser when illuminated from the (a) ITO and (b) Al side of the device. Even though the Al electrode absorbs or reflects a significant fraction of the light, photocurrents near 1 Sun values are still capable of being produced. It appears that when illuminated from the ITO side, more applied voltage is required in order for the photocurrent to saturate.

A final step is to determine the scaling exponent, $\alpha$, for both active layer thicknesses when illuminating from

different sides. For the 90 nm thick active layer, $\alpha$ is close to unity regardless of the illumination direction. This indicates that carrier transport is unrestricted for the $D_{n,p}$ values for this $t$. On the other hand, for the $t = 225$ nm device, the transport is more restricted when illuminating from the Al side compared to the ITO side. This result agrees with the previous result for the standard and inverted devices in the previous section where it was found that $L_n > L_p$. The values of $D_p$ imposed by the optical model cause holes to be generated further than they can are capable of traveling. This leads to the recombination of charge carriers.

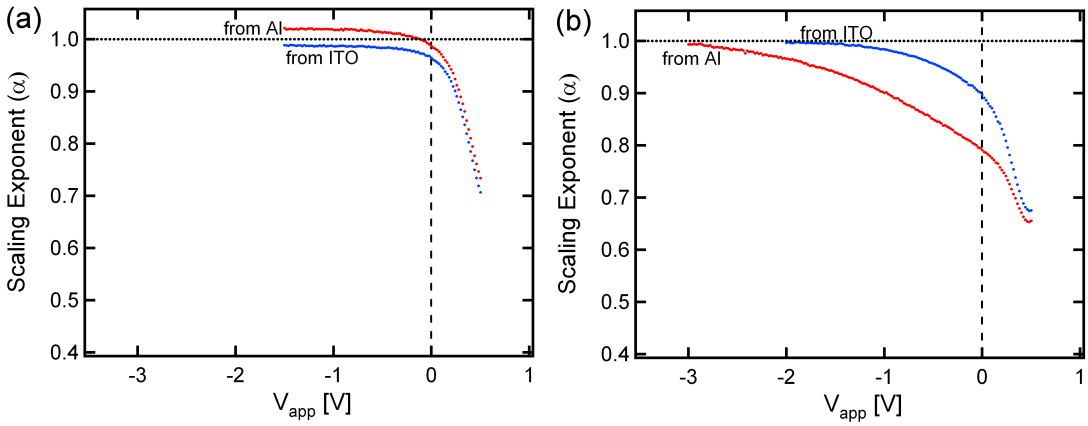


Figure 5.11: Scaling exponent $\alpha$ for a (a) 90 nm and (b) 225 nm active layer thicknesses. Greater recombination is noted for generation profiles that require holes to transport a long distance. Ultimately, it is found that $L_n > L_p$ as was found in the previous section for the experiment with standard and inverted solar cells.

## 5.5 Conclusions

In summary, a simple method has been developed to extract $L_{n,p}$ for functional solar cells by measuring the scaling of the photocurrent with light intensity over a range of applied voltages for different exciton generation profiles. For annealed P3HT:PCBM, it is observed that hole transport is much more restricted than electron transport, which actually assists device performance for P3HT:PCBM standard solar cells with thicker active layers. For inverted devices, transport is severely limited and results in a scaling exponent below that for the traditional space charge limited photocurrent with a constant generation profile. The analysis is supported with an electro-optical model, which indicates that the slower carrier suffers significant recombination far away from its final destination (holes from the anode in this case). Ultimately, these results support the premise that thicker active layers could be used to absorb more light for BHJ systems where $L_n \neq L_p$. As a double check of the work on standard and inverted devices, similar results are obtained for a single standard device with thin Al electrode. By shining light from different sides of the active layer, electron and hole transport can be separately probed where it is also found that $L_n > L_p$.

The results of this chapter indicate that holes are the slower carrier for annealed P3HT:PCBM devices and have an average transport length of ∼100 nm. This agrees with the electrical models of PC cells presented in Chapter 4, where the build-up of space charge is evident for PC cells, depending on carrier mobilities. Furthermore, the transport length mismatch between electrons and holes for P3HT:PCBM helps explain why standard devices with active layers much thicker than 100 nm have high PCE, as discussed in Chapter 1. These measurements should be done on other high-performing blends like PCDTBT:$PC_{70}BM$ that have low levels of monomolecular recombination but still have optimized active layers with thicknesses below 100 nm. Most likely, free carrier transport is a critical process that limits the possibility to make active layers thicker in these devices to absorb more light.

# Chapter 6

# Conclusions and Outlook

## 6.1 Why This Thesis is Important

In this thesis, the groundwork has been laid for a new type of organic solar cell geometry, those with photonic crystal (PC) photoactive layers. This method is fundamentally different from other light management approaches that utilize ray or wave optics. For ray optics approaches including microprism substrates[93] and V-folded substrates[94], light sees the photoactive layer as a flat layer, because the substrates are textured on a scale much larger than the wavelength of light. Furthermore, many wave optics approaches incorporate planar photoactive layers, including optical spacer configurations[27,29], that control light absorption through thin film interference. However, the photoactive layer of PC solar cells is comprised of periodic nanostructures on the order of the wavelength of light. This is also the case for diffraction grating[61,62,97] and surface plasmon[99] approaches, but instead of being interfaced with a metal, the nanostructures in the PC design are interfaced with a low index of refraction material that provides optical contrast. This contrast allows for the coupling of resonant or quasiguided modes that is a unique effect in trapping light in organic solar cells.

Development of this new cell design has offered many contributions to the field of light trapping in OPV. Most notably is the first measurement of resonant modes in both angular-dependent device reflection and IPCE. Calculation of the optical redistribution of light in PC cells along with photonic band diagrams offers a complete picture of resonant mode excitation. These methods should serve as guidelines to characterize wavelength-specific enhancements for future light trapping schemes, PC or otherwise. In terms of device fabrication, P.R.I.N.T. has been demonstrated to be a successful method to fabricate periodic nanostructures that could be easily extended to make nanopatterned substrates or active layers for other light trapping approaches[61,93,97,99,115].

Development of an accurate optical model for PC cells in this thesis extends previous models for planar OPV

devices[25,26]. When coupled with the extension of the standard electrical model[65] from one dimension to higher dimensions, a complete electro-optical model for PC cells is now available. This model can now be applied to other light trapping approaches comprised of periodic nanostructures.

While working to understand the impact of the PC geometry on electrical processes, a better description of device performance was first required for planar cells than what was available. Foremost, knowledge of the impact of carrier transport layers on device performance was needed. An important contribution of this thesis is how these layers can affect parasitic device resistances. While they have been known to greatly affect device performance[53], it was not understood how they influence fundamental physical processes in the photoactive layer including exciton dissociation and charge transport. Having this newfound understanding allowed for the analysis of a standard OPV system with $TiO_x$ as an electron transporting layer.

A final contribution of this thesis is a simple method to measure the transport length of electrons and holes in BHJ devices. While field effect transistor (FET) and space charge limited current (SCLC) diode methods have been widely used before, they each have negative aspects. FET measurements are parallel to the plane of the film, while both involve injecting charge from the contacts in the dark. However, carriers in working solar cells transport perpendicular to the plane of the film and are extracted due to photogeneration under illumination. Using this method, hole transport was shown to be restricted relative to electron transport for P3HT:PCBM solar cells. The short transport length of holes is consistent with the electro-optical model of PC cells where there is prediction of free carrier transport losses in the relatively thick post structures. Furthermore, these measurements helped resolve the question why the most efficient P3HT:PCBM solar cells have very thick active layers[7,56].

## 6.2 Looking Forward

### 6.2.1 Device Physics

In conjunction with a more thorough understanding of fundamental physics, device performance of OPV solar cells will continue to progress. All models of BHJ performance indicate that the barrier of 10% can be broken[13–15] with a combination of the right light absorption properties, layer morphology, choice of electrodes and interface materials, and carrier extraction. The goal of high performance will be guided by a more thorough and detailed description of electro-optical processes in these solar cells.

Recently, there has been a flourish of progress in the understanding of BHJ device function. Most notably, there is currently an extensive debate on the voltage dependence of the photocurrent in BHJ solar cells. It is

universally accepted that the photocurrent goes to zero near $V_{oc}$ and saturates at negative voltages to a value proportional to light absorption. Recent work has shown that losses are both monomolecular and bimolecular in nature[159], however the precise physical mechanisms are still being explored[69,160–162] along with the exact shape of the photocurrent near open-circuit conditions[157,163].

Even though the precise mechanisms are still being resolved, the field dependence of the photocurrent is widely accepted. Application of larger electric fields inevitably extracts more photocurrent. This has led to exciting advances in device design to enhance the internal field to improve photocurrent extraction[164,165]. Novel techniques to enhance the electric field may continue to be demonstrated in the future as a route to boost OPV performance.

Finally, greater understanding of fundamental physics has also led to the introduction of new device models. Many variations of drift/diffusion[54,59,65,129], equivalent circuit[53], Monte Carlo[126,166,167], and analytic[168] models have been presented to predict device performance. While they have all achieved significant success, work needs to be done to show the links and transitions from one model to the next. Monte Carlo models capture the microscopic structure of the BHJ and are the closest to a first-principles calculation. It is still not clear what assumptions are required to justify using drift/diffusion models that disregard the microscale structure. Likewise, the assumptions needed to move from numerical drift/diffusion to analytic models are not completely resolved. Because these models use different parameters, a thorough study of the link between different parameter sets that predict identical J-V curves would be very insightful. Work should be done to unify these modes of description into a more complete model of device performance.

### 6.2.2 Synthesis of the Ideal Donor/Acceptor System

Figure 6.1 shows the theoretical limit of $J_{sc}$, $V_{oc}$, and PCE for a single bandgap solar cell under standard AM 1.5 operating conditions as a function of bandgap. This is known as the Shockley-Queisser limit[169]. A tradeoff exists between $J_{sc}$ and $V_{oc}$, where a maximum efficiency above 30% is possible for a bandgap of ∼1.4 eV. While this is the limit assuming no optical or electrical losses, it is helpful to understand the weakest link of BHJ solar cells that has kept their PCE below 10%. Because a significant amount of energy is lost during electron transfer from the donor to acceptor (1 eV for P3HT:PCBM), $V_{oc}$ is much lower than what is predicted in the theoretical limit. If the exciton could be split in P3HT without the use of PCBM as an acceptor, then $V_{oc}$ would have a theoretical limit of 1.7 V for P3HT's bandgap of 2.1 eV. This is almost three times higher that what is achieved in experiment for P3HT:PCBM ($V_{oc}$ = 0.6 V). Even when paired with PCBM, a loss of 1 eV

upon electron transfer is much more than is required to separate the electron and hole (~0.3 eV). Tailoring the energy levels to reduce this loss has already significantly enhanced device performance and raised efficiency levels above the level of 7%[10]. This will continue to be a significant area of research until the ideal donor/acceptor system is found with optimal energy levels, light absorption, and carrier extraction. While silicon remains king of inorganic solar cells, the equivalent material system in the field of BHJ devices has yet to be synthesized.

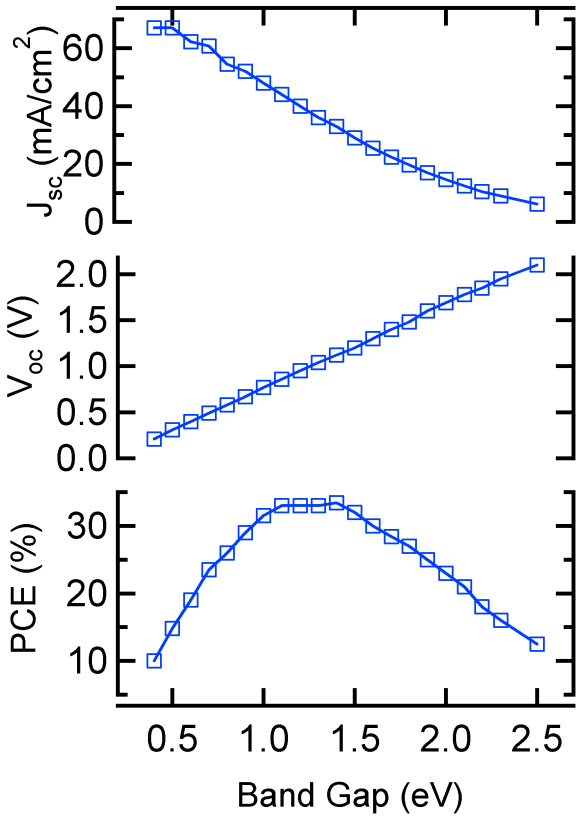


Figure 6.1: Theoretical limit for single bandgap solar cell as function of bandgap energy. A tradeoff exists between $J_{sc}$ and $V_{oc}$, making a gap of 1.4 eV optimal for the AM 1.5 solar spectrum.

### 6.2.3 Nanostructures and Light Trapping

While synthetic chemists continue to search for the perfect donor/acceptor system, approaches to enhance efficiency that rely on nano-engineering will further develop. Recently, light absorption enhancement factors of 100 times for extremely thin samples have been predicted[75]. Attempts to fabricate this type of nanostructure, which has multiple length scales, using simple methods over large areas will continue so long as these types of enhancements are possible. Thin active layers are also desirable from the standpoint of material cost, where less material is used for thinner active layers. However, this must be weighed against the added complexity of fabricating nanostructures.

Ultimately, the future of light trapping techniques in solar applications remains uncertain. These techniques will always involve structures in the submicron regime in order for light to be manipulated. However, in order for photovoltaics to become a significant player as an energy converter, hundreds of square kilometers of land must be covered to absorb light from the sun. This leads to an astronomical number of total nanostructures. Therefore, developing extremely simple fabrication methods is mandatory for light trapping techniques to become truly relevant in the field of photovoltaics. This is especially true for OPV where the driving force behind their development is their reduced cost compared to inorganic solar cells. Each additional step in fabrication (e.g. to make nanostructures for light trapping) will add to the complexity of device processing and ultimately to the cost.

The P.R.I.N.T. method used in this thesis has the potential to be a simple, large scale method to generate nanostructures in roll-to-roll fashion. However, as reviewed at the end of Chapter 3, there are still issues when the PFPE mold is contacted with a BHJ thin film. An immediate goal is to determine if the contact changes the morphology or if contamination occurs either by leaving behind PFPE or unwanted particles. Recent progress has also been made using more controlled techniques for making nanostructures. So-called solvent assisted patterning techniques that use Si master molds[50] may be an alternative to embossing methods like P.R.I.N.T. However, such methods come with added complications and a greater challenge to upscale to roll-to-roll fabrication.

Issues with patterning photoactive materials directly can be immediately circumvented by nanostructuring an inorganic layer of the solar cell that is more robust to cleaning and sonication. Recent progress has been made in patterning ITO[115], but the device efficiency is still not to the level of the best planar cells. Even with years of attempts to enhance the absolute performance of P3HT:PCBM devices above the level of 4.4% published in 2005 for a simple planar device[7], no method involving nanostructures has shown a PCE above this level.

Therefore, a path in nanopatterning research is unlikely to involve P3HT:PCBM as an active material where the PCE has already been maximized. There is greater hope for light trapping near the band edge of materials that have very long band tails. This is the case for amorphous silicon (a-Si) where a high population of resonant modes can be excited[80]. Also, the number of excitable modes scales with the flash layer thickness, which is typically a few microns for a-Si cells but less that 100 nm for PC organic solar cells. Future research in OPV light trapping should involve low-bandgap polymers that absorb more weakly than P3HT and are more similar to a-Si in their absorption properties. This could result in light trapping approaches having a greater impact in improving BHJ device performance to levels of 10%. The fabrication methods, characterization techniques, and electro-optical modeling developed as part of this thesis should set the stage for these developments.

# Appendix A

# Accuracy of Research Tools

The accuracy of a few research tools used in this thesis are given below.

## A.1 Optical Modeling Program

All optical simulations in this thesis have been done using code written in *Mathematica* following the procedure outlined by Tikhodeev et al.[84]. In their publication, the transmission of light in a model photonic crystal slab system (Fig. A.1(c)) is calculated. The dark grey square posts have an index of refraction of 1.99, while the light grey substrate and medium surrounding the posts have index of 1.44. Both materials are taken to be transparent. The periodicity, $d$, is 680 nm, while the post height, $L_z$, is 120 nm. Figure A.1(b) shows the calculation of the zeroth order transmission from Tikhodeev et al. under normal incidence illumination. Figure A.1(a) shows that the same result is obtained using the *Mathematica* program and demonstrates its accuracy compared to literature.

It is not shown here, but the same result was obtained in *RSoft DiffractMOD*, a commercially available optical simulation package. Furthermore, agreement was achieved between the local absorption profiles of Chapter 5 calculated using *Mathematica* and *RSoft DiffractMOD*. Finally, many of the results of Chapter 2 have been reproduced by Lumerical, which sells finite element solvers for optical calculations (see http://www.lumerical.com/fdtd_online_help/solar_organic.php for details).

## A.2 Electrical Modeling Program

All electrical simulations in Chapters 4 and 5 were conducted in *COMSOL Multiphysics*, a finite element solver. Figure A.2 shows agreement between *COMSOL Multiphysics* and the results from Koster et al. for the model system MDMO-PPV:PCBM with active layer thickness of 120 nm[65]. The J-V curves, concentration profiles of electrons and holes, and net generation rate of free carriers are reproduced using *COMSOL Multiphysics*. Excellent agreement is achieved, which demonstrates the accuracy of the simulation method.

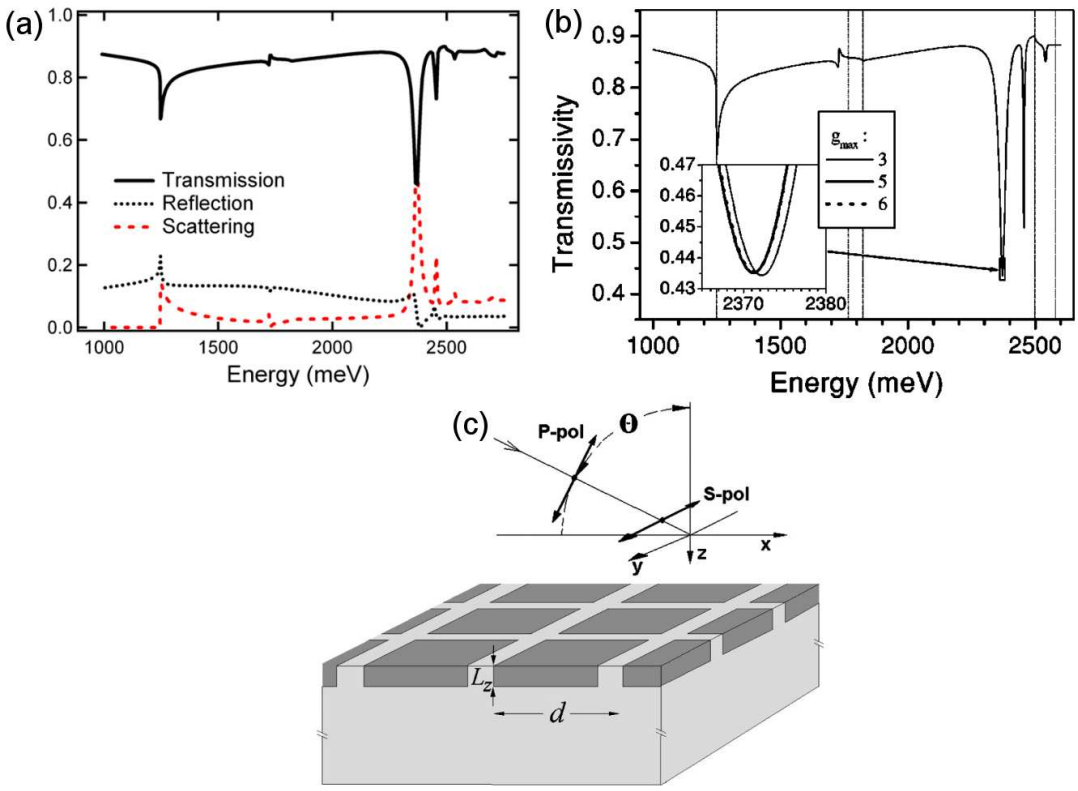


Figure A.1: Simulated optical properties for photonic crystal slab using scattering matrix method (a) developed for this thesis and (b) from Tikhodeev et al.[84]. (c) Schematic of the model structure with index of refraction of 1.44 (light grey) and 1.99 (dark grey)[84]. The periodicity, $d$, is 680 nm, while the post height, $L_z$, is 120 nm. Figures from Tikhodeev et al.: Copyright 2002 by The American Physical Society.

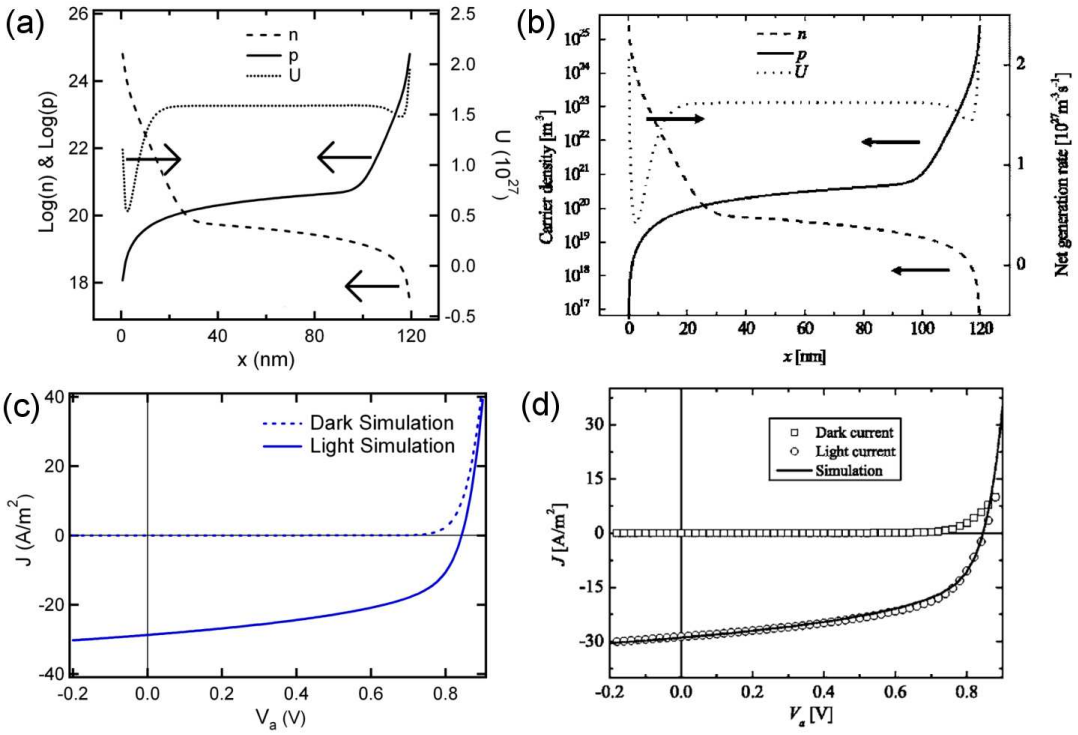


Figure A.2: (a,b) Concentration of electons, $n$, and holes, $p$, and net generation rate of free carriers, $U$, at short circuit using (a) *COMSOL Multiphysics* and (b) from Koster et al.[65]. (c,d) Simulated J-V curves using (c) *COMSOL Multiphysics* and (d) from Koster et al.[65]. The model system is MDMO-PPV:PCBM with 120 nm active layer thickness. Figures from Koster et al.: Copyright 2005 by The American Physical Society.

## A.3 Optical Measurement Set-up

The angular dependent IPCE and reflection measurements in Chapter 3 were conducted on a custom-built measurement set-up, which consists of LabView controlled stepper motors and data acquisition software integrated to a Woollam ellipsometry monochromater. The sample is a 675 nm thin film of PMMA on a silicon substrate. The optical properties and thickness of PMMA were determined using spectroscopic ellipsometry and then input into the scattering matrix optical model described above to generate the reflection data under various angles of incidence. Very good agreement is achieved between the simulations and measurements.

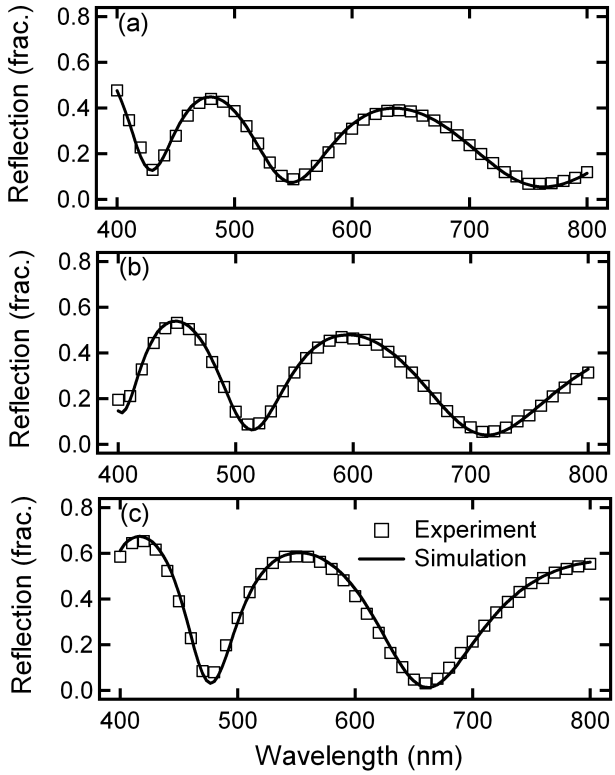


Figure A.3: Specular reflection of 675 nm PMMA film on silicon substrate at (a) 30°, (b) 45°, and (c) 60° incidence in s-polarization. The measurements are done using a custom-built angular reflection set-up, while the simulations are done using the scattering matrix method written in *Mathematica*.

# Bibliography


[1] A. Banerjee and V. M. Yakovenko. Universal patterns of inequality. *New J. Phys.*, 12:075032, 2010.

[2] M. A. Green, K. Emery, Y. Hishikawa, and W. Warta. Solar cell efficiency tables (version 36). *Prog. Photovoltaics Res. Appl.*, 18:346–352, 2010.

[3] A. J. Heeger. Nobel lecture in chemistry, 2000.

[4] C. W. Tang. Two-layer organic photovoltaic cell. *Appl. Phys. Lett.*, 48:183–185, 1986.

[5] J. J. M. Halls, C. A. Walsh, N. C. Greenham, E. A. Marseglia, R. H. Friend, S. C. Moratti, and A. B. Holmes. Efficient photodiodes from interpenetrating polymer networks. *Nature*, 376:498–500, 1995.

[6] G. Yu and A. J. Heeger. Charge separation and photovoltaic conversion in polymer composites with internal donor/acceptor heterojunctions. *J. Appl. Phys.*, 78:4510–4515, 1995.

[7] G. Li, V. Shrotriya, J. Huang, Y. Yao, T. Moriarty, K. Emery, and Y. Yang. High-efficiency solution processable self-organization of polymer blends. *Nat. Mater.*, 4:864–868, 2005.

[8] J. Peet, J. Y. Kim, N. E. Coates, W. L. Ma, D. Moses, A. J. Heeger, and G. C. Bazan. Efficiency enhancement in low-bandgap polymer solar cells by processing with alkane dithiols. *Nat. Mater.*, 6:497–500, 2007.

[9] S. H. Park, A. Roy, S. Beaupre, S. Cho, N. Coates, J. S. Moon, D. Moses, M. Leclerc, K. Lee, and A. J. Heeger. Bulk heterjunction solar cells with internal quantum efficiency approaching 100%. *Nat. Photonics*, 3:297–303, 2009.

[10] H.-Y. Chen, J. Hou, S. Zhang, Y. Liang, G. Yang, Y. Yang, L. Yu, Y. Wu, and G. Li. Polymer solar cells with enhanced open-circuit voltage and efficiency. *Nat. Photonics*, 3:649–653, 2009.

[11] Y. Liang, Z. Xu, J. Xia, S-T. Tsai, Y. Wu, G. Li, C. Ray, and L. Yu. For the Bright Future-Bulk Heterojunction Polymer Solar Cells with Power Conversion Efficiency of 7.4%. *Adv. Mater.*, 22:E135–E138, 2010.

[12] Solarmer Energy Inc. Press Release, .

[13] L. J. A. Koster, V. D. Mihailetchi, and P. W. M. Blom. Ultimate efficiency of polymer/fullerene bulk heterojunction solar cells. *Appl. Phys. Lett.*, 88:093511, 2006.

[14] J. D. Servaites, M. A. Ratner, and T. J. Marks. Practical efficiency limits in organic photovoltaic cells: Functional dependence of fill factor and external quantum efficiency. *Appl. Phys. Lett.*, 95:163302, 2009.

[15] M. C. Scharber, D. Mühlbacher, M. Koppe, P. Denk, C. Waldauf, A. J. Heeger, and C. J. Brabec. Design rules for donors in bulk-heterojunction solar cells towards 10% energy-conversion efficiency. *Adv. Mater.*, 18:789–794, 2006.

[16] K. M. Coakley and M. D. McGehee. Conjugated Polymer Photovoltaic Cells. *Chem. Mater.*, 16:4533–4542, 2004.

[17] H. Hoppe and N. S. Sariciftci. Organic solar cells: An overview. *J. Mater. Res.*, 19:1924–1945, 2004.

[18] S. Gunes, H. Neugebauer, and N. S. Sariciftci. Conjugated polymer-based organic solar cells. *Solar Cells*, 107:1324–1338, 2007.

[19] P. W. M. Blom, V. D. Mihailetchi, L. J. A. Koster, and D. E. Markov. Device Physics of Polymer:Fullerene Bulk Heterojunction Solar Cells. *Adv. Mater.*, 19:1551–1566, 2007.

[20] L.-M. Chen, Z. Hong, G. Li, and Y. Yang. Recent progress in polymer solar cells: Manipulation of polymer:fullerene morphology and the formation of efficient inverted polymer solar cells. *Adv. Mater.*, 21: 1434–1449, 2009.

[21] M. Niggemann, M. Riede, A. Gombert, and K. Leo. Light trapping in organic solar cells. *Phys. Stat. Sol. A*, 205:2862 – 2874, 2008.

[22] L. Escoubas, J.-J. Simon, P. Torchio, D. Duché, S. Vedraine, W. Vervisch, J. L. Rouzo, F. Flory, G. Rivière, G. Yeabiyo, and H. Derbal. Bringing some photonic structures for solar cells to the fore. *Appl. Optics*, 50: C329–C339, 2011.

[23] T. M. Clarke and J. R. Durrant. Charge photogeneration in organic solar cells. *Chem. Rev.*, 110:6736–6767, 2010.

[24] R. Steim, F. R. Kogler, and C. J. Brabec. Interface materials for organic solar cells. *J. Mater. Chem.*, 20: 2499–2512, 2010.

[25] L. A. A. Pettersson, L. S. Roman, and O. Inganas. Modeling photocurrent action spectra of photovoltaic devices based on organic thin films. *J. Appl. Phys.*, 86:487–496, 1999.

[26] N.-K. Persson, H. Arwin, and O. Inganas. Optical optimization of polyfluorene-fullerene blend photodiodes. *J. Appl. Phys.*, 97:034503, 2005.

[27] B. V. Andersson, D. M. Huang, A. J. Moulé, and O. Inganäs. An optical spacer is no panacea for light collection in organic solar cells. *Appl. Phys. Lett.*, 94:043302, 2009.

[28] T. Ameri, G. Dennler, C. Waldauf, P. Denk, K. Forberich, M. C. Scharber, C. J. Brabec, and K. Hingerl. Realization, characterization, and optical modeling of inverted bulk-heterojunction organic solar cells. *J. Appl. Phys.*, 103:084506, 2008.

[29] J. Y. Kim, S. H. Kim, H.-H. Lee, K. Lee, W. Ma, X. Gong, and A. J. Heeger. New architecture for high-efficiency polymer photovoltaic cells using solution-based titanium oxide as an optical spacer. *Adv. Mater.*, 18:572–576, 2006.

[30] A. J. Moulé and K. Meerholz. Minimizing optical losses in bulk heterojunction polymer solar cells. *Appl. Phys. B*, 86:721–727, 2007.

[31] J. D. Kotlarski, P. W. M. Blom, L. J. A. Koster, M. Lenes, and L. H. Slooff. Combined optical and electrical modeling of polymer:fullerene bulk heterojunction solar cells. *J. Appl. Phys.*, 103:084502, 2008.

[32] L. A. A. Pettersson, S. Ghosh, and O. Inganas. Optical anisotropy in thin films of poly(3,4-ethylenedioxythiophene)-poly(4-styrenesulfonate). *Org. Electron.*, 3:143–148, 2002.

[33] D.-H. Ko, J. R. Tumbleston, M.-R. Ok, H. Chun, R. Lopez, and E. Samulski. Suppression of bimolecular recombination by UV-sensitive electron transport layers in organic solar cells. *J. Appl. Phys.*, 108:083101, 2010.

[34] J. R. Tumbleston, D.-H. Ko, E. T. Samulski, and R. Lopez. Electrophotonic enhancement of bulk heterojunction organic solar cells through photonic crystal photoactive layer. *Appl. Phys. Lett.*, 94:043305, 2009.

[35] U. Zhokhavets, T. Erb, H. Hoppe, G. Gobsch, and N. S. Sariciftci. Effect of annealing of poly(3-hexylthiophene)/fullerene bulk heterojunction composites on structural and optical properties. *Thin Solid Films*, 496:679–682, 2006.

[36] D. E. Markov, C. Tanase, P. W. M. Blom, and J. Wildeman. Simultaneous enhancement of charge transport and exciton diffusion in poly(p-phenylene vinylene) derivatives. *Phys. Rev. B*, 72:045217, 2005.

[37] P. E. Shaw, A. Ruseckas, and I. D. W. Samuel. Exciton diffusion measurements in poly(3-hexylthiophene). *Adv. Mater.*, 20:3516–3520, 2008.

[38] J. J. M. Halls, K. Pichler, R. H. Friend, S. C. Moratti, and A. B. Holmes. Exciton diffusion and dissociation in a poly (p-phenylenevinylene)/C60 heterojunction photovoltaic cell. *Appl. Phys. Lett.*, 68:3120–3122, 1996.

[39] H. Hoppe, M. Niggemann, C. Winder, J. Kraut, R. Hiesgen, A. Hinsch, D. Meissner, and N. S. Sariciftci. Nanoscale morphology of conjugated polymer/fullerene-based bulk-heterojunction solar cells. *Adv. Funct. Mater*, 14:1005–1011, 2004.

[40] H. Hoppe and N. S. Sariciftci. Morphology of polymer/fullerene bulk heterojunction solar cells. *J. Mater. Chem.*, 16:45–61, 2006.

[41] L. S. C. Pingree, O. G. Reid, and D. S. Ginger. Imaging the evolution of nanoscale photocurrent collection and transport networks during annealing of polythiophene/fullerene solar cells. *Nano Lett.*, 9:2946–2952, 2009.

[42] C. Groves, O. G. Reid, and D. S. Ginger. Heterogeneity in polymer solar cells: local morphology and performance in organic photovoltaics studied with scanning probe microscopy. *Acc. Chem. Res.*, 43:612–620, 2010.

[43] J. S. Moon, J. K. Lee, S. Cho, J. Byun, and A. J. Heeger. Columnlike structure of the cross-sectional morphology of bulk heterojunction materials. *Nano Lett.*, 9:230–234, 2009.

[44] H. Ade and H. Stoll. Near-edge X-ray absorption fine-structure microscopy of organic and magnetic materials. *Nat. Mater.*, 8:281–290, 2009.

[45] C. J. Brabec, G. Zerza, G. Cerullo, S. de Silvestri, S. Luzzati, J. C. Hummelen, and S. Sariciftci. Tracing photoinduced electron transfer process in conjugated polymer/fullerene bulk heterojunctions in real time. *Chem. Phys. Lett.*, 340:232–236, 2001.

[46] C. L. Braun. Electric field assisted dissociation of charge transfer states as a mechanism of photocarrier production. *J. Chem. Phys.*, 80:4157–4161, 1984.

[47] V. D. Mihailetchi, L. J. A. Koster, J C. Hummelen, and P. W. M. Blom. Photocurrent Generation in Polymer-Fullerene Bulk Heterojunctions. *Phys. Rev. Lett.*, 93:216601, 2004.

[48] K. Vandewal, K. Tvingstedt, A. Gadisa, O. Inganäs, and J. V. Manca. On the origin of the open-circuit voltage of polymer-fullerene solar cells. *Nat. Mater.*, 8:904–909, 2009.

[49] K. Vandewal, K. Tvingstedt, A. Gadisa, O. Inganäs, and J. V. Manca. Relating the open-circuit voltage to interface molecular properties of donor:acceptor bulk heterojunction solar cells. *Phys. Rev. B*, 81:125204, 2010.

[50] X. He, F. Gao, G. Tu, D. Hasko, S. Hüttner, U. Steiner, N. C. Greenham, R. H. Friend, and W. T. S. Huck. Formation of nanopatterned polymer blends in photovoltaic devices. *Nano Lett.*, 10:1302–1307, 2010.

[51] V. D. Mihailetchi, J. Wildeman, and P. W. M. Blom. Space-charge limited photocurrent. *Phys. Rev. Lett.*, 94:126602, 2005.

[52] V. Mihailetchi, L. J. A. Koster, and P. W. M. Blom. Effect of metal electrodes on the performance of polymer:fullerene bulk heterojunction solar cells. *Appl. Phys. Lett.*, 85:970–972, 2004.

[53] J. D. Servaites, S. Yeganeh, T. J. Marks, and M. A. Ratner. Efficiency Enhancement in Organic Photovoltaic Cells: Consequences of Optimizing Series Resistance. *Adv. Funct. Mater.*, 20:97–104, 2010.

[54] A. Wagenpfahl, D. Rauh, M. Binder, C. Deibel, and V. Dyakonov. S-shaped current-voltage characteristics of organic solar devices. *Phys. Rev. B*, 82:115306, 2010.

[55] D. W. Sievers, V. Shrotriya, and Y. Yang. Modeling optical effects and thickness dependent current in polymer bulk-heterojunction solar cells. *J. Appl. Phys.*, 100:114509, 2006.

[56] A.J. Moule and K. Meerholz. Intensity-dependent photocurrent generation at the anode in bulk-heterojunction solar cells. *Appl. Phys. B*, 92:209–218, 2008.

[57] G. Li, V. Shrotriya, Y. Yao, and Y. Yang. Investigation of annealing effects and film thickness dependence of polymer solar cells based on poly(3-hexylthiophene). *J. Appl. Phys.*, 98:043704, 2005.

[58] J. Gilot, I. Barbu, M. M. Wienk, and R. A. J. Janssen. The use of ZnO as optical spacer in polymer solar cells: Theoretical and experimental study. *Appl. Phys. Lett.*, 91:113520, 2007.

[59] R. Häusermann, E. Knapp, M. Moos, N. A. Reinke, T. Flatz, and B. Ruhstaller. Coupled optoelectronic simulation of organic bulk-heterojunction solar cells: Parameter extraction and sensitivity analysis. *J. Appl. Phys.*, 106:104507, 2009.

[60] J. D. Joannopoulos, R. D. Meade, and J. N. Winn. *Photonic Crystals: Molding the Flow of Light*. Princeton University Press, New Jersey, 1995.

[61] M. Niggemann, M. Glatthaar, A. Gombert, A. Hinsch, and V. Wittwer. Diffraction gratings and buried nano-electrodes architectures for organic solar cells. *Thin Solid Films*, 451-452:619–623, 2004.

[62] A. Abass, H. Shen, P. Bienstman, and B. Maes. Angle insensitive enhancement of organic solar cells using metallic gratings. *J. Appl. Phys.*, 109:023111, 2011.

[63] M.-S. Kim, J.-S. Kim, J. C. Cho, M. Shtein, L. J. Guo, and J. Kim. Flexible conjugated polymer photovoltaic cells with controlled heterojunctions fabricated using nanoimprint lithography. *Appl. Phys. Lett.*, 90:123113, 2007.

[64] M. Aryal, K. Trivedi, and W. Hu. Nano-confinement induced chain alignment in ordered P3HT nanostructures defined by nanoimprint lithography. *ACS Nano*, 3:3085–3090, 2009.

[65] L. J. A. Koster, E. C. P. Smits, V. D. Mihailetchi, and P. W. M. Blom. Device model for the operation of polymer/fullerene bulk heterojunction solar cells. *Phys. Rev. B*, 72:085205, 2005.

[66] A. J. Moulé, J. B. Bonekamp, and K. Meerholz. The effect of active layer thickness and composition on the performance of bulk-heterojunction solar cells. *J. Appl. Phys.*, 100:094503, 2006.

[67] W. Ma, C. Yang, X. Gong, K. Lee, and A. J. Heeger. Thermally stable, efficient polymer solar cells with nanoscale control of the interpenetrating network morphology. *Adv. Funct. Mater.*, 15:1617–1622, 2005.

[68] V. D. Mihailetchi, H. Xie, B. de Boer, L. J. A. Koster, and P. W. M. Blom. Charge transport and photocurrent generation in poly(3-hexylthiophene):methanofullerene bulk-heterojunction solar cells. *Adv. Funct. Mater.*, 16:699–708, 2006.

[69] R. Street, Sarah Cowan, and A. Heeger. Experimental test for geminate recombination applied to organic solar cells. *Phys. Rev. B*, 82:121301, 2010.

[70] C. R. Newman, C. D. Frisbie, D. A. da Silva Filho, J.-L. Bredas, P. C. Ewbank, and K. R. Mann. Introduction to organic thin film transistors and design of n-channel organic semiconductors. *Chem. Mater.*, 16: 4436–4451, 2004.

[71] V. D. Mihailetchi, L. J. A. Koster, P. W. M. Blom, C. Melzer, B. de Boer, J. K. J. van Duren, and R. A. J. Janssen. Compositional dependence of the performance of poly(p-phenylene vinylene):methanofullerene bulk-heterojunction solar cells. *Adv. Funct. Mater.*, 15:795–801, 2005.

[72] E. Yablonovitch and G. D. Cody. Intensity enhancement in textured optical sheets for solar cells. *IEEE Trans. Electron Devices*, 29:300–305, 1982.

[73] V. Andersson, K. Tvingstedt, and O. Inganäs. Optical modeling of a folded organic solar cell. *J. Appl. Phys.*, 103:094520, 2008.

[74] M. Agrawal and P. Peumans. Broadband optical absorption enhancement through coherent light trapping in thin-film photovoltaic cells. *Opt. Express*, 16:5385–5396, 2008.

[75] Z. Yu, A. Raman, and S. Fan. Fundamental limit of nanophotonic light trapping in solar cells. *Proc. Natl. Acad. Sci.*, 2010:1–6, 2010.

[76] D. W. Zhao, S. T. Tan, L. Ke, P. Liu, A. K. K. Kyaw, X. W. Sun, G. Q. Lo, and D. L. Kwong. Optimization of an inverted organic solar cell. *Sol. Energ. Mat. Sol. Cells*, 94:985–991, 2010.

[77] P. Bermel, C. Luo, L. Zeng, L. C. Kimerling, and J. D. Joannopoulos. Improving thin-film crystalline silicon solar cell efficiencies with photonic crystals. *Opt. Express*, 15:16986–17000, 2007.

[78] D. Zhou and R. Biswas. Photonic crystal enhanced light-trapping in thin film solar cells. *J. Appl. Phys.*, 103:093102, 2008.

[79] L. Zeng, Y. Yi, C. Hong, J. Liu, N. Feng, X. Duan, L. C. Kimerling, and B. A. Alamariu. Efficiency enhancement in Si solar cells by textured photonic crystal back reflector. *Appl. Phys. Lett.*, 89:111111, 2006.

[80] L. Zeng, P. Bermel, Y. Yi, B. A. Alamariu, K. A. Broderick, J. Liu, C. Hong, X. Duan, J. Joannopoulos, and L. C. Kimerling. Demonstration of enhanced absorption in thin film Si solar cells with textured photonic crystal back reflector. *Appl. Phys. Lett.*, 93:221105, 2008.

[81] D. Duché, L. Escoubas, J.-J. Simon, P. Torchio, W. Vervisch, and F. Flory. Slow Bloch modes for enhancing the absorption of light in thin films for photovoltaic cells. *Appl. Phys. Lett.*, 92:193310, 2008.

[82] T. Fujita, Y. Sato, T. Kuitani, and T. Ishihara. Tunable polariton absorption of distributed feedback microcavities at room temperature. *Phys. Rev. B*, 57:428–434, 1998.

[83] R. Shimada, A. L. Yablonskii, S. G. Tikhodeev, and T. Ishihara. Transmission properties of a two-dimensional photonic crystal slab with an excitonic resonance. *IEEE J. Quantum Electron.*, 38:872–879, 2002.

[84] S. G. Tikhodeev, A. L. Yablonskii, E. A. Muljarov, N. A. Gippius, and T. Ishihara. Quasiguided modes and optical properties of photonic crystal slabs. *Phys. Rev. B*, 66:045102, 2002.

[85] J. R. Tumbleston, D.-H. Ko, E. T. Samulski, and R. Lopez. Absorption and quasiguided mode analysis of organic solar cells with photonic crystal photoactive layers. *Opt. Express*, 17:7670–7681, 2009.

[86] W. J. E. Beek, M. M. Wienk, M. Kemerink, X. Yang, and R. A. J. Janssen. Hybrid zinc oxide conjugated polymer bulk heterojunction solar cells. *J. Phys. Chem. B*, 109:9505–9516, 2005.

[87] D. M. Whittaker and I. S. Culshaw. Scattering-matrix treatment of patterned multilayer photonic structures. *Phys. Rev. B*, 60:2610–2618, 1999.

[88] Reference Solar Spectral Irradiance, Air Mass 1.5, . URL `http://rredc.nrel.gov/solar/spectra/am1.5/`.

[89] Jan Gilot, Martijn M Wienk, and René A J Janssen. Double and triple junction polymer solar cells processed from solution. *Appl. Phys. Lett.*, 90:143512, 2007.

[90] A. L. Roest, J. J. Kelly, D. Vanmaekelbergh, and E. A. Meulenkamp. Staircase in the electron mobility of a ZnO quantum dot assembly due to shell filling. *Phys. Rev. Lett.*, 89:036801, 2002.

[91] H.-L. Yip, S. K. Hau, N. S. Baek, H. Ma, and A. K.-Y. Jen. Polymer solar cells that use self-assembled-monolayer-modified ZnO/metals as cathodes. *Adv. Mater.*, 20:2376–2382, 2008.

[92] P. Peumans, V. Bulovic, and S. R. Forrest. Efficient photon harvesting at high optical intensities in ultrathin organic double-heterostructure photovoltaic diodes. *Appl. Phys. Lett.*, 76:2650–2652, 2000.

[93] M. Niggemann, M. Glatthaar, P. Lewer, C. Muller, J. Wagner, and A. Gombert. Functional microprism substrate for organic solar cells. *Thin Solid Films*, 511-512:628–633, 2006.

[94] S.-B. Rim, S. Zhao, S. R. Scully, M. D. McGehee, and P. Peumans. An effective light trapping configuration for thin-film solar cells. *Appl. Phys. Lett.*, 91:243501, 2007.

[95] Y. Zhou, F. Zhang, K. Tvingstedt, W. Tian, and O. Inganäs. Multifolded polymer solar cells on flexible substrates. *Appl. Phys. Lett.*, 93:033302, 2008.

[96] K. Tvingstedt, V. Andersson, F. Zhang, and O. Inganäs. Folded reflective tandem polymer solar cell doubles efficiency. *Appl. Phys. Lett.*, 91:123514, 2007.

[97] S.-I. Na, S.-S. Kim, J. Jo, S.-H. Oh, J. Kim, and D.-Y. Kim. Efficient polymer solar cells with surface felief gratings fabricated by simple soft lithography. *Adv. Funct. Mater.*, 18:3956–3963, 2008.

[98] L. S. Roman, O. Inganäs, T. Granlund, T. Nyberg, M. Svensson, M. R. Andersson, and J. C. Hummelen. Trapping light in polymer photodiodes with soft embossed gratings. *Adv. Mater.*, 12:189–195, 2000.

[99] K. Tvingstedt, N.-K. Persson, O. Inganäs, A. Rahachou, and I. V. Zozoulenko. Surface plasmon increase absorption in polymer photovoltaic cells. *Appl. Phys. Lett.*, 91:113514, 2007.

[100] C. Cocoyer, L. Rocha, L. Sicot, B. Geffroy, R. de Bettignies, C. Sentein, C. Fiorini-Debuisschert, and P. Raimond. Implementation of submicrometric periodic surface structures toward improvement of organic-solar-cell performances. *Appl. Phys. Lett.*, 88:133108, 2006.

[101] J. P. Rolland, B. W. Maynor, L. E. Euliss, A. E. Exner, G. M. Denison, J. M. DeSimone, Chapel Hill, North Carolina, and Chemical Engineering. Direct fabrication and harvesting of monodisperse, shape-specific nanobiomaterials. *J. Am. Chem. Soc.*, 127:10096–10100, 2005.

[102] J. R. Tumbleston, D.-H. Ko, R. Lopez, and E. T. Samulski. Characterizing enhanced performance of nanopatterned bulk heterojunction organic photovoltaics. *Proc. SPIE*, 7047:70470S, 2008.

[103] D.-H. Ko, J. R. Tumbleston, L. Zhang, S. Williams, J. M. DeSimone, R. Lopez, and E. T. Samulski. Photonic crystal geometry for organic solar cells. *Nano Lett.*, 9:2742–2746, 2009.

[104] D.-H. Ko, J. R. Tumbleston, R. Lopez, and E. T. Samulski. Photonic crystal geometry for organic polymer:fullerene standard and inverted solar cells. *J. Phys. Chem. C*, 115:4247–4245, 2011.

[105] K. D. Alexander, M. J. Hampton, S. Zhang, A. Dhawan, H. Xu, and R. Lopez. A high-throughput method for controlled hot-spot fabrication in SERS-active gold nanoparticle dimer arrays. *J. Raman Spectrosc.*, 40: 2171–2175, 2009.

[106] T. J. Merkel, S. W. Jones, K. P. Herlihy, F. R. Kersey, A. R. Shields, M. Napier, J. C. Luft, H. Wu, W. C. Zamboni, A. Z. Wang, J. E. Bear, and J. M. DeSimone. Using mechanobiological mimicry of red blood cells to extend circulation times of hydrogel microparticles. *Proc. Natl. Acad. Sci.*, 108:586–591, 2011.

[107] M. J. Hampton, S. S. Williams, Z. Zhou, J. Nunes, D.-H. Ko, J. L. Templeton, E. T. Samulski, and J. M. Desimone. The patterning of sub-500 nm inorganic oxide structures. *Adv. Mater.*, 20:2667–2673, 2008.

[108] Jennifer Y Kelly and Joseph M DeSimone. Shape-specific, monodisperse nano-molding of protein particles. *J. Am. Chem. Soc.*, 130:5438–5439, 2008.

[109] S. S. Williams, S. Retterer, R. Lopez, R. Ruiz, E. T. Samulski, and J. M. DeSimone. High-resolution PFPE-based molding techniques for nanofabrication of high-pattern density, sub-20 nm features: A fundamental materials approach. *Nano Lett.*, 10:1421–1428, 2010.

[110] S.-Y. Chuang, H.-L. Chen, W.-H. Lee, Y.-C. Huang, W.-F. Su, W.-M. Jen, and C.-W. Chen. Regioregularity effects in the chain orientation and optical anisotropy of composite polymer/fullerene films for high-efficiency, large-area organic solar cells. *J. Mater. Chem.*, 19:5554–5560, 2009.

[111] G. Dennler, K. Forberich, M. C. Scharber, C. J. Brabec, I. Tomiš, K. Hingerl, and T. Fromherz. Angle dependence of external and internal quantum efficiencies in bulk-heterojunction organic solar cells. *J. Appl. Phys.*, 102:054516, 2007.

[112] C. Zhang, S. W. Tong, C. Jiang, E. T. Kang, D. S. H. Chan, and C. Zhu. Efficient multilayer organic solar cells using the optical interference peak. *Appl. Phys. Lett.*, 93:043307, 2008.

[113] S. E. Shaheen, C. J. Brabec, N. S. Sariciftci, F. Padinger, J. C. Hummelen, and T. Fromherz. 2.5% efficient organic plastic solar cells. *Appl. Phys. Lett.*, 78:841–843, 2001.

[114] C. Tao, S. Ruan, G. Xie, X. Kong, L. Shen, F. Meng, C. Liu, X. Zhang, W. Dong, and W. Chen. Role of tungsten oxide in inverted polymer solar cells. *Appl. Phys. Lett.*, 94:043311, 2009.

[115] K. S. Nalwa, J.-M. Park, K.-M. Ho, and S. Chaudhary. On realizing higher efficiency polymer solar cells using a textured substrate platform. *Adv. Mater.*, 23:112–116, 2011.

[116] J. Nelson. *The Physics of Solar Cells*. Imperial College Press, London, 2003.

[117] T. Aernouts, W. Geens, J. Poortmans, P. Heremans, S. Borghs, and R. Mertens. Extraction of bulk and contact components of the series resistance in organic bulk donor-acceptor-heterojunctions. *Thin Solid Films*, 404:297–301, 2002.

[118] J. R. Tumbleston, D.-H. Ko, E. T. Samulski, and R. Lopez. Nonideal parasitic resistance effects in bulk heterojunction organic solar cells. *J. Appl. Phys.*, 108:084514, 2010.

[119] J. R. Tumbleston, D.-H. Ko, E. T. Samulski, and R. Lopez. Electro-optical model of photonic crystal bulk heterojunction organic solar cells. *AIP Conf. Proc.*, 1280:121–129, 2010.

[120] L. J. A. Koster, V. D. Mihailetchi, and P. W. M. Blom. Bimolecular recombination in polymer/fullerene bulk heterojunction solar cells. *Appl. Phys. Lett.*, 88:052104, 2006.

[121] L. J. A. Koster, V. D. Mihailetchi, H. Xie, and P. W. M. Blom. Origin of the light intensity dependence of the short-circuit current of polymer/fullerene solar cells. *Appl. Phys. Lett.*, 87:203502, 2005.

[122] L. J. A. Koster, V. D. Mihailetchi, R. Ramaker, and P. W. M. Blom. Light intensity dependence of open-circuit voltage of polymer:fullerene solar cells. *Appl. Phys. Lett.*, 86:123509, 2005.

[123] M. M. Mandoc, W. Veurman, L. J. A. Koster, B. de Boer, and P. W. M. Blom. Origin of the reduced fill factor and photocurrent in MDMO-PPV:PCNEPV all-polymer solar cells. *Adv. Funct. Mater.*, 17: 2167–2173, 2007.

[124] L. J. A. Koster, W. J. van Strien, W. J. E. Beek, and P. W. M. Blom. Device operation of conjugated polymer/zinc oxide bulk heterojunction solar cells. *Adv. Funct. Mater.*, 17:1297–1302, 2007.

[125] D. Veldman, O. Ipek, S. C. J. Meskers, J. Sweelssen, M. M. Koetse, S. C. Veenstra, J. M. Kroon, S. S. van Bavel, J. Loos, and R. A. J. Janssen. Compositional and electric field dependence of the dissociation of charge transfer excitons in alternating polyfluorene copolymer/fullerene blends. *J. Am. Chem. Soc.*, 130: 7721–7735, 2008.

[126] C. Deibel, T. Strobel, and V. Dyakonov. Origin of the efficient polaron-pair dissociation in polymer-fullerene blends. *Phys. Rev. Lett.*, 103:036402, 2009.

[127] C. Groves and N. C. Greenham. Bimolecular recombination in polymer electronic devices. *Phys. Rev. B*, 78:155205, 2008.

[128] A. Pivrikas, G. Juska, A. J. Mozer, M. Scharber, K. Arlauskas, N. S. Sariciftci, H. Stubb, and R. Osterbacka. Bimolecular recombination coefficient as a sensitive testing parameter for low-mobility solar-cell materials. *Phys. Rev. Lett.*, 94:176806, 2005.

[129] T. Kirchartz, B. E. Pieters, K. Taretto, and U. Rau. Mobility dependent efficiencies of organic bulk heterojunction solar cells: Surface recombination and charge transfer state distribution. *Phys. Rev. B*, 80: 035334, 2009.

[130] M. Niggemann, W. Graf, and A. Gombert. Realization of ultrahigh photovoltages with organic photovoltaic nanomodules. *Adv. Mater.*, 20:4055–4060, 2008.

[131] R. A. Marsh, C. R. McNeill, A. Abrusci, A. R. Campbell, and R. H. Friend. A unified description of current voltage characteristics in organic and hybrid photovoltaics under low light intensity 2008. *Nano Lett.*, 8: 1393–1398, 2008.

[132] C. Waldauf, M. C. Scharber, P. Schilinsky, J. A. Hauch, and C. J. Brabec. Physics of organic bulk heterojunction devices for photovoltaic applications. *J. Appl. Phys.*, 99:104503, 2006.

[133] S. Chaudhary, H. Lu, A. M. Muller, C. J. Bardeen, and M. Ozkan. Hierarchical placement and associated optoelectronic impact of carbon nanotubes in polymer-fullerene solar cells. *Nano Lett.*, 7:1973–1979, 2007.

[134] M. D. Irwin, D. B. Buchholz, A. W. Hains, R. P. H. Chang, and T. J. Marks. P-type semiconducting nickel oxide as an efficiency-enhancing anode interfacial layer in polymer bulk-heterojunction solar cells. *Proc. Natl. Acad. Sci.*, 105:2783–2787, 2008.

[135] S. Yoo, B. Domercq, and B. Kippelen. Intensity-dependent equivalent circuit parameters of organic solar cells based on pentacene and C60. *J. Appl. Phys.*, 97:103706, 2005.

[136] P. Schilinsky, C. Waldauf, J. Hauch, and C. J. Brabec. Simulation of light intensity dependent current characteristics of polymer solar cells. *J. Appl. Phys.*, 95:2816–2819, 2004.

[137] C. G. Shuttle, A. Maurano, R. Hamilton, B. O'Regan, J. C. de Mello, and J. R. Durrant. Charge extraction analysis of charge carrier densities in a polythiophene/fullerene solar cell: Analysis of the origin of the device dark current. *Appl. Phys. Lett.*, 93:183501, 2008.

[138] C. R. McNeill, J. J. M. Halls, R. Wilson, G. L. Whiting, S. Berkebile, M. G. Ramsey, R. H. Friend, and N. C. Greenham. Efficient polythiophene/polyfluorene copolymer bulk heterojunction photovoltaic devices: Device physics and annealing effects. *Adv. Funct. Mater.*, 18:2309–2321, 2008.

[139] C. G. Shuttle, B. O'Regan, A. M. Ballantyne, J. Nelson, D. D. C. Bradley, and J. R. Durrant. Bimolecular recombination losses in polythiophene: Fullerene solar cells. *Phys. Rev. B*, 78:113201, 2008.

[140] C. Waldauf, M. Morana, P. Denk, P. Schilinsky, K. Coakley, S. A. Choulis, and C. J. Brabec. Highly efficient inverted organic photovoltaics using solution based. *Appl. Phys. Lett.*, 89:233517, 2006.

[141] R. Steim, S. A. Choulis, P. Schilinsky, and C. J. Brabec. Interface modification for highly efficient organic photovoltaics. *Appl. Phys. Lett.*, 92:093303, 2008.

[142] S. K. Hau, H.-L. Yip, O. Acton, N. S. Baek, H. Ma, and A. K.-Y. Jen. Interfacial modification to improve inverted polymer solar cells. *J. Mater. Chem.*, 18:5113–5119, 2008.

[143] A. K. K. Kyaw, X. W. Sun, C. Y. Jiang, G. Q. Lo, D. W. Zhao, and D. L. Kwong. An inverted organic solar cell employing a sol-gel derived ZnO electron selective layer and thermal evaporated MoO 3 hole selective layer. *Appl. Phys. Lett.*, 93:221107, 2008.

[144] G. Li, C.-W. Chu, V. Shrotriya, J. Huang, and Y. Yang. Efficient inverted polymer solar cells. *Appl. Phys. Lett.*, 88:253503, 2006.

[145] F. Verbakel, S. C. J. Meskers, and R. A. J. Janssen. Electronic memory effects in diodes of zinc oxide nanoparticles in a matrix of polystyrene or poly(3-hexylthiophene). *J. Appl. Phys.*, 102:083701, 2007.

[146] C. Uhrich, D. Wynands, S. Olthof, M. K. Riede, K. Leo, S. Sonntag, B. Maennig, and M. Pfeiffer. Origin of open circuit voltage in planar and bulk heterojunction organic thin-film photovoltaics depending on doped transport layers. *J. Appl. Phys.*, 104:043107, 2008.

[147] M. Caironi, T. Agostinelli, D. Natali, M. Sampietro, R. Cugola, M. Catellani, and S. Luzzati. External quantum efficiency versus charge carriers mobility in polythiophene/methanofullerene based planar photodetectors. *J. Appl. Phys.*, 102:024503, 2007.

[148] C. Tanase, E. J. Meijer, P. W. M. Blom, and D. M. de Leeuw. Unification of the hole transport in polymeric field-effect transistors and light-emitting diodes. *Phys. Rev. Lett.*, 91:216601, 2003.

[149] L. H. Jimison, M. F. Toney, I. McCulloch, M. Heeney, and A. Salleo. Charge-transport anisotropy due to grain boundaries in directionally crystallized thin films of regioregular poly(3-hexylthiophene). *Adv. Mater.*, 21:1568–1572, 2009.

[150] R. W. I. de Boer, M. Jochemsen, T. M. Klapwijk, A. F. Morpurgo, J. Niemax, A. K. Tripathi, and J. Pflaum. Space charge limited transport and time of flight measurements in tetracene single crystals: A comparative study. *J. Appl. Phys.*, 95:1196–1202, 2004.

[151] S. Tiwari and N. C. Greenham. Charge mobility measurement techniques in organic semiconductors. *Opt. Quant. Electron.*, 41:69–89, 2009.

[152] J. R. Tumbleston, D.-H. Ko, E. T. Samulski, and R. Lopez. Analyzing local exciton generation profiles as a means to extract transport lengths in organic solar cells. *Phys. Rev. B*, 82:205325, 2010.

[153] F.-C. Chen, J.-L. Wu, and Y. Hung. Spatial redistribution of the optical field intensity in inverted polymer solar cells. *Appl. Phys. Lett.*, 96:193304, 2010.

[154] J.-T. Shieh, C.-H. Liu, H.-F. Meng, S.-R. Tseng, Y.-C. Chao, and S.-F. Horng. The effect of carrier mobility in organic solar cells. *J. Appl. Phys.*, 107:084503, 2010.

[155] A. Huijser, T. J. Savenije, A. Shalav, and L. D. A. Siebbeles. An experimental study on the molecular organization and exciton diffusion in a bilayer of a porphyrin and poly(3-hexylthiophene). *J. Appl. Phys.*, 104:034505, 2008.

[156] G. Juska, K. Genevicius, N. Nekrasas, G. Sliauzys, and G. Dennler. Trimolecular recombination in polythiophene: fullerene bulk heterojunction solar cells. *Appl. Phys. Lett.*, 93:143303, 2008.

[157] M. Limpinsel, A. Wagenpfahl, M. Mingebach, C. Deibel, and V. Dyakonov. Photocurrent in bulk heterojunction solar cells. *Phys. Rev. B*, 81:085203, 2010.

[158] L. Zeng, C. W. Tang, and S. H. Chen. Effects of active layer thickness and thermal annealing on polythiophene: Fullerene bulk heterojunction photovoltaic devices. *Appl. Phys. Lett.*, 97:053305, 2010.

[159] S. Cowan, A. Roy, and A. J. Heeger. Recombination in polymer-fullerene bulk heterojunction solar cells. *Phys. Rev. B*, 82:245207, 2010.

[160] R. A. Street, M. Schoendorf, A. Roy, and J. H. Lee. Interface state recombination in organic solar cells. *Phys. Rev. B*, 81:205307, 2010.

[161] Carsten Deibel. Charge carrier dissociation and recombination in polymer solar cells. *Phys. Status Solidi A*, 2736:2731–2736, 2009.

[162] L. J. A. Koster, M. M. Wienk, K. Maturová, and R. A. J. Janssen. Quantifying bimolecular recombination losses in organic bulk heterojunction solar cells. *Adv. Mater.*, page ASAP, 2011.

[163] Z. E. Ooi, R. Jin, J. Huang, Y. F. Loo, A. Sellinger, and J. C. de Mello. On the pseudo-symmetric current voltage response of bulk heterojunction solar cells. *J. Mater. Chem.*, 18:1644–1651, 2008.

[164] M. Lenes, F. B. Kooistra, J. C. Hummelen, I. van Severen, L. Lutsen, D. Vanderzande, T. J. Cleij, and P. W. M. Blom. Charge dissociation in polymer:fullerene bulk heterojunction solar cells with enhanced permittivity. *J. Appl. Phys.*, 104:114517, 2008.

[165] Y. Yuan, T. J. Reece, P. Sharma, S. Poddar, S. Ducharme, A. Gruverman, Y. Yang, and J. Huang. Efficiency enhancement in organic solar cells with ferroelectric polymers. *Nat. Mater.*, 2011:1–7, 2011.

[166] C. Groves, L. J. A. Koster, and N. C. Greenham. The effect of morphology upon mobility: Implications for bulk heterojunction solar cells with nonuniform blend morphology. *J. Appl. Phys.*, 105:094510, 2009.

[167] L. Meng, Y. Shang, Q. Li, Y. Li, X. Zhan, Z. Shuai, R. G. E. Kimber, and A. B. Walker. Dynamic Monte Carlo simulation for highly efficient polymer blend photovoltaics. *J. Phys. Chem. B*, 114:36–41, 2010.

[168] Jdrzej Szmytkowski. Modeling the electrical characteristics of P3HT:PCBM bulk heterojunction solar cells: Implementing the interface recombination. *Semicond. Sci. Technol.*, 25:015009, 2010.

[169] W. Shockley and H. J. Queisser. Detailed balance limit of efficiency of p-n junction solar cells. *J. Appl. Phys.*, 32:510–519, 1961.